FOSSIL ENERGY

DOE/BC/14851-2
(OSTI ID: 6970)

PREDICTION OF GAS INJECTION PERFORMANCE FOR HETEROGENEOUS RESERVOIRS

Annual Report
September 1996 – September 1997

By
Martin J. Blunt
Franklin M. Orr, Jr.

Date Published: May 1999

Work Performed Under Contract No. DE-FG22-96BC14851

Stanford University
Stanford, California

National Petroleum Technology Office
U. S. DEPARTMENT OF ENERGY
Tulsa, Oklahoma

DISCLAIMER

This report was prepared as an account of work sponsored by an agency of the United States Government. Neither the United States Government nor any agency thereof, nor any of their employees, makes any warranty, expressed or implied, or assumes any legal liability or responsibility for the accuracy, completeness, or usefulness of any information, apparatus, product, or process disclosed, or represents that its use would not infringe privately owned rights. Reference herein to any specific commercial product, process, or service by trade name, trademark, manufacturer, or otherwise does not necessarily constitute or imply its endorsement, recommendation, or favoring by the United States Government or any agency thereof. The views and opinions of authors expressed herein do not necessarily state or reflect those of the United States Government.

This report has been reproduced directly from the best available copy.

Available to DOE and DOE contractors from the Office of Scientific and Technical Information, P.O. Box 62, Oak Ridge, TN 37831; prices available from (423) 576-8401.

Available to the public from the National Technical Information Service, U.S. Department of Commerce, 5285 Port Royal Rd., Springfield, VA 22161

DOE/BC/14851-2
Distribution Category UC-122

Prediction of Gas Injection Performance for Heterogeneous Reservoirs

By
Martin J. Blunt
Franklin M. Orr, Jr.

May 1999

Work Performed Under Contract DE-FG22-96BC14851

Prepared for
U.S. Department of Energy
Assistant Secretary for Fossil Energy

Jerry F. Casteel, Technology Manager
National Petroleum Technology Office
P.O. Box 3628
Tulsa, OK 74101

Prepared by
Stanford University
Petroleum Engineering Department
651 Serra Street, Room 260
Stanford, CA 94305-2220

Contents

List of Tables

List of Figures

Acknowledgements

We would also like to take the opportunity to thank the many students, post-docs and research associates who contributed to this work. David DiCarlo is the research associate in charge of our experimental program. He joined us in August this year and already has had the unenviable task of preparing this report. Our previous research associate, Dengen Zhou, contributed much to Chapters 2 and 3 of this report. We wish him well in his new position at Chevron Research. Jon Burger, a research associate, now with PTS laboratories, did much to set up the CT scanner to measure three phase relative peremabilities, as described in Chapter 3. Rod Batycky, who received his Ph.D. in February and Acting Assistant Professor Marco Thiele, both of whom are now with StreamSim Technologies performed the streamline work described in Chapter 5. Darryl Fenwick, who received his Ph.D. in February and is now with the Institut Francais Du Petrole in Paris, developed the network model described in Chapter 2. Of our present students, Ph.D. candidate Akshay Sahni did the work in Chapter 3, while Ph.D. student Yun Wang did the work in Chapter 4. Our present group also includes post-docs Charles Schaefer and Yann Gautier, Ph.D. students Richard Hughes and Jichun Zhu, and MS students Tuba Firincioglu, Martha Crane, Rajiv Lulla, Mun Hong Hui and Stephanie Bertels. We look forward to describing their research in later reports.

We gratefully acknowledge the support of the Department of Energy under Grant No. DE-FG22-96BC14851. We thank Jerry Casteel and his colleagues for their continued interest and encouragement. We also are grateful for funding from the nine members of the SUPRI-C Gas Injection Affiliates Group: Arco, British Petroleum Exploration, Chevron, Exxon, Japan National Oil Corporation, Mobil, Norsk Hydro, Saga Petroleum, and Statoil. Without this generous support this work would not have been possible.

Martin Blunt
Lynn Orr
Stanford
December 1997

1. Introduction

This report describes research carried out in the Department of Petroleum Engineering at Stanford University from September 1996 - September 1997 under the first year of a three-year Department of Energy grant on the Prediction of Gas Injection Performance for Heterogeneous Reservoirs. The research effort is an integrated study of the factors affecting gas injection, from the pore scale to the field scale, and involves theoretical analysis, laboratory experiments and numerical simulation. The original proposal described research in four main areas: (1) Pore scale modeling of three phase flow in porous media; (2) Laboratory experiments and analysis of factors influencing gas injection performance at the core scale with an emphasis on the fundamentals of three phase flow; (3) Benchmark simulations of gas injection at the field scale; (4) Development of streamline-based reservoir simulator. Each stage of the research is planned to provide input and insight into the next stage, such that at the end we should have an integrated understanding of the key factors affecting field scale displacements. The chapters that follow give a detailed account of our progress in these areas.

In chapter 2, we provide a description of the results from a pore scale model of three phase flow in porous media. By coding pore scale displacement processes observed in micromodels and predicted from theoretical considerations, a numerical model may be developed that can compute macroscopic parameters, such as local oil recovery, relative permeability and capillary pressure from an understanding of the basic physics at the pore scale. We show that the three phase relative permeabilities depend on fluid properties, particularly spreading coefficient, and are extremely sensitive to the saturation path taken during the experiment. However, one simple idea emerges: for gas injection when the oil and water saturations are both low, the oil relative permeability, $k_{ro} \sim S_o^2$.

Chapter 3 details our experimental work using CT scanning to make in situ measurements of three phase saturations along a core during a displacement experiment. We provide an analysis that shows that from this and a knowledge of the capillary pressures, three phase relative permeabilities can be measured. Experimentally we wish to test some of the predictions from network modeling, particularly the impact of spreading coefficient and the functional form of oil relative permeability at low saturation.

Chapter 4 concerns another important aspect of gas injection processes: the thermodynamics and flow of multicomponent gas/oil mixtures. This section provides a theory for finding the minimum miscibility pressure (MMP) or minimum miscibility enrichment (MME) for reservoir mixtures containing an arbitrary number of components. This work is the general extension of the seminal studies carried out over several years on the method of characteristics theory of gas/oil mixtures.

Chapter 5 provides details of a three-dimensional streamline based reservoir simulator that can handle gravity and changing well conditions for tracer flow, miscible flow and waterflooding. Where comparison with conventional grid-based simulation is possible, the streamline method is up to 100 times faster and more accurate. This offers great promise for improving significantly our ability to predict flow in heterogeneous reservoirs at the field scale. The extension to compositional displacements is planned next under the grant.

2. Use of Network Modeling to Predict Saturation Paths, Relative Permeabilities and Oil Recovery for Three Phase Flow in Porous Media

Darryl Fenwick and Martin Blunt

We present a network model of three phase flow in water-wet porous media. To explain the high oil recoveries in gas injection and gravity drainage experiments, we show that the mechanism for oil recovery is flow through connected oil layers in the pore space that are on the order of a micron thick. We then describe a simple model for the configuration of oil, water and gas in a single pore and present an approximate expression for the conductance of oil layers. We use this expression to derive the oil relative permeability when flow is dominated by layer drainage. We show that for low oil and water saturations $k_{ro} \sim S_o^2$, consistent with the results of several experiments. To predict k_{ro} for the full range of oil saturation we use a capillary equilibrium based network model that can simulate any sequence of oil, water and gas injection. We introduce a self-consistency procedure to ensure that the correct sequence of saturation changes is used in the network model to compute relative permeability. We then present relative permeabilities and oil recoveries for gas injection into different initial oil saturations, and for waterflooding a reservoir containing gas and oil. We show that the relative permeabilities are strongly affected by the fluid properties and by the type of displacement process.

2.1 Introduction

Network models simulate multiphase flow through an idealized representation of the pore space to calculate average properties, such as relative permeability, capillary pressure and oil recovery. Network models can predict multiphase flow properties directly if both the geometry of the porous medium and the displacement process are known precisely [1, 2, 3, 4]. Where a complete description of the flow physics and the pore structure is unknown or difficult to obtain, conceptual models can be developed. These models make approximations about the structure of the pore space and the flow processes. While they cannot make direct predictions of multiphase properties, they can be used to provide insight into flow in porous media. With suitable tuning of parameters, the models can match experimental data and can then be used to make predictions for situations outside the range of available measurements. Examples of this approach include studies of relative permeability hysteresis and the effects of wettability in two phase flow [5, 6, 7, 8, 9]. In this report we use a conceptual model to study three phase flow.

The flow of three phases – oil, water and gas – occurs in a variety of different displacement processes in oil reservoirs and during pollutant transport and clean-up. Although there is now a large body of literature on three phase relative permeability (for example, Oak [10] provides a review of studies up to 1990 and Jerauld [11] provides a recent discussion of measurements in Prudhoe Bay), three phase flow is not well understood, and current empirical models for relative permeability do not adequately describe the full range of possible behavior.

A three phase network model requires knowledge of the pore-scale displacement mechanisms, which are studied using micromodels that reproduce the anticipated behavior in real rock. As a result of these experiments the displacement processes for three phase flow in water-wet media are now fairly well understood [12, 13, 14, 15, 16, 17]. Based on these observations several three phase network models have been constructed [18, 19, 20, 21, 22, 23, 24]. These models have predicted

successfully oil recovery in micromodel experiments [18, 19, 20], and have computed three phase relative permeabilities and capillary pressures [23, 24].

In this report we will present a network model for water-wet media and use it to address two unique aspects of three phase flow. First, oil may form a layer in grooves, crevices, roughness or corners of the pore space, sandwiched between water close to the solid surfaces and gas in the center of the pores. Flow through such layers is the mechanism by which oil may drain to low saturation during gas injection. We will present an approximate analytical model of oil layer conductance and use it to predict oil relative permeability in the layer drainage regime. Second, a three phase displacement involves changes in two independent saturations. This is in contrast to two phase flow (say, oil and water), where the water saturation can only increase (imbibition for a water-wet system) or decrease (drainage). The direction of the saturation change affects relative permeability and capillary pressure. In three phase flow there is an infinite number of possible routes in saturation space all with potentially different relative permeabilities and oil recoveries. In our model we specify a sequence of saturation changes. However, in a macroscopic displacement, normally the boundary conditions are known – the gas and water fractional flows at injection wells and the initial saturation of oil and water in the reservoir. This displacement results in a certain sequence of saturation changes at a fixed point in the reservoir, but the network model does not automatically know what the sequence is. In this report we present a self-consistency procedure that allows the network model to find relative permeabilities for the right saturation path.

First we will discuss the significance of oil layers in three phase flow and describe how the network model computes oil layer conductance. Before describing the network model itself, we show how we can make predictions of oil relative permeability directly from expressions for the oil layer conductance. Then we will introduce the network model. Further details are provided elsewhere [23, 25]. We then describe the self-consistency procedure. Last we will present self-consistent saturation paths and relative permeabilities for gas injection and for waterflooding a reservoir containing oil and gas.

2.2 Oil Films and Layers

Dumoré and Schols [26] showed that low oil saturations can be achieved during gas injection in water-wet rock. Since then, many other authors [27, 28, 29, 30, 31] have studied three phase gas injection and gravity drainage and have all confirmed that very high oil recoveries are possible. Remaining oil saturations as low as 0.1% have been recorded [31]. The mechanism for these high recoveries is oil drainage through connected layers in the pore space. The presence of oil layers is controlled by the spreading coefficient. The initial spreading coefficient for oil C_s^i is:

$$C_s^i = \gamma_{gw} - \gamma_{ow} - \gamma_{go} \tag{2.1}$$

where γ is the interfacial tension of pure fluids before they are brought in contact with each other, and the subscripts g, o and w label gas, oil and water respectively. If $C_s^i > 0$, oil will spread over a flat water surface. If $C_s^i < 0$ it will not. However, fluids in porous media are usually at thermodynamic equilibrium, thus the arrangement of fluid in the pore space is governed by the equilibrium spreading coefficient:

$$C_s^{eq} = \gamma_{gw}^e - \gamma_{ow}^e - \gamma_{go}^e \tag{2.2}$$

where the interfacial tensions are measured for fluids in contact with each other. If $C_s^i > 0$, the gas/water interface will be covered by a film of oil, making γ_{gw}^e significantly lower than γ_{gw}. C_s^{eq} is either zero or negative [32]. C_s^{eq}, the interfacial tensions and the wettability of the rock control the configuration of fluids in the pore space.

Historically, the experiments analyzing hydrocarbon spreading between water and gas have been performed on flat surfaces. If the hydrocarbon spreads, the resulting film over the water surface has been found experimentally and theoretically to be typically of order molecular size. [33, 34, 25] However, in porous media there are grooves, roughness, and corners. Oil in the pore space does not flow through molecular-sized films, that have a negligible conductance, but instead through layers of order microns thick in the pore space wedged between water and gas, as illustrated in Fig. 2.1(a). In this paper we use the word film only to refer to intermolecular films in contrast to layers that are microns across. Several micromodel experiments have confirmed that the pore scale mechanism of oil recovery is through the drainage of oil layers [12, 13, 14, 15, 17, 35, 36]. Oil layers may be present even for $C_s^i < 0$ [17, 36].

We will now make an approximate calculation of how thick the oil layer must be to explain observed drainage rates. Take, as an example, the experiments of Zhou and Blunt [31]. Here oil saturations as low as 0.1% were achieved after three weeks of hexane drainage in a sand column that had a porosity of approximately 0.35. The column had length of 1 m. Clearly the drainage rate is highest at the beginning of the experiment and decreases to almost zero by the end. However, to obtain a typical channel size, we assume that the oil saturation in the top half (0.5 m) of the column decreases by 5% in one week, which is consistent with the experimental data [31]. The oil flow is the saturation decrease times the porosity times the length of column, or $0.05 \times 0.35 \times 0.5 = 8.75 \times 10^{-3}$ m^3 per m^2 per week, which is a Darcy velocity $q = 1.4 \times 10^{-9}$ ms^{-1}. The mean grain diameter of the sand was approximately $d = 500$ μm. We assume that the distance between pores is also 500 μm. Thus the total oil flow in each pore $Q = q \times d^2 = 3.6 \times 10^{-15}$ $\mathrm{m}^3\mathrm{s}^{-1}$. If we assume that the flow is accommodated by a layer of thickness t and width d (the pore size) flowing freely under gravity, then [37]

$$Q = \frac{dt^3}{3\mu}\rho_o g \tag{2.3}$$

where μ is the oil viscosity (approximately 3×10^{-4} $\mathrm{kgm}^{-1}\mathrm{s}^{-1}$ for hexane) and ρ_o is the oil density (659 kgm^{-3}) and $g = 9.81$ ms^{-2}. Solving for t using the data above gives $t \approx 1\mu$m. Again this is consistent with our assertion that oil forms a layer of order a micron across in the pore space. It is possible to perform similar calculations for other experiments – the layer thickness is found to be approximately one micron or larger. Since such low oil saturations are reached, these layers must be well connected throughout the porous medium.

The arrangement of the three fluids in a representative corner of the pore space is shown schematically in Fig. 1. We assume that the oil layers are connected throughout the porous medium. We also assume that the medium is strongly water-wet, such that the oil/water contact angle θ_{ow} is less than or equal to the gas/oil contact angle θ_{go} and that the only curvature of the interface is in the plane of the wedge. For this configuration to be possible, $\theta_{ow} + \beta < \pi/2$ and $\theta_{go} + \beta < \pi/2$, where β is the half-angle of the corner. The oil/water capillary pressure is $P_{cow} = \gamma_{ow}^e / r_{ow}$ where r_{ow} is the radius of curvature of the oil/water interface. Similarly $P_{cgo} = \gamma_{go}^e / r_{go}$ where r_{go} is the radius of curvature of the gas/oil interface. A thick oil layer is present when P_{cow} is large and P_{cgo} is small. The oil layer is assumed to exist until the contact of the oil/water interface with the solid surface coincides with the gas/oil contact, as shown in Fig. 2.1(b). We define a ratio of interfacial curvatures as:

$$R = \frac{r_{ow}}{r_{go}} = \frac{P_{cgo}\gamma_{ow}^e}{P_{cow}\gamma_{go}^e} \tag{2.4}$$

If R is very small, the oil layer can be very thick. The critical ratio R_c at which the layer is no longer stable is:

$$R_c = \frac{\cos(\theta_{go} + \beta)}{\cos(\theta_{ow} + \beta)} \tag{2.5}$$

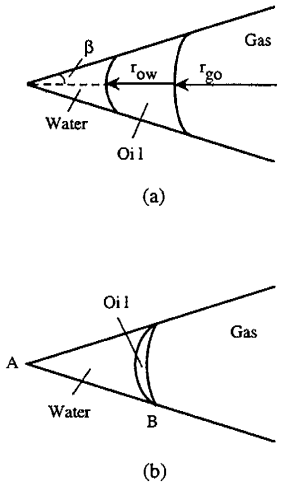

Figure 2.1: (a) Three phases in a corner with half angle β. (b) When the gas/oil and oil/water interfaces touch at point B, the oil layer is assumed to be unstable.

R_c depends only on β and the contact angles. It is independent of the magnitude of the interfacial tensions. If $R < R_c$, then the fluid arrangement resembles Fig. 2.1(a). If $R > R_c$, there is no oil layer, and there is only a gas/water interface with an interfacial tension γ^e_{gw}. Although there might be a molecular-sized oil film present, this film is too thin to have any significant effect on the flow of oil. [38]

For a completely water-wet system it is possible to relate θ_{go} to C_s^{eq}. It is assumed throughout this work that water coats the entire solid surface and the system is strongly water-wet ($\theta_{ow} = \theta_{gw} = 0$). At the gas/oil/water contact, the horizontal force balance of the interfacial tensions is given by,

$$\gamma^e_{gw} = \gamma^e_{go} \cos\theta_{go} + \gamma^e_{ow}. \tag{2.6}$$

Eq. 2.6 can be manipulated, resulting in,

$$\cos\theta_{go} = 1 + \frac{C_s^{eq}}{\gamma^e_{go}}, \tag{2.7}$$

as derived by Kalaydjian [39] and Kalaydjian et al. [29]. Using Eq. 2.7, Eq. 2.5 becomes,

$$R_c = 1 + \frac{C_s^{eq}}{\gamma^e_{go}} - \left(-\frac{C_s^{eq}}{\gamma^e_{go}}\right)^{1/2} \left(2 + \frac{C_s^{eq}}{\gamma^e_{go}}\right)^{1/2} \tan\beta \tag{2.8}$$

Eq. 2.8 is based upon a simple geometric argument for oil layer stability. However, the analysis gives an indication of the expected behavior of oil layers. Layers can be present even for negative spreading coefficients, as shown experimentally [36, 17], but as the spreading coefficient decreases, oil layers become increasingly less likely to exist. Note that whether or not a oil layer exists depends on the value of R which is governed by the ratio of capillary pressures, and on R_c which depends on C_s^{eq}. Thus oil layers may be present for $C_s^{eq} < 0$, and absent for $C_s^{eq} = 0$, depending on the capillary pressures.

2.3 Conductance of Oil Layers

In this section we investigate the expression for the conductance of an oil layer between water and gas. We define a conductance g where the volumetric flow in a single pore is given by $Q = g\Delta\Phi$, where $\Delta\Phi$ is the potential drop across the pore. The conductance of water in a corner (Fig. 2.1) is given by [40]

$$g_w = \frac{A_w r_{ow}^2}{\mu_w l R_{fw}} \tag{2.9}$$

where A_w is the area of water in the corner, l is the length of the pore, and μ_w is the viscosity of water. R_{fw} is a constant dimensionless resistance factor for flow of a single fluid in a corner [40]. This value was calculated by an approximate expression by Zhou *et al.* [41] A_w is given by

$$A_w = r_{ow}^2 \left[\sin\alpha_w \left(\cos\alpha_w + \sin\alpha_w \cot\beta\right) - \alpha_w\right], \tag{2.10}$$

where

$$\alpha_w = \frac{\pi}{2} - \theta_{ow} - \beta. \tag{2.11}$$

If we assume that all three phases in the pore are flowing with the same imposed potential gradient and the water and oil viscosities are assumed equal ($\mu_o = \mu_w = \mu$), then the conductance of an oil layer in a corner is the conductance of both water and oil in the corner minus the conductance of the water, or

$$g_o = \frac{A_c r_{go}^2}{\mu l R_{fo}} - g_w, \tag{2.12}$$

where A_c is the area of water and oil in the corner, g_w is given by Eq. 2.9, and R_{fo} is another dimensionless resistance factor whose value is dependent upon the gas/oil contact angle (θ_{go}) on the water surface. We have ignored viscous coupling between the fluids. For a triangular pore with $\beta = 30°$, $R_{fw} = 31$. If $\theta_{go} = 0$, corresponding to $C_s^{eq} = 0$ from Eq. 2.7, then $R_{fo} = 31$. If $\theta_{go} = 33°$, corresponding to $C_s^{eq} = -4\ mN/m$ from Eq. 2.7, then $R_{fo} = 70$.

A_c is given by

$$A_c = r_{go}^2 \left[\sin\alpha_o \left(\cos\alpha_o + \sin\alpha_o \cot\beta\right) - \alpha_o\right], \tag{2.13}$$

where

$$\alpha_o = \frac{\pi}{2} - \theta_{go} - \beta. \tag{2.14}$$

If there is a no flow boundary at the oil/water interface, a different expression for oil layer conductance is appropriate. Approximate analytical expressions for this case are given by Zhou *et al.* [41]

2.4 Relative Permeability of a Single Pore

Now that we have an expression for oil layer conductance, we can predict the oil relative permeability. We will assume that the porous medium is a bundle of parallel pores of constant cross-section, where every pore has been entered by gas and oil flow occurs only through layers. This layer drainage regime is thus appropriate for low oil and water saturations. While we cannot use this approach to predict exactly the oil relative permeability for a real rock, we will show that the functional form of the relative permeability is consistent with several experimental measurements.

The saturation of a phase is the fraction of the cross-sectional area of a pore occupied by that phase. Eq. 2.13 gives us the area of water and oil in a corner, A_c, and hence:

$$S_w + S_o = \frac{n_c A_c}{A_t} \tag{2.15}$$

where n_c is the number of corners in the pore and A_t is the cross-sectional area of the pore. Similarly, the water saturation $S_w = n_c A_w / A_t$.

If the pore is completely full of one phase, the conductance is approximately [1]:

$$g_t = \frac{\pi r_{eff}^4}{8\mu l}, \tag{2.16}$$

where the effective radius $r_{eff} = 1/2\left(\sqrt{A_t/\pi} + r_i\right)$ and r_i is the inscribed radius of the pore. The oil relative permeability is $k_{ro} = n_c g_o / g_t$.

Using Eqs. 2.12–2.14 it is possible to find k_{ro} as a function of S_w and S_o. We will spare the details, and give an expression for one example, for a pore of equilateral triangular cross-section ($\beta = 30°$) with $\theta_{go} = \theta_{ow} = 0$. In this case, $n_c = 3$, $R_{fw} = R_{fo} = 31$, and

$$k_{ro} = 0.632\left(S_o^2 + 2S_o S_w\right). \tag{2.17}$$

If there is no flow boundary condition between oil and water it is possible to show that the oil relative permeability is [41]

$$k_{ro} = 0.632\frac{S_o^3}{S_o + S_w}. \tag{2.18}$$

When the oil saturation is much smaller than the water saturation, then the functional form of the oil relative permeability depends on the boundary condition at the oil/water interface: $k_{ro} \sim S_o$ if oil and water flow together, Eq. 2.17, while $k_{ro} \sim S_o^3$ for no flow at the oil/water interface, Eq. 2.18. $k_{ro} \sim S_o^3$ is consistent with a classic film drainage expression for oil flow, Eq. (3).

For both Eqs. 2.17 and 2.18, when the oil saturation is of the same magnitude or larger than the water saturation:

$$k_{ro} \sim S_o^2. \tag{2.19}$$

The quadratic form for k_{ro} is readily explained – S_o is proportional to the oil area in the corner ($S_o \sim A_o = A_c - A_w$), while the conductance and hence k_{ro} is proportional to the square of the oil area (A_o^2).

The conceptual picture of oil flowing in layers in the pore space leads to the prediction of quadratic oil relative permeabilities at low saturation – a prediction that is confirmed by a number of experiments. Fig. 2.2 shows the oil relative permeability at low saturation from the experiments of Grader & O'Meara [44] which were performed in glass bead packs with analogue fluids. In these experiments $S_w \approx 6\%$ for $S_o \leq 30\%$, and thus we expect Eq. 2.19 to be valid. At low oil saturation, a best fit of the data gives $k_{ro} \sim S_o^{1.9}$, consistent with layer drainage. In other work, gas injection k_{ro} in a consolidated sandstone also showed quadratic behavior [42]. Similar experiments by Goodyear and Jones [43] again showed the same functional form for the oil relative permeability.

This simple analysis cannot, however, predict k_{ro} for larger values of S_o, where the arrangement of oil-filled pores is important, nor can it determine the effect of spreading coefficient on k_{ro}. Network modeling is necessary to predict the effect of spreading coefficient and to compute relative permeabilities for the full saturation range.

2.5 Network Model

The network model is a cubic lattice of pores connected by throats. All the pores and throats have equilateral triangular cross-sections. The pore and throat radii are chosen from different

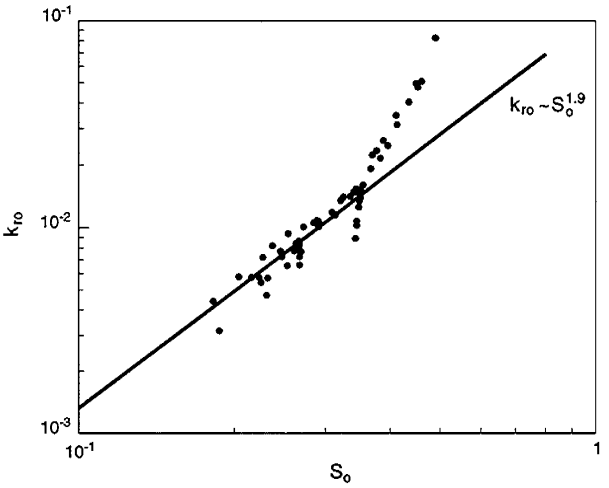

Figure 2.2: Oil relative permeabilities measured in a water-wet system. (from Grader & O'Meara [44] using a glass bead pack and analogue fluids. Included is a line of slope 1.9 on a log-log scale that best fits the k_{ro} data at low S_o.)

distributions. The model consists of $30 \times 15 \times 15$ pores. Fluids are injected at the inlet and displaced through the outlet. There are periodic boundary conditions on the other sides. Saturations and relative permeabilities are computed on the final $15 \times 15 \times 15$ section of the model to avoid inlet effects. We did not observe any outlet effects. Several of the results were also calculated for statistically equivalent, but different realizations, and on $40 \times 20 \times 20$ networks. In all cases, the results were similar. However, there are some examples where finite size effects are important, and these will be discussed later. The model is strongly water-wet and $\theta_{ow} = 0$. The model allows the two phase displacement processes – piston-like throat filling, cooperative pore filling and snap-off – observed in micromodels by Lenormand *et al.* and others and incorporated into previous two phase network models (see, for instance [6, 5].) For three phase flow the displacement processes observed in micromodels [14, 12, 13, 17], including the presence of oil layers, are added in the model. Further details are given elsewhere [23, 25].

We assume that locally the system is in capillary equilibrium, which is appropriate for capillary numbers of around 10^{-7} and lower, where the viscous pressure drop across the network model, including the pressure drops in oil layers, are small in comparison with the capillary pressure. A dynamic three phase network model that has explored the effects of pressure gradients in oil layers has been presented by Pereira *et al* [20]. Our model is accurate only in the limit of very low flow rates. At every stage in the displacement either water, oil or gas is injected to fill one pore or throat. We compute the capillary pressures for all possible two and three phase displacement mechanisms. From this we can compute the entry pressure for each pore and throat. The entry pressure is the pressure of the injected phase necessary to fill a pore or throat, assuming that the other two phase pressures are held constant. We fill the pore or throat with the lowest entry pressure. In this way we can inject oil, gas and water into the network in any order.

Periodically, we compute relative permeabilities. We find the conductance of each phase in every pore and throat and solve for the phase pressures. There are four possible arrangements of fluid in a pore or throat:

1. A pore or throat full of water. Here use Eq. 2.16 for the conductance.

2. A pore or throat containing gas in the center and water in the corners. For the gas phase use

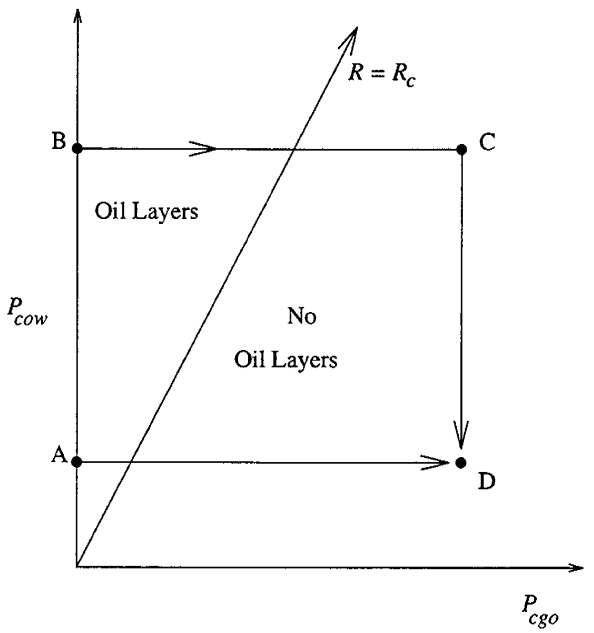

Figure 2.3: Different paths in capillary pressure space. The $R = R_c$ line separates the regions of oil layer stability. Path BCD represents gas invasion into high P_{cow} corresponding to high S_o, followed by imbibition of water. Path AD represents gas invasion into low P_{cow} corresponding to residual oil saturation after water invasion.

Eq. 2.16 but where A_t is replaced by the cross-sectional area of gas in the pore. For water Eq. 2.9 is used, where r_{ow} is replaced by r_{gw}, the gas/water radius of curvature.

3. A pore or throat containing oil in the center and water in the corners. The water conductance is again given by Eq. 2.9, and the oil conductance by Eq. 2.16 but where A_t is replaced by the cross-sectional area of oil in the pore.

4. A pore or throat containing gas in the center, water in the corner and an oil layer. An oil layer is only present if $R < R_c$, Eq. 2.8. The oil layer conductance is given by Eq. 2.12, the gas conductance is the same as for arrangement (2) and the water conductance is the same as for arrangement (3).

2.6 Paths in Capillary Pressure Space

Fig. 2.3 is a schematic diagram representing different three phase displacements as paths in $P_{cgo} - P_{cow}$ space. All oil/water displacements occur on the P_{cow} axis. The point A represents water and waterflood residual oil, while B represents a high oil saturation. When gas is introduced into the system, P_{cgo} is defined. The line $R = R_c$ separates the region where oil layers are stable from the region where oil layers do not exist. R_c is calculated from Eq. 2.8 . Let us consider two different paths ABCD and AD that start and end at the same capillary pressures.

The path AD represents gas injection into residual oil at a fixed value of P_{cow}. Oil layers are present for only a short range of P_{cgo}, and so we expect limited oil layer drainage and little incremental oil recovery. On the other hand, gas injection may result in the formation of an oil bank. At some fixed point in the reservoir, the oil saturation first increases (path AB) before gas

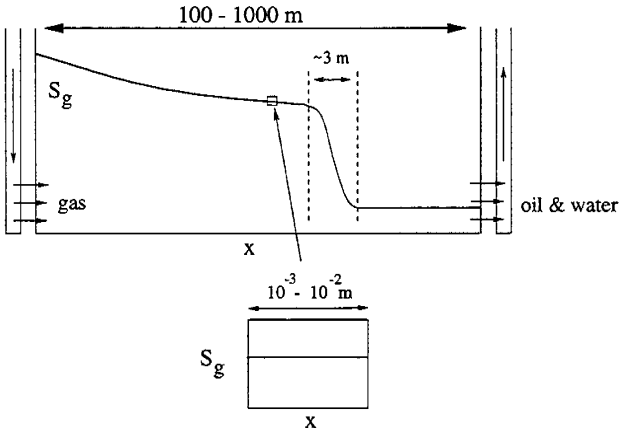

Figure 2.4: Schematic diagram of different scales in multiphase flow in porous media. At the field scale (100–1000 m), the saturation profile is dominated by viscous forces. At much smaller scales (10^{-3}–10^{-2} m), saturations are relatively constant and flow is dominated by capillary forces. Around a length scale of a meter, capillary and viscous forces are approximately the same.

enters the system. Path BC represents gas invasion into the high oil saturation in the oil bank, and oil layers exist until a large value of P_{cgo} is reached. In this case there is a greater opportunity for layer drainage and a lower final oil saturation can be obtained. Path CD represents water injection after gas flooding – while this may give little further oil recovery the oil saturation is likely to be very low already.

In previous work we have used the network model to demonstrate that the route ABCD does indeed give a higher oil recovery than route AD [23, 24]. The relative permeabilities and oil recovery are very sensitive to the sequence of saturation changes. This is principally because of oil layers – when oil layers are present, oil cannot be trapped, but when they are absent, oil may be trapped by both gas and water, leading to poor oil recovery.

What path does the displacement actually follow? One would hope that a network model would be able to predict the sequence of saturation changes for a given displacement. This issue is discussed next.

2.7 Self-Consistent Saturation Paths

Fig. 2.4 illustrates the different length scales for a multiphase flow in a reservoir. The network model represents a small portion of rock over which the saturations are approximately constant and capillary forces dominate. However, over larger scales, the competition between viscous and capillary forces leads to changes in saturation over a few meters. On the reservoir scale, viscous forces dominate. Thus we use a network model that assumes capillary equilibrium to study flow at the pore level. To compute flow on the reservoir scale, we may use a conventional numerical simulator, where to a reasonable approximation capillary forces may be ignored. The link between the pore-level and the field-scale is provided by using relative permeabilities from the network model in the numerical simulator.

The network model computes relative permeability for a particular saturation path. With known initial saturations in the reservoir and injection conditions, we can use the relative permeabilities derived from the network model in a conventional field-scale numerical simulator to predict the sequence of saturation changes in the reservoir. The saturation path computed by the

simulator is dependent upon the initial conditions, injection conditions, viscosities of the phases, and gravitational forces. The saturation path from the numerical solver and the saturation path used by the network model may not be the same.

If the paths from the network model and the numerical solver are not the same, then the sequence of pore-level displacements does not represent the proper sequence for the particular macroscopic displacement that is being investigated. In order to find the correct saturation path, the iteration procedure shown schematically in Fig. 2.5 is used. The procedure is as follows:

1. With the network model and a specified pore size distribution, perform a three phase displacement with a guessed saturation path from initial to injection conditions.

2. The displacement produces a set of three phase relative permeabilities. The three phase relative permeabilities are tabulated as functions of their own saturation for the selected path.

3. The tabulated values are input into a one-dimensional, three phase Buckley-Leverett numerical solver with given injection conditions and phase viscosities.

4. Stop the simulator after a sufficient amount of time such that any shocks and rarefaction waves are resolved. Find the saturation path by plotting the saturations of all the grid blocks on a ternary diagram. For a Buckley-Leverett problem, the saturation is a function of x/t only. Thus the saturation path measured by taking the saturations in each grid block at a fixed time is the same as the sequence of saturation changes in a fixed grid block over time.

5. Compare the saturation paths of the network model and the numerical simulation. If the saturation values along the two paths differ by less than 1%, we consider them identical.

6. If the paths are not identical, return to step 1. The saturation path for the network model is that obtained from the numerical solver. If the paths coincide, stop.

When the iteration is complete, the three phase relative permeabilities calculated by the network model are self-consistent. This means that the network model computes relative permeabilities for a sequence of saturation changes that is the same as the sequence that results from a one-dimensional field-scale simulation using the same relative permeabilities.

This procedure gives us valid predictions of relative permeabilities for one-dimensional, homogeneous displacements. However, for heterogeneous, three-dimensional flows, the saturation paths may be different in different regions of the reservoir. Coupling pore scale modeling directly to three-dimensional reservoir simulation remains an unresolved research issue.

2.8 1D Numerical Solution

The numerical simulations are performed using an explicit, three phase numerical simulator using a total variation diminishing (TVD) scheme. [45] The scheme is second-order accurate in space and first-order accurate in time. Two mass balance equations are solved simultaneously:

$$\frac{\partial S_w}{\partial t} + \frac{\partial f_w}{\partial x} = 0, \tag{2.20}$$

and

$$\frac{\partial S_g}{\partial t} + \frac{\partial f_g}{\partial x} = 0, \tag{2.21}$$

where,

$$f_w = \frac{\lambda_w}{\lambda_t}, \tag{2.22}$$

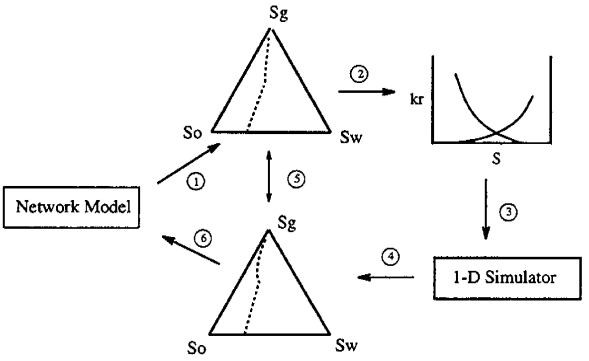

Figure 2.5: Schematic diagram of iteration procedure to obtain self-consistent relative permeability values. (1) A saturation path through the three phase region is guessed and followed with the network model. (2) During the displacement, three phase relative permeability values are calculated. (3) These relative permeability values are input into a 1-D numerical simulator with selected initial conditions, injection conditions, and fluid properties. (4) The 1-D simulator generates another saturation path. (5) This path is compared to the proposed path with the network model. (6) If the paths do not coincide, repeat the procedure, using the path from step 4 in the network model.

$$f_g = \frac{\lambda_g}{\lambda_t}, \tag{2.23}$$

$$\lambda_w = \frac{k_{rw}}{\mu_w}, \qquad \lambda_o = \frac{k_{ro}}{\mu_o}, \qquad \lambda_g = \frac{k_{rg}}{\mu_g}, \tag{2.24}$$

and

$$\lambda_t = \lambda_w + \lambda_o + \lambda_g. \tag{2.25}$$

x represents dimensionless distance and t is the number of pore volumes of injected fluid. Eqs. 2.20 and 2.21 assume incompressible, one-dimensional flow where we have ignored gravity and capillary forces. Capillary forces are assumed to be neglible at the field-scale, even though they dominate at the scale of the network model. For the cases we consider we will assume horizontal gas or water injection with no gravity – however, gravity can easily be accommodated in the one-dimensional conservation equations if required.

2.9 Gas Injection

We will now present self-consistent relative permeabilities for gas injection into different initial saturations of oil and water. $f_g = 1$ is specified at the inlet. The viscosities are

$$\mu_o = 1\,cp, \quad \mu_w = 1\,cp, \quad \text{and} \quad \mu_g = 0.1\,cp.$$

Note that the self-consistent paths are only valid for this set of phase viscosities.

Runs are performed for $C_s^{eq} = 0$ and $C_s^{eq} = -4\ mN/m$. $C_s^{eq} \approx 0$ represents light alkanes and some oil mixtures, such as Soltrol, while $C_s^{eq} = -4\ mN/m$ is the value for a decane/water/air system [46]. These spreading coefficients span a plausible range for light crude oils at reservoir conditions, although reliable estimates of spreading coefficients in these circumstances are not available.

The displacements start with the network filled with water. Oil is injected until a specified oil saturation is reached. The resulting S_w and S_o are the initial saturations for gas injection into the

network, and for the numerical solution. Then gas injection is simulated, and the iteration procedure is followed. Up to 12 iterations may be required until self-consistent relative permeabilities are found, although typically self-consistent paths are found in only four iterations. Note that the self-consistent path may involve the injection of water and oil into the network model, as well as gas.

The relative permeabilities are a function not only of saturation and saturation path, but also depend on the pore scale configuration of fluid. The relative permeabilites here are computed for secondary gas injection – that is gas injection after primary drainage of oil. Tertiary gas injection – gas injection after waterflooding – starts from different pore level arrangements of fluid and thus may give different relative permeabilities.

$C_s^{eq} = 0$ Results

Fig. 2.6 shows the self-consistent saturation paths for gas injection into five different combinations of initial oil and water saturations (denoted S_{oi} and S_{wi} respectively). As a comparison Fig. 2.6 also contains experimental saturation paths obtained by Grader & O'Meara [44]. Grader & O'Meara used analogue fluids – n-decane ($\mu = 0.735$ cp) was used in place of gas, and benzyl alcohol ($\mu = 4.984$ cp) in place of oil. The water viscosity was 1.140 cp. For this fluid system, $C_s^i = 2\ mN/m$. It is assumed that $C_s^{eq} \approx 0$. The porous medium was a glass bead pack, with n-decane (gas) invading into different initial saturations of benzyl alcohol (oil). Fig. 2.2(a) shows k_{ro} for the same experiments.

No attempt has been made to match the experiments. The pore size distribution used in the network model is not intended to be representative of a glass bead pack, and the viscosities of the fluids are different. The experimental data is provided for qualitative comparison only. However, several common features between the network model results and the experiments can be noted:

- At high oil saturations, oil is more mobile than water. Thus, the gas preferentially invades into the oil until S_o is significantly reduced.

- Similarly, when S_o is low, the gas preferentially displaces the more mobile water until S_w is low.

- Different initial conditions follow similar paths in the three phase region, especially at low values of S_o.

An important difference between the experiment and the network model results is that Grader & O'Meara observed a shock in the two phase region ahead of the invading gas (n-decane) for an initial oil (benzyl alcohol) saturation of 48%. Two phase shocks are not found with the network model for the gas injection cases studied.

Fig. 2.7 shows the capillary pressure paths. Notice that the paths remain in the region of oil layer stability and thus oil is not trapped, and eventually it can all be displaced. Comparison of Fig. 2.7 with Fig. 2.3 indicates that the capillary pressure paths taken in Fig. 2.3 do not correspond to field-scale gas injection. Paths such as in Fig. 2.3 that force certain values of P_{cow} or lower to be maintained, and allow oil to be trapped, must correspond to a displacement where both gas and water are injected to displace oil. Only through the injection of water can a fixed value of P_{cow} be maintained.

Fig. 2.8 shows the self-consistent gas relative permeabilities for the saturation paths shown in Fig. 2.6. The k_{rg} curves are very similar, and virtually identical at higher saturations. Experiments by Oak [47] also found that k_{rg} values were similar at high S_g for various initial conditions. Note that at low gas saturations, the curves have a step-like character, which is due to the finite size of the network.

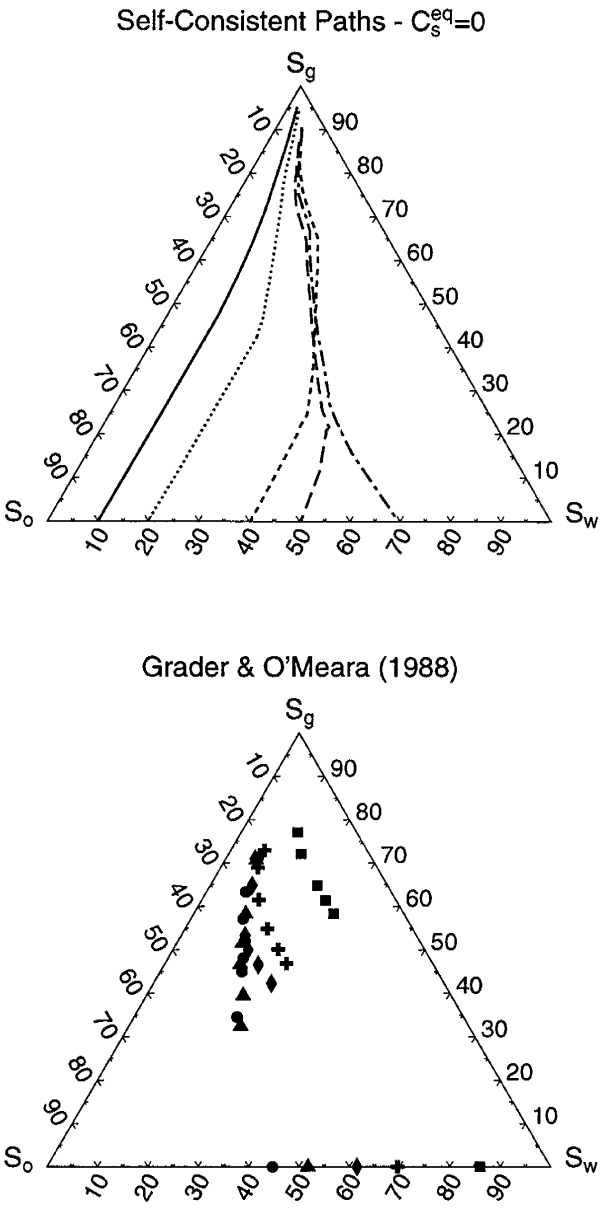

Figure 2.6: Top plot: Self-consistent saturation paths for gas injection into oil and water. Bottom plot: Gas injection experiments performed by Grader & O'Meara [44] using a glass bead pack and analogue fluids. The experimental data is provided for qualitative comparison only.

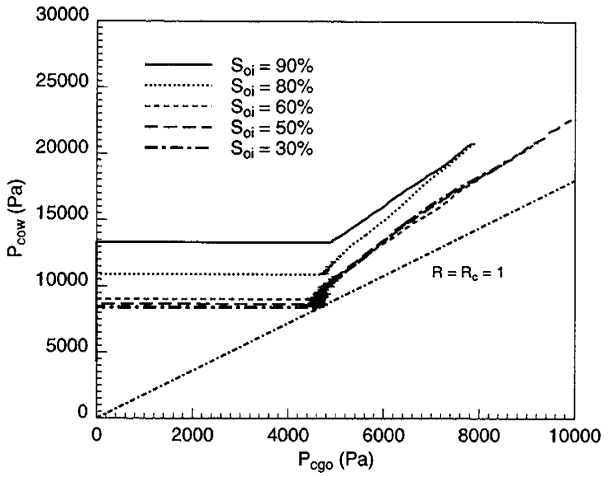

Figure 2.7: Capillary pressure paths for gas injection into different values of initial oil saturation (S_{oi}).

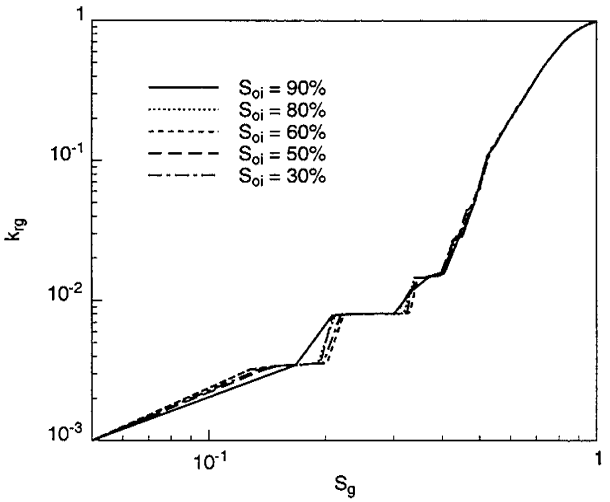

Figure 2.8: Self-consistent k_{rg} curves for the saturation paths in Fig. 2.6. Note that the step-like character of the k_{rg} curves at low S_g is due to finite-size effects.

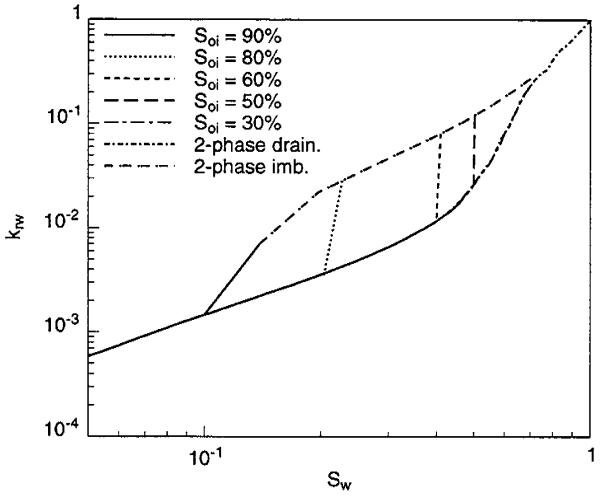

Figure 2.9: Self-consistent k_{rw} curves for the saturation paths in Fig. 2.6. The curves overlap when flow is dominated by water drainage through the corners of the pore space.

The self-consistent water relative permeability curves are given in Fig. 2.9. For reference, the two phase relative permeability curves are also included. If the self-consistency procedure required values of k_{rw} at $S_w > S_{wi}$, the two phase imbibition k_{rw} values were used. For $S_w < S_{wi}$, the k_{rw} curves are very similar for all values independent of S_{oi}, and correspond to the k_{rw} curve for two phase drainage. Several three phase experiments have also shown that k_{rw} curves are similar for different initial conditions. [48, 49, 47, 10] At low S_w the drainage curves show a straight line on the log–log plot, indicating that the flow is dominated by flow in corners.

Fig. 2.10 shows the self-consistent oil relative permeability curves. There is a very rapid change in k_{ro} at large values of S_o, which is controlled by the arrangement of pores and throats filled with oil, followed by a less dramatic decrease at low S_o, in the layer drainage regime. At low S_o the k_{ro} curve has a slope of between 1 and 2 on the log-log plot in accordance with the expression for oil layer conductance, Eq. 2.12. The shape of the k_{ro} curve is similar to the experimental results in Fig. 2.2. Unlike the k_{rw} and k_{rg} curves, k_{ro} is different for different initial conditions. This indicates that k_{ro} cannot be written as a function of S_o alone. Similar functional forms for k_{ro} have been found experimentally [50, 48, 49, 47, 10].

To illustrate why k_{ro} is a function of both S_o and S_{oi}, consider k_{ro} at $S_o = 0.4$ for $S_{oi} = 0.9$ and $S_{oi} = 0.6$. From Fig. 6, when $S_o = 0.4$, $S_w = 0.1$ and $S_g = 0.5$ for $S_{oi} = 0.9$, while for $S_{oi} = 0.6$ S_w is larger (0.4) and S_g is smaller (0.2). To a good approximation gas occupies the largest pores and water the smallest, while oil fills those of intermediate size. This means that higher water saturations force oil to occupy larger pores. Hence for $S_{oi} = 0.6$ the oil occupies larger pores than for $S_{oi} = 0.9$, which in turn leads to a larger k_{ro}. Experiments by Skauge *et al.* [51] have also found that k_{ro} increases for decreasing S_{oi}. This effect is evident in Fig. 2.10. However, this example ignores the effect of oil flow through layers, which influences the k_{ro} values in Fig. 2.10. If S_{oi} is low, the oil can be very poorly connected and have a very dentritic structure which tends to reduce k_{ro} disproportionately. This also affects k_{ro}. Thus, the $S_{oi} = 30\%$ curve in Fig. 2.10 is below the curves for $S_{oi} = 80\%$ and $S_{oi} = 60\%$.

The finite size of the network affects the k_{ro} calculations. Some of the curves in Fig. 2.10 have been smoothed by interpolation between selected points before input in the numerical simulator, to ensure that the numerical model was stable.

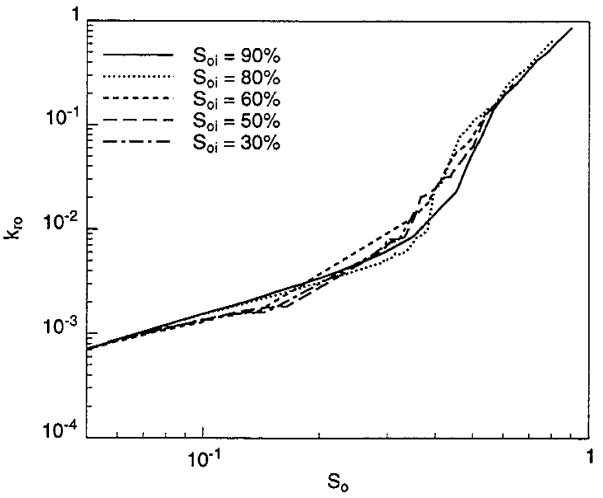

Figure 2.10: Self-consistent k_{ro} curves for the saturation paths in Fig. 2.6. Flow at low oil saturation is governed by flow through layers. When oil flows through oil-filled pores and throats, the relative permeability curves differ for different initial conditions. Note the qualitative similarity with the experimental results in Fig. 2.2.

Fig. 2.11 shows the average oil saturation over all the grid blocks in the numerical solver as a function of the pore volumes of gas injected. The plots are determined by the TVD solution with 500 grid blocks. Eventually all the oil can be recovered, but only after the injection of a huge amount of gas.

$C_s^{eq} = -4$ mN/m Results

Displacements for $C_s^{eq} = -4\ mN/m$ were simulated for initial conditions at $S_{oi} = 90\%$ and $S_{oi} = 30\%$. Fig. 2.12 gives the self-consistent saturation paths. For comparison, the $S_{oi} = 90\%$ and $S_{oi} = 30\%$ paths for $C_s^{eq} = 0$ are included. The $S_{oi} = 30\%$ path stops at an oil saturation of 23.4%. The $S_{oi} = 90\%$ path is similar to the path at $C_s^{eq} = 0$. At high S_g the $C_s^{eq} = 0$ path displaces more oil, which is due to the effect of C_s^{eq} upon k_{ro} values at low S_o.

Again there is no trapped oil. For $S_{oi} = 30\%$ when the displacement was stopped, all the oil is surrounded by gas, with water found only in the corners of the pore space. If the displacement in the network model were allowed to continue the capillary pressure path would proceed along the $R = R_c$ line, very slowly displacing all the oil from the network.

The self-consistent k_{ro} values are shown in Fig. 2.13. At high S_o, the $S_{oi} = 90\%$ curves are very similar for both values of C_s^{eq}. At low S_o, the $C_s^{eq} = -4\ mN/m$ curve lies consistently below the $C_s^{eq} = 0$ curve. Oil flow through layers for $C_s^{eq} = -4\ mN/m$ has a smaller conductance because the ratio of interfacial curvatures (R) is much closer to the critical value R_c than for the displacement at $C_s^{eq} = 0$. The lower k_{ro} values will have an impact upon the rate of oil recovery. For the $S_{oi} = 30\%$ displacement at $C_s^{eq} = -4\ mN/m$, oil layers are not stable all the time. Thus, the oil that reconnects at the beginning of the displacement becomes disconnected again as the displacement continues, similar to the AD path discussed in Fig. 2. The final oil saturation when the displacement ceases is 23.4%. For this condition, a simple linear interpolation from the last finite k_{ro} value to $k_{ro} = 0$ at $S_o = 23.4\%$ is added. Note that the k_{ro} value at $S_o = 23.4\%$ should be finite, reflecting the very slow displacement of oil as the capillary pressure path oscillates along the $R = R_c$ line for oil layer stability. Notice that the absence of the layer drainage regime for

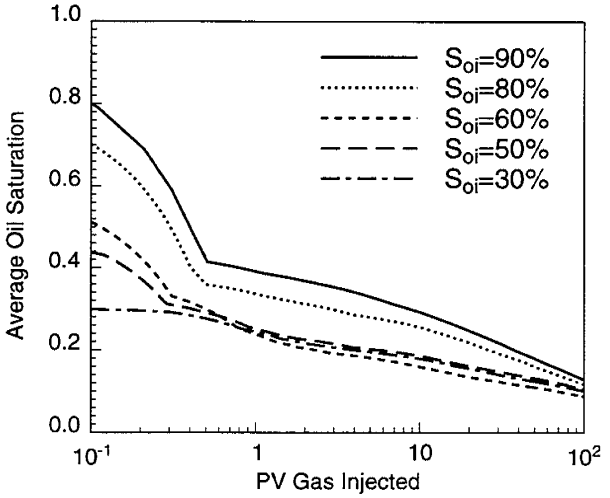

Figure 2.11: The average oil saturation during gas injection for $C_s^{eq} = 0$. The curves were calculated using the TVD solver with 500 grid blocks.

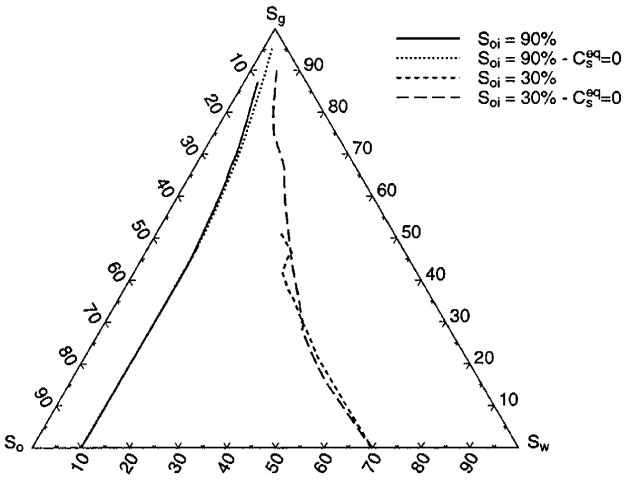

Figure 2.12: Self-consistent saturation paths for gas injection into oil and water with $C_s^{eq} = -4$ mN/m, with gas injection into $S_{oi} = 90\%$ and $S_{oi} = 30\%$ for $C_s^{eq} = 0$ included for comparison.

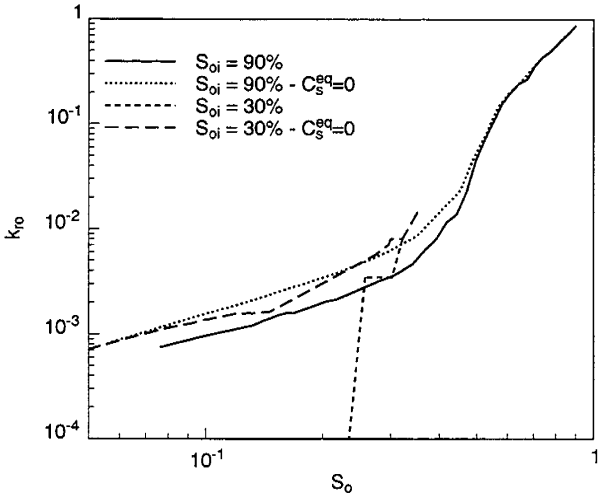

Figure 2.13: Self-consistent k_{ro} curves. At low S_o, k_{ro} values for $C_s^{eq} = -4\ mN/m$ are lower because the displacement is closer to the region of layer instability than for $C_s^{eq} = 0$. k_{ro} values for gas injection into $S_{oi} = 30\%$ are not finite throughout the entire displacement. However, oil is displaced to 23.4% saturation. The k_{ro} curve is constructed by interpolating the last finite value of the k_{ro} curve to zero at $S_o = 23.4\%$.

$S_{oi} = 30\%$ is qualitatively in agreement with the experimental measurements shown in Fig. 2(d). In comparison with $C_s^{eq} = 0$, k_{rg}, k_{rw}, (not shown here) and k_{ro} are all more sensitive to S_{oi}. This is due to the more complex behavior when $\theta_{go} > 0$ and oil is not completely wetting in the presence of gas.

Fig. 2.14 shows the recovery curves for the $S_{oi} = 90\%$ and $S_{oi} = 30\%$ paths at the two C_s^{eq} values. Recovery is more rapid for $C_s^{eq} = 0$ due to the higher k_{ro} values at low S_o.

Figs. 2.11 and 2.14 illustrate an important point regarding the concept of oil recovery and residual oil saturation. For the gas injection examples given, there is no residual oil saturation. However, an immense quantity of gas is required to reduce the oil saturation to very low values. This finding suggests perhaps that reported measurements of S_{or} for gravity drainage and gas injection experiments are incorrect, and that S_o would continually decrease if the experiment were allowed to continue. Fig. 2.14 also illustrates the sensitivity of oil recovery to C_s^{eq}. Fig. 2.14 indicates that after approximately 10 pore volumes of gas is injected into $S_{oi} = 30\%$, the fraction of original oil in place recovered for $C_s^{eq} = 0$ is twice the amount for $C_s^{eq} = -4\ mN/m$.

2.10 Three Phase Waterflood

Self-consistent three phase relative permeabilities for water injection into a reservoir containing water, oil and gas are presented. $f_w = 1$ is specified at the inlet, and the viscosities are the same as is used for gas injection. A single run is shown representing the waterflood of a reservoir containing oil and gas. For this case, $C_s^{eq} = 0$. The displacements start with the network filled with water. Gas invades into the network up to $S_g = 80\%$. Oil subsequently invades into the network, displacing the gas, until $S_o = 30\%$, $S_g = 50\%$, and $S_w = 20\%$. This is the initial condition of the reservoir. Oil is found in layers and in the centers of some intermediate-sized throats and pores. At this point, water injection commences, and the self-consistency procedure is followed. The results given below were determined in three iterations. Fig. 2.15 shows the saturation path. Point A is

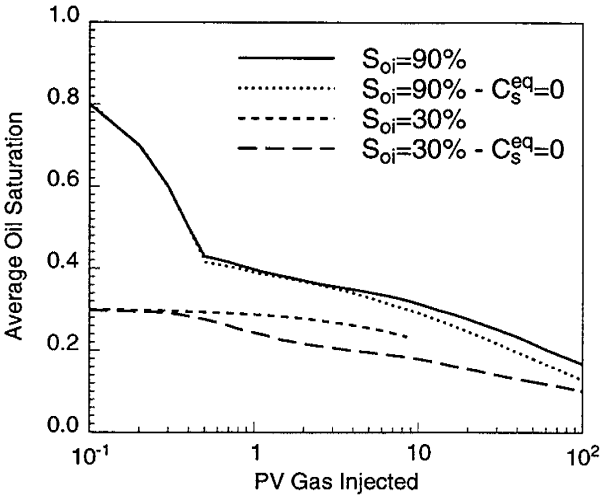

Figure 2.14: The average oil saturation during gas injection for $C_s^{eq} = -4\ mN/m$. The $S_{oi} = 90\%$ and $S_{oi} = 30\%$ paths for $C_s^{eq} = 0$ are included for reference. The curves were calculated using the TVD solver with 500 grid blocks.

the initial condition. The final saturations are given by point C. At point C, $S_w = 47.4\%$, $S_o = 7\%$, and $S_g = 45.6\%$ – both oil and gas are trapped. The path from A to Point B represents an oil bank ahead of the invading water front. Note that the advancing oil bank traps the gas, and the oil is subsequently trapped by the advancing water. The capillary pressure path is given in Fig. 2.16. Note that the displacement occurs in the region of oil layer stability. Since oil layers are stable, the oil acts as a wetting fluid. Thus, the oil can rapidly disconnect the gas by snap-off. At B, the gas is trapped. Water invades into oil. At C, oil layers are stable, but some oil is trapped because the gas is also trapped – oil can only flow if there are connected paths of pores that are either oil-filled or contain oil layers.

The oil relative permeability curve for the self-consistent path in Fig. 2.15 along with the k_{ro} for gas injection into $S_{oi} = 90\%$ are shown in Fig. 2.17. The k_{ro} curves are very different. Significant hysterisis is also seen in the gas and water relative permeabilities.

Fig. 2.18 shows the average oil saturation as a function of pore volumes of water injected. Oil recovery is slow initially when the gas is being displaced. As more gas becomes trapped, the oil production increases until the oil is trapped. The ultimate recovery of oil is 76.7% as a fraction of original oil in place. Note that the rate of recovery is more rapid than gas injection (see Fig. 2.11). Although the ultimate recovery of oil through gas injection is higher, over 100 pore volumes of gas would have to be injected to reach the same average oil saturation.

2.11 Conclusions

1. The mechanism for high oil recovery during gas injection is drainage of connected oil layers in the pore space. These layers are of order microns in thickness, wedged between water and gas in the pore space. Such layers can exist even if the spreading coefficient is negative.

2. Layer drainage leads to a characteristic form for the oil relative permeability at low saturation. If both the oil and water saturations are small $k_{ro} \sim S_o^2$, with no residual oil saturation, as observed in many experiments.

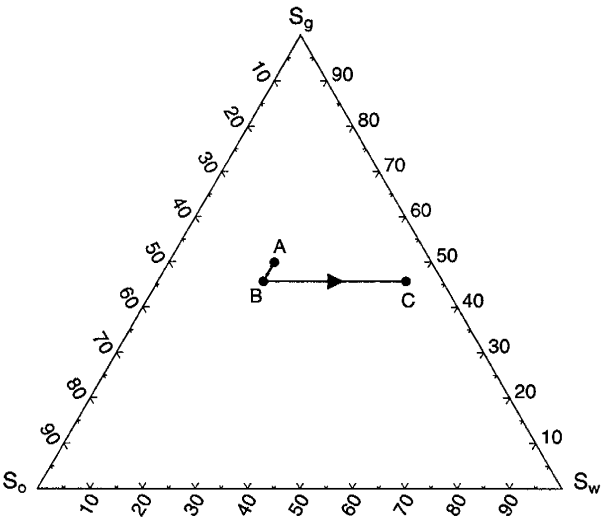

Figure 2.15: Self-consistent saturation path for imbibition into $S_o = 30\%$, $S_w = 20\%$, and $S_g = 50\%$. Point A is the initial condition. The path from A to B is an oil bank ahead of the water front. Point C is the final saturations where both oil and gas are trapped. At point C, $S_w = 47.4\%$, $S_o = 7\%$, and $S_g = 45.6\%$.

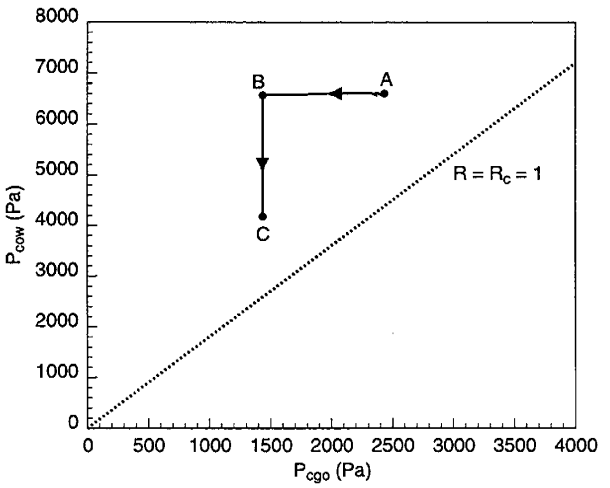

Figure 2.16: Capillary pressure path for the waterflood gas condensate example. Point A is the initial condition. Point C is the final condition at which oil and gas are both trapped. The path from A to B is an oil bank ahead of the invading water.

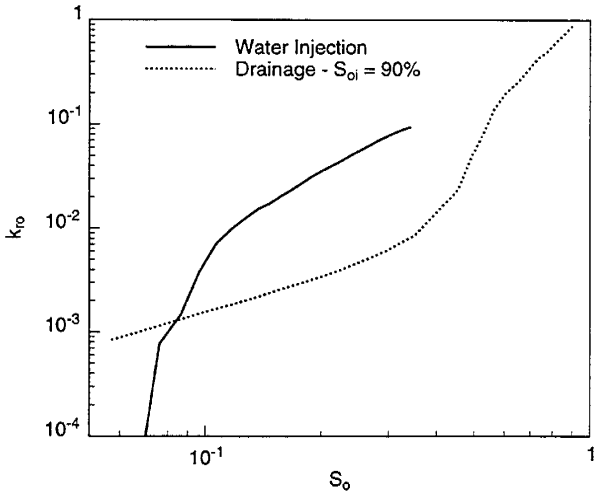

Figure 2.17: The self-consistent k_{ro} curve for water injection into a gas-condensate reservoir. k_{ro} for gas injection into $S_{oi} = 90\%$ is included for comparison.

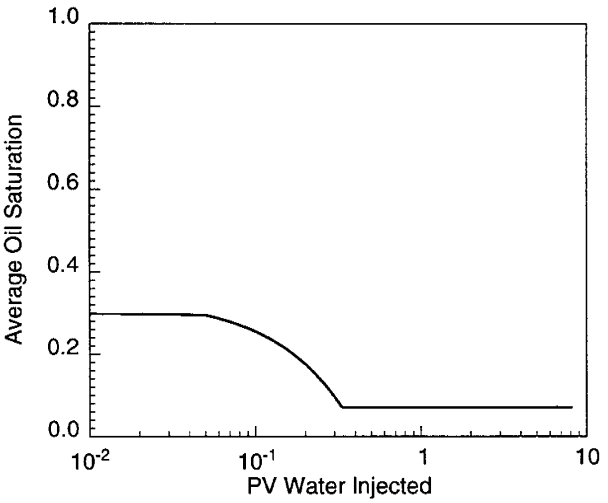

Figure 2.18: The average oil saturation for water injection of a gas condensate reservoir.

3. The computation of self-consistent saturation paths and relative permeability allows the network model to make predictions of multiphase flow properties for any type of displacement process.

4. The saturation paths and relative permeabilities computed for gas injection into different initial oil saturations show qualitatively similar features to experimental measurements. In particular, for a given fluid system, the water and gas relative permeabilities are similar for different initial conditions, while the oil relative permeability is not. The oil relative permeability shows a rapid decrease with oil saturation at large S_o and then a transition to the layer drainage regime.

5. The relative permeabilities and the rate of oil recovery are functions of equlibrium spreading coefficient.

6. The oil, water and gas relative permeabilitites for gas injection are all different from those for three phase waterflooding.

The next step of our work is to experimentally test some of the predictions of the network model, namely the quadratic form of k_{ro} at low s_o, and the effect of the spreading coefficient. This is discussed in the next section.

3. Three-Phase Flow Experiments

Akshay Sahni, Dengen Zhou, Jon Burger and Martin Blunt

This research presents a framework for analyzing three phase flow experiments in porous media. We obtain in-situ measurements of phase saturations from three phase gravity drainage experiments using a CT Scanner. We perform these experiments with both consolidated and unconsolidated sands and with different spreading and initial conditions. Three phase relative permeabilities are computed for each of these experiments using in-situ measurements of phase saturations. We also analyze data from a previously published dynamic displacement experiment [44], where three phase relative permeabilites have been measured. Once the three phase relative permeabilities are known, we calculate analytically the saturation paths and recoveries for the experiments.

3.1 Motivation

The simultaneous flow of three immiscible fluids in porous media is an essential component of enhanced oil recovery and aquifer remediation processes. It is important to understand three phase flow for designing optimum methods for recovering oil by gas injection, gas gravity drainage, surfactant flooding and thermal recovery.

At Stanford, we are trying to get a better understanding of three phase flow, from the pore scale upwards. Over the past few years, research on three phase flow has primarily focussed on:

- two and three phase gravity drainage in capillary tubes
- three phase flow in micromodels
- three phase network modeling
- mathematics of three phase flow

From three phase flow in capillaries we can study the flow of oil as thin layers in an idealized context [41]. Micromodel studies of three phase flow allow us to study pore level processes [17]. Three dimensional and three phase network modeling can give us estimates of relative permeability and capillary pressures for a variety of different three phase flow processes and for different fluid systems [52] (see chapter 2 of this report). Finally, if we can correctly predict the three phase relative permeabilities, we have the mathematical ability to compute the saturation paths and recoveries analytically [78, 79].

This research provides a good conceptual picture of several three phase flow phenomena, yet, it is still essential to look at three phase flow behavior in an actual porous medium. Although work has been done to understand three phase flow at the core scale, most of the published literature does an inadequate job of analyzing three phase flow experiments. It is our objective to bridge this gap between experiment and theory of three phase flow in porous media.

At Stanford, we now have a unique experimental capability - a dual energy CT scanner that can operate in both horizontal and vertical mode. This enables us to obtain in-situ measurements of phase saturations and compute three phase relative permeabilities. To study three phase flow at the core scale, we propose to perform and model analytically a series of three phase gravity drainage experiments in both consolidated and unconsolidated porous media. We will also look at systems with different spreading and initial conditions. Then we hope to relate the results obtained from our experiments to those obtained from capillary tubes, micromodels and network modeling. We also extend our theoretical framework to analyze three phase dynamic displacement experiments [44] and construct solutions to three phase flow problems analytically.

3.2 Literature Review

Although three phase flow experiments are hard to perform, there are many published studies. Grader and O'Meara [44] performed dynamic displacement experiments using three immiscible fluids. Virnovsky [53] and Grader and O'Meara [44] developed a theory to obtain three phase relative permeability as a function of saturation by an extension of the Welge [54] and JBN [55] methods to three phases. Siddiqui *et. al* [56] verified the theory using X-ray computerized tomography to obtain in-situ saturations for three phase dynamic displacement experiments. Sarem [57] obtained three phase relative permeability by unsteady state displacement experiments assuming that relative permeability of each phase was a function of its own saturation. Oak *et. al* [58] presented a steady-state study of three phase relative permeability using fired Berea cores. Minssieux and Duquerroix [59] analyzed water alternating gas experiments in porous media with residual oil.

Three phase gravity drainage experiments have shown that it is possible to obtain very low residual oil saturations [26, 27, 60, 31]. Vizika and Lombard [61] studied the effects of wettability and spreading characteristics of the fluid system in three phase gravity drainage. Skurdal *et. al* [30] analyzed gas gravity drainage experiments using spreading and non-spreading systems under oil wet, water wet and mixed wet conditions. Naylor *et. al* [62] performed gravity drainage experiments by measuring in-situ oil and brine saturations using a radioactive tracer technique. Chalier *et. al* [63] used a gamma-ray absorption technique to obtain three phase relative permeability for tertiary gas gravity drainage experiments. Skauge *et. al* [64] summarized results from gas gravity drainage experiments at different water saturations. Espie *et. al* [65] established and interpreted laboratory data quantifying the dynamics of oil bank growth during the waterflood/gravity drainage interaction in Prudhoe Bay cores.

In three phase flow, oil may form layers in crevices and roughness of the pore space, between water and gas. It is the drainage of these layers that is responsible for the good recoveries observed in gravity drainage experiments (Blunt *et. al* [38]). Although the residual oil saturation is very low, the relative permeability at low oil saturations may also be very small, making gas injection schemes uneconomic over any reasonable time scale. It is therefore important to have a good understanding of the three phase relative permeability, especially at low oil saturation.

Most numerical models of three phase flow in porous media use empirical relationships for capillary pressure and relative permeability [66, 67, 68, 69, 70]. Delshad and Pope [72], Oak [58] and Fayers and Matthews [73] compared empirical models to published experimental data and showed that in most cases the empirical models fail to match the measurements.

In the next section 'Dynamic Displacement Experiments', we describe our analysis of the displacement experiment of Grader and O'Meara [44]. We then present our analysis of gravity drainage experiments and detail the proposed research.

3.3 Dynamic Displacement Experiments

Overview

We use data from a dynamic displacement experiment (Grader and O'Meara [44]). The method of characteristics (MOC) is used to calculate analytically saturation paths and recoveries for three phase displacements in one dimension once the relative permeabilities are known (see Guzman and Fayers [78] and references therein for a discussion of MOC theory applied to three phase flow). In contrast with previous work we find MOC solutions for experimentally measured relative permeabilities, rather than assuming, a priori, some empirical model. In other words, rather than attempting to force a pre-conceived model on the data, in this work we find the simplest functional form of relative permeability that adequately matches the data.

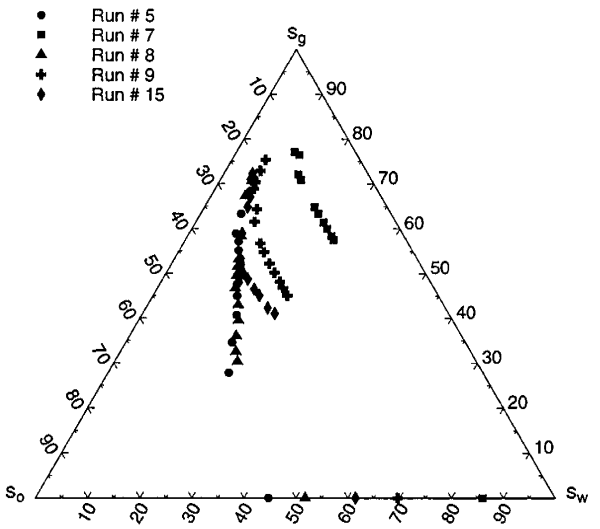

Figure 3.1: Saturation trajectories from Grader and O'Meara's experiments

Experiment Description

The fluids used in Grader and O'Meara's experiments [44] were water, benzyl alcohol and decane, and the porous medium was composed of glass beads with 140-200 mesh sizes. Decane (viscosity = 0.735 cp) was used in place of gas, to reduce viscous fingering effects, and benzyl alcohol was the oil phase. The viscosities of water and benzyl alcohol were 1.140 cp and 4.984 cp respectively. The initial spreading coefficient for oil was 0.2 mN/m. The interfacial tensions were about an order of magnitude less than typical gas-oil-water systems to reduce capillary end-effects. A three phase dynamic displacement experiment was initiated by saturating the porous medium totally with water and then flooding it with oil until the irreducible water saturation was reached. Uniform two phase saturation in the core was obtained by injecting a given fractional flow of oil and water to reach steady state. At this point, the injection of gas (decane) was started.

Virnovsky [53] and Grader and O'Meara [44] extended the Welge/JBN [54, 55] method for determination of two phase relative permeability to three phases. Details of calculating the saturation of a particular phase at the outlet end and the corresponding phase relative permeability are provided in these papers. Several experiments were performed with different initial water saturations, and the saturation trajectories obtained are shown on the ternary diagram, Fig. 3.1.

Analysis of the Experiment

The three phase relative permeabilities obtained by Grader and O'Meara are shown plotted as a function of their own saturations in Fig. 3.2. To a good approximation the relative permeability values lie on a single curve and hence appear to be a function of their own saturation.

In order to have a convenient functional form of relative permeabilities, we matched them to the following polynomial:

$$k_{rp} = As_p + Bs_p^2 + Cs_p^3 + Ds_p^4 + Es_p^5 \tag{3.1}$$

where the subscript p labels the phase (oil, water or gas).

The matching parameters A, B, C, D and E were found by a least-squares fit to the data. Table 3.1 shows the values obtained. If Eq. (1) predicts $k_{rp} < 0$, we set $k_{rp} = 0$. Recently Hicks *et. al* [74] analyzed similar experiments and showed that Stone model I and II [68, 69] relative permeabilities could not match the experimental recoveries very well. They got better results by

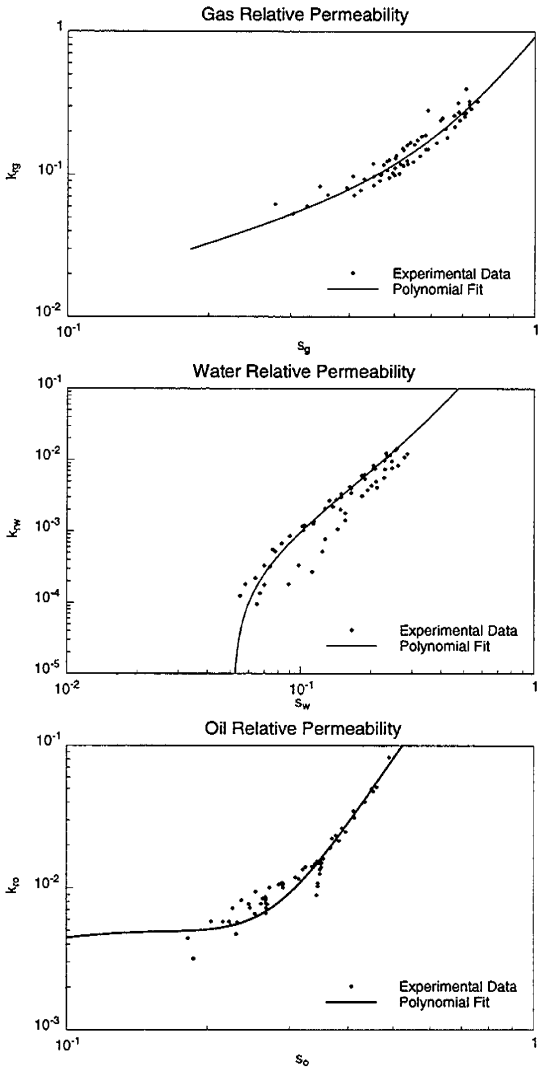

Figure 3.2: Measured and fitted relative permeabilities

Table 3.1: Polynomial fit to relative permeability

k_{rp}	A	B	C	D	E
Oil	0.079	-0.399	0.436	0.878	1.023
Gas	0.160	-0.009	0.091	0.261	0.425
Water	-0.01	0.2	-0.198	1.662	-0.032

using different Corey [75] type relative permeabilities in different regions of the saturation space. The approach we use in this report is simpler, and the polynomial form of relative permeability gives good predictions of the recoveries and saturation paths, as we show later.

We will now summarize the procedure to calculate the analytical solution given by Guzman and Fayers [78, 79]. The dimensionless conservation equation, in one dimension, ignoring capillary pressure may be written as:

$$s_t + A s_x = 0 \tag{3.2}$$

where

$$s = \begin{pmatrix} s_w \\ s_g \end{pmatrix} \tag{3.3}$$

$$s_t = \begin{pmatrix} \frac{\partial s_w}{\partial t} \\ \frac{\partial s_g}{\partial t} \end{pmatrix} \tag{3.4}$$

$$s_x = \begin{pmatrix} \frac{\partial s_w}{\partial x} \\ \frac{\partial s_g}{\partial x} \end{pmatrix} \tag{3.5}$$

and

$$A = \begin{pmatrix} \frac{\partial f_w}{\partial s_w} & \frac{\partial f_w}{\partial s_g} \\ \frac{\partial f_g}{\partial s_w} & \frac{\partial f_g}{\partial s_g} \end{pmatrix} \tag{3.6}$$

s_w is the water saturation, s_g is the gas saturation, and f_w and f_g are fractional flows of water and gas respectively. There are two independent saturations, chosen to be s_w and s_g, and the oil saturation is given by:

$$s_o = 1 - s_w - s_g \tag{3.7}$$

Let $x = 0$ be the injection end of the experiment, then we have the initial conditions at time, $t = 0$: $s_g = 1$ for $x \leq 0$ (we inject gas at 100% saturation) and $s_g = 0$, $s_w = s_{wi}$ for $x > 0$, where s_{wi} is the initial water saturation in the core. This mathematical statement is a Riemann problem that may be solved by the method of characteristics (MOC). The solutions are functions of $v = x/t$ only. Mathematically, we can write Eq. (2) as:

$$v\frac{ds}{dv} = A\frac{ds}{dv} \tag{3.8}$$

where v is an eigenvalue of A, and ds/dv is an eigenvector, and:

$$\frac{ds}{dv} = \begin{pmatrix} \frac{ds_w}{dv} \\ \frac{ds_g}{dv} \end{pmatrix} \tag{3.9}$$

The matrix A has two eigenvalues that correspond to characteristic wavespeeds ($v = x/t$) with which given saturation values will travel.

A rarefaction is a smooth change in saturation with v. The eigenvectors of A tell us the path in saturation space taken by a rarefaction as the wavespeed changes. Fig. 3.3 shows these rarefaction curves computed for the polynomial relative permeabilities fit to Grader and O'Meara's experiments. Only rarefaction curves for the faster of the two wavespeeds are shown. In Appendix A we show how the eigenvalues and eigenvectors are computed, and how the rarefaction curves are found.

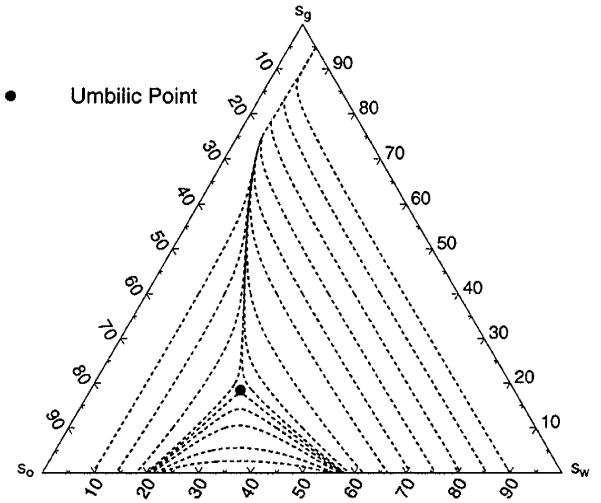

Figure 3.3: Rarefaction curves for the polynomial relative permeabilities fit to Grader and O'Meara's experiments

An analytical solution is constructed by following a rarefaction curve from the injection condition ($s_g = 1$ in this case) to the initial condition as the wavespeed increases monotonically. The reason the wavespeed has to increase is to avoid multiple-valued solutions for $s(v = x/t)$. For most cases this simple procedure is not possible and a solution can only be constructed with shocks or discontinuities in saturation. Shocks obey an integral form of the conservation equation and the shock speed is:

$$V_{sh} = \frac{f_p^L - f_p^R}{s_p^L - s_p^R} \tag{3.10}$$

where L and R label the saturations to the left (upstream) and right (downstream) of the shock respectively, and $p = w,g$. Eq. 10 is obeyed by both water and gas phases. Constant states, where s is constant as v varies, may separate shocks and rarefaction waves. It is possible to construct a unique path from injection to initial conditions as the wavespeed (or shock speed) monotonically increases, composed of rarefactions, shocks and constant states. How these solutions are constructed for the cases presented in this report is described in Appendix A.

If k_{rp} is a function of its own saturation, then A always has real eigenvalues [76]. More complex models that assume at-least one k_{rp} dependent on two saturations (such as Stone's models [68, 69]) yield complex wavespeeds. Regions in saturation space with complex wavespeeds are called elliptic regions.

If the two eignevalues of A are equal at some s_w and s_g then we have an umbilic point, and both wavespeeds are the same. Corey type relative permeabilities give a single umbilic point (Holden [77]) and no elliptic regions. If the relative permeabilities are more general functions of their own phase, Guzman and Fayers [78, 79] showed that there may be none, one or multiple umbilic points, and again no elliptic regions. It is the presence of points of inflexion ($d^2k_{rp}/ds_p^2 = 0$, for $s_p \neq 0$ and $s_p \neq 1$) in any of the relative permeability curves that gives rise to the more complex structure. The relative permeabilities we use here do have points of inflexion. There is a single umbilic point (at $s_w = 0.2879$ and $s_g = 0.184$) in the three phase region and the structure of the rarefaction curve is qualitatively similar to that obtained using Corey type relative permeabilities [80, 81].

Inspection of the rarefacton curves, Fig. 3. gives an indication of the saturation paths. For low oil saturation, the rarefactions are aligned at approximately constant s_o, which means that gas will preferentially displace water, with little displacement of oil. This makes physical sense for horizontal gas injection at low oil saturation where the water relative permeability is much larger than the oil relative permeability. For large oil saturation, the rarefactions have approximately constant s_w. This implies that gas preferentially displaces oil since $k_{ro} > k_{rw}$. Notice that there is a dividing rarefaction [80, 81] that passes through the umbilic point and separates paths with s_o approximately constant from those with s_w approximately constant. This dividing curve has a critical influence on the analytical solutions and its precise location is extremely sensitive to the relative permeabilities. For example, we attempted to fit the experimental data in Fig. 3.2. with a third order polynomial ($D = E = 0$ in Eq. (1)). The fit was excellent, but the predicted analytical solutions were not matched to the experiment as well as for a fifth order polynomial. On the other hand, the solutions are insensitive to the predicted relative permeabilities at saturations below those measured in the experiment, since here the wavespeeds are very low. Thus in Fig. 2. the very steep k_{rw} curve at low s_w and the flat k_{ro} curve at low s_o which are artifacts of the polynomial fit, have very little effect on the solutions. Also note that the rarefactions shown in Fig. 3 appear to start at $s_g = 0.95$, rather than $s_g = 1$. This is because the predicted water relative permeability at low saturation is very small and goes to zero for s_w approximately 5%. This represents a connate water saturation. The important point to stress here is that a good match to experiments is obtained by a good match to the relative permeabilities for the saturations actually measured; the extrapolation of the relative permeabilities outside the region probed experimentally has no physical meaning.

As a check on our analytical solution, we also performed numerical simulations of the three phase flow problems. We used an explicit, first order in time, second order in space, total variation diminishing (TVD) scheme (Blunt and Rubin [45]) with 800 gridblocks.

Fig. 3.4. shows the saturation path for horizontal gas injection into low oil saturation ($s_{wi} = 0.696$, $s_{oi} = 0.304$). Grader and O'Meara [44] do not provide sufficient information to construct the saturation profiles for their experiments, but we can compare directly the measured and predicted saturation paths. This case recovers very little incremental oil. The analytical solution follows the rarefaction curve and then shocks directly to the initial conditions. Except for small v, the rarefaction and shock are at approximately constant oil saturation. Thus the oil recovery is poor unless a huge number of pore volumes of gas is injected.

Fig. 3.5. shows gas injection into a higher oil saturation ($s_{wi} = 0.518$, $s_{oi} = 0.482$). Here it is not possible to find a shock from the rarefaction curve to the initial conditions. The analytic solution features a shock from the three phase region to the two phase region, and then a two phase shock to the initial conditions. This solution has an oil bank. Fig. 6. for $s_{wi} = 0.447$, $s_{oi} = 0.553$,

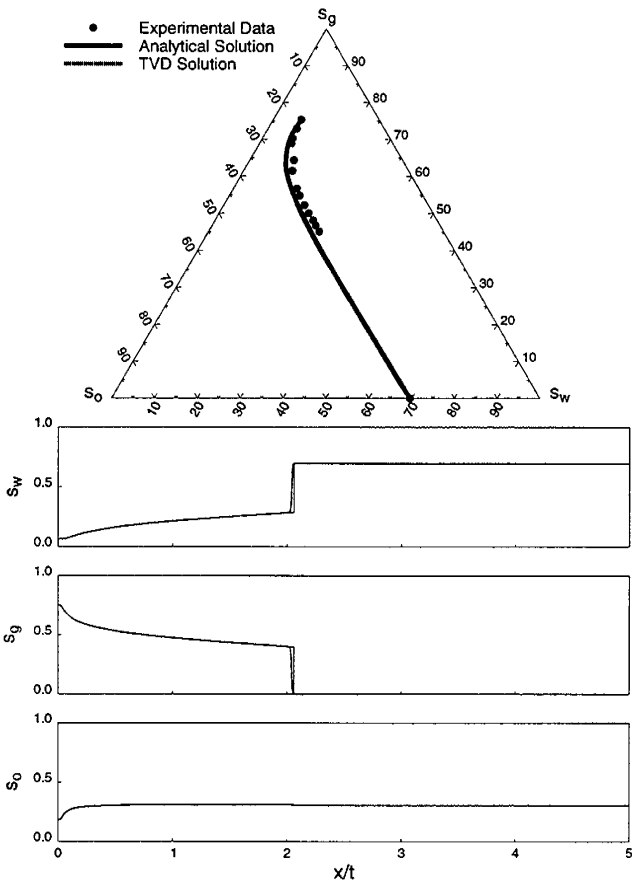

Figure 3.4: Predicted and measured saturation paths for Grader and O'Meara's run #9

shows qualitatively the same features. The analytical solution for the cases shown in Figs. 5 and 6 follow the same path in the three phase region.

For all cases, the analytical and experimental paths are similar. The formation of an oil bank, and a three phase shock has been observed directly using in-situ saturation measurements for similar experiments [56]. Our analytical predictions for runs #15 and #7 are not shown, but they also agree well with the experiments. The numerical and analytical one-dimensional solutions for saturation are virtually identical.

The polynomial relative permeabilities we used assumed that the residual oil saturation was zero. This implies that given sufficient time, gas could displace all the oil and water from the core. In reality, however, the experiments are run for only a finite time. Since the wavespeeds for drainage at low saturations are very slow (corresponding to low relative permeability), it would take huge amounts of gas to displace oil at very low saturations. For the range of saturations actually encountered, the theoretical predictions are excellent. Even if the relative permeabilities predict zero residual oil saturation, this saturation will never be reached in a realistic experiment.

Falls and Schulte [80, 81] presented analytical solutions for three phase flow with Corey type relative permeabilities, for which a single umbilic point was observed. The solutions obtained here are similar to the ones obtained by Falls and Schulte, and there is a narrow range of initial conditions for which the solution follows the same path in the three phase region (Figs. 5 and 6). The use of Stone [68, 69] relative permeabilities or different curves for different regions of saturation space, as suggested by Hicks and Grader [74], give elliptic regions. These are unphysical artifacts

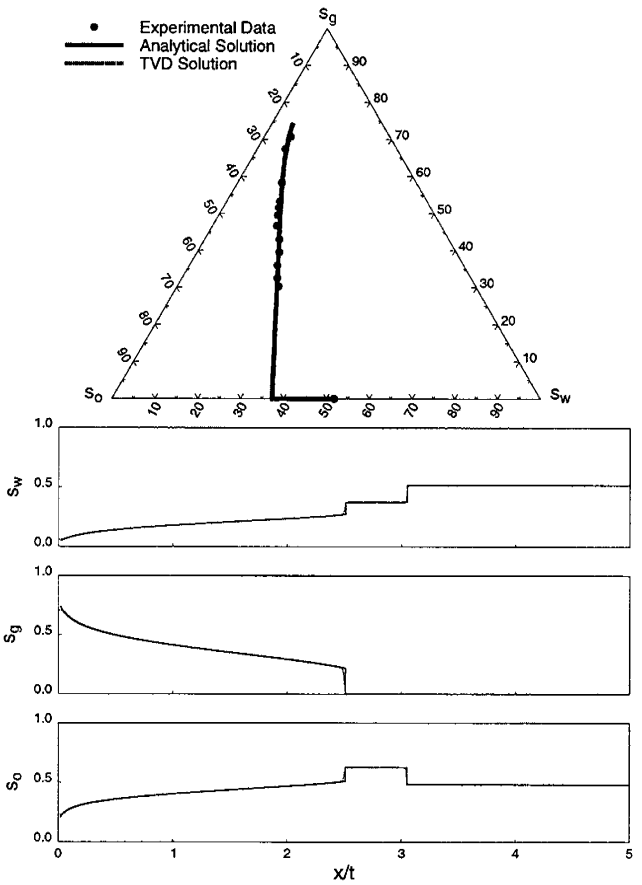

Figure 3.5: Predicted and measured saturation paths for Grader and O'Meara's run #8

of the extrapolation of the relative permeabilities outside the domain probed experimentally. The elliptic regions can cause instabilities or may give rise to non-unique solutions [76]. In this work, the experimental data is matched successfully using polynomial relative permeabilities, and there are no elliptic regions.

Recovery Calculation

Once the saturation profiles have been obtained, the oil recovery can be computed analytically. Fig. 3.7. shows the oil and water recoveries as a function of pore volumes of decane injected for run #5. The computed recoveries match well with the experimental data. As seen in Fig. 3.7. the increase of slope of the recovery curve for oil just before 0.3 pore volumes injected is due to the breakthrough of the oil bank prior to the gas.

Conclusions

For the experiments analyzed the three phase relative permeabilities were, to a good approximation, functions of their own saturation. Analytical solutions for the saturation paths and recoveries computed using a polynomial fit to the relative permeabilities predicted the results of the experiments well. The fitted relative permeabilities did not give elliptic regions and there was a single umbilic point in the three phase region. For a narrow range of initial conditions a two phase shock, and an oil bank developed, and the saturation paths in the three phase region were the

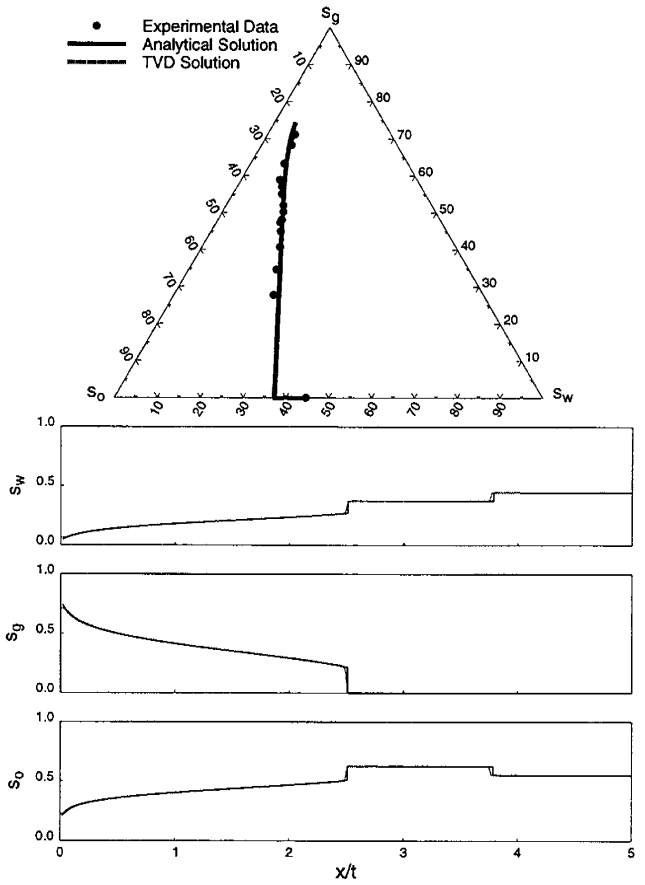

Figure 3.6: Predicted and measured saturation paths for Grader and O'Meara's run #5

same. Outside this narrow range, different initial conditions may lead to different saturation paths through the three phase region. The solution structure is similar to that obtained from Corey type relative permeabilities [80, 81].

3.4 Gravity Drainage Experiments

Introduction

Past research [26, 27, 60, 31] has shown that three phase gravity drainage results in very low residual oil saturations. However, we need to equate oil recovery to some measurable quantity and figure out how long it would take to recover oil by gravity drainage. To understand this, we will be performing three phase gravity drainage experiments under different spreading and initial conditions, with both consolidated (sandstone) and unconsolidated (sand) porous media. To obtain different spreading conditions we will be using three different oils; hexane, n-octane and n-decane. We hope to find out how oil recovery varies with changing spreading coefficient for three phase gravity drainage. Table 3.2. gives a list of proposed experiments. We can calculate relative permeability from in-situ measurements of phase saturations obtained from the CT-scanner and compute the saturation paths and recoveries analytically using the method of characteristics.

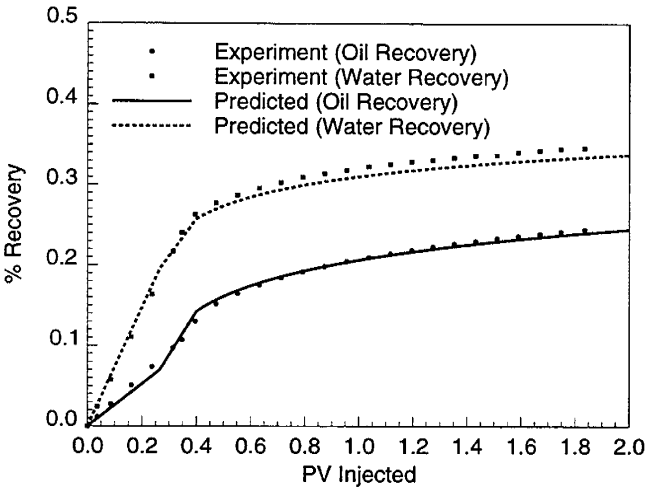

Figure 3.7: Predicted and measured recoveries for Grader and O'Meara's run #5

Table 3.2: Proposed three phase gravity drainage experiments

Exp.No.	*Fluid*	*PorousMedium*	*InitialCondition*
1	n-octane	sand	intermediate s_o
2	hexane	sand	intermediate s_o
3	decane	sand	intermediate s_o
4	n-octane	sand	$s_o + s_{wc}$
5	n-octane	sand	$s_{or} + s_w$
6	n-octane	sandstone	intermediate s_o
7	hexane	sandstone	intermediate s_o
8	decane	sandstone	intermediate s_o

Analysis of of Gravity Drainage Experiments

We develop here the equations needed to compute relative permeability during a two phase air-water gravity drainage experiment. Equations to compute three phase gravity drainage follow from these equations.

Starting with Darcy's law for two phase flow with the z direction defined to be positive in the downward direction.

$$u_w = -\frac{kk_{rw}}{\mu_w}\left(\frac{\partial p_w}{\partial z} - \rho_w g\right) \tag{3.11}$$

$$u_g = -\frac{kk_{rg}}{\mu_g}\left(\frac{\partial p_g}{\partial z} - \rho_g g\right) \tag{3.12}$$

Since head change in the gas phase is almost zero, we have

$$p_g - \rho_g g z = 0 \tag{3.13}$$

or

$$\frac{\partial p_g}{\partial z} = \rho_g g \tag{3.14}$$

Capillary pressures implies

$$p_g - p_w = p_{cgw} \tag{3.15}$$

thus

$$p_w = p_g - p_{cgw} = \rho_g g z - p_{cgw} \tag{3.16}$$

Substituting this in Equation 3.11. we get

$$u_w = \frac{k k_{rw}}{\mu_w} \left(\frac{\partial p_{cgw}}{\partial z} + \Delta \rho_{gw} g \right) \tag{3.17}$$

where

$$\Delta \rho_{gw} = \rho_w - \rho_g \tag{3.18}$$

Conservation of water implies

$$\frac{\partial u_w}{\partial z} + \phi \frac{\partial s_w}{\partial t} = 0 \tag{3.19}$$

Inserting Equation 3.19 in Equation 3.17 we get

$$\phi \frac{\partial s_w}{\partial t} = -\frac{\partial}{\partial z} \left[\frac{k k_{rw}}{\mu_w} \left(\frac{\partial p_{cgw}}{\partial z} + \Delta \rho_{gw} g \right) \right] \tag{3.20}$$

From the above Equation we can obtain relative permeability of water as

$$k_{rw} = -\frac{\mu_w \phi}{k} \frac{\int_0^z \frac{\partial s_w}{\partial t} dz}{\left(\frac{\partial p_{cgw}}{\partial z} + \Delta \rho_{gw} g \right)} \tag{3.21}$$

In the above equation, z is the distance from the top of the core or sandpack. We assume that $s_g = 1.00$ at the top of the core($z = 0$).

In the region where capillary pressure is negligible, the relative permeability is given by

$$k_{rw} = -\frac{\mu_w \phi}{k} \frac{\int_0^z \frac{\partial s_w}{\partial t} dz}{\Delta \rho g} \tag{3.22}$$

Once the relative permeabilities are known we can compute the flow velocity for each phase using the method of characteristics. For free gravity drainage, neglecting capillary pressure Equation 3.17 becomes

$$u_w = \frac{kk_{rw}}{\mu_w}(\rho_w - \rho_g)g \tag{3.23}$$

Using the Method of Characteristics, we can obtain the following from Equations 3.19 and 3.23

$$v_w = \frac{z}{t} = \frac{k(\rho_w - \rho_g)g}{\mu_w \phi}\frac{\partial k_{rw}(s_w)}{\partial s_w} \tag{3.24}$$

where v_w is the characteristic velocity for a given water saturation s_w. Assuming the relative permeability of a phase to be a function of saturation of that phase only (for example: $k_{rw} = as_w^b$) we can write the above equation as

$$v_w = \frac{k(\rho_w - \rho_g)g}{\mu_w \phi} abs_w^{(b-1)} \tag{3.25}$$

Air-Water Gravity Drainage Experiment

In this section, we show results from an air-water gravity drainage experiment where in-situ phase saturations have been obtained from the CT scanner. Meaurements of porosity and saturation as a function of distance(from the top of sandpack) and time are shown in Figure 3.8. Relative permeability is calculated using the expression given in Equation 3.22. The saturation profiles are calculated from the expression given in Equation 3.24, neglecting capillary pressure. Measurements of the relative permeabilities and the computed saturation profiles are shown in Figure 3.9.

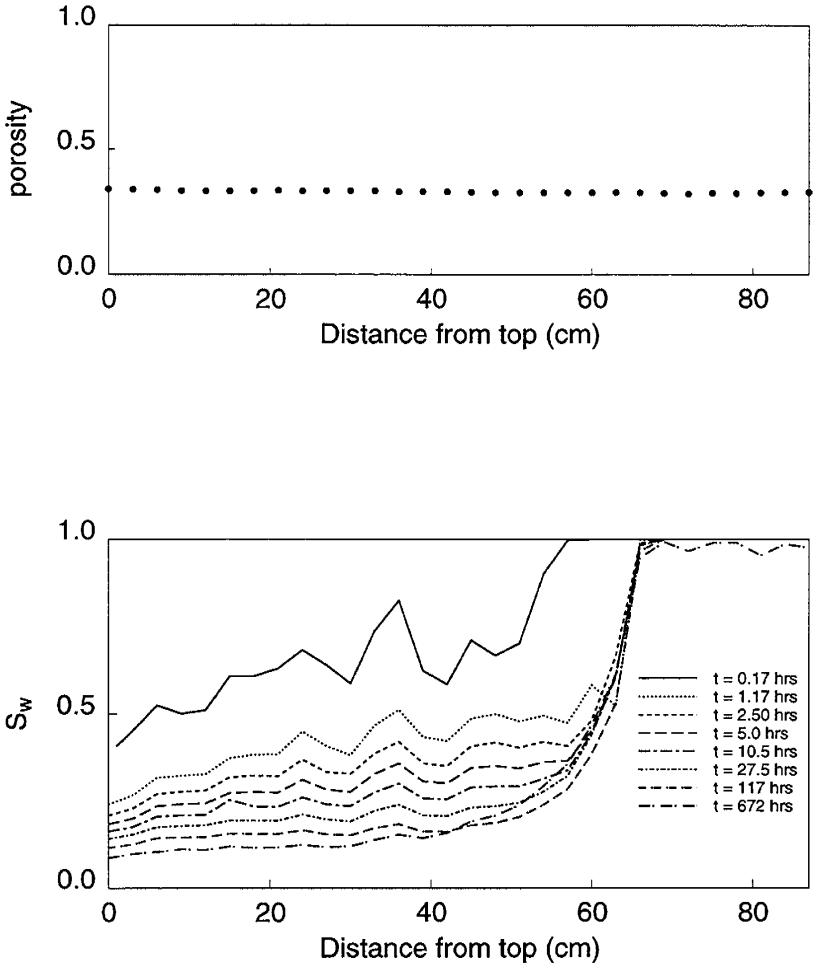

Figure 3.8: Porosity and in-situ saturation measurements from CT Scanner

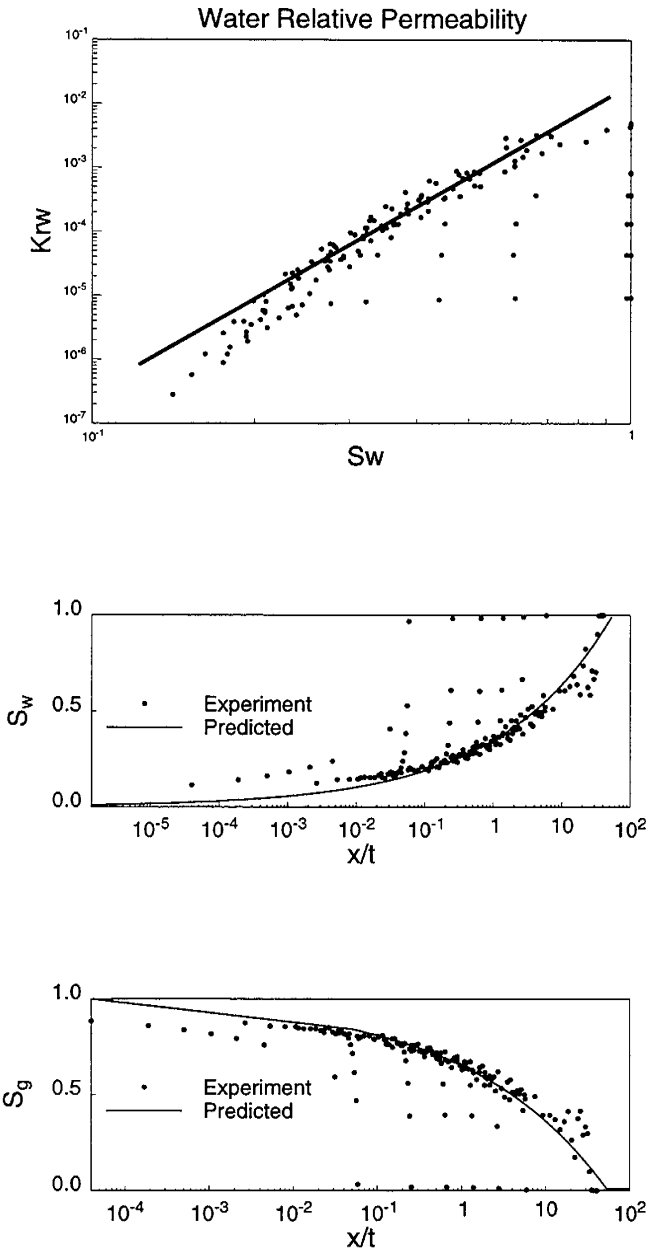

Figure 3.9: Relative permeability and computed saturation profiles

Three Phase Gravity Drainage

The equations to compute relative permeability for three phase gravity drainage follow from those derived earlier for two phase gravity drainage.

For three phase flow we can write Darcy's law for each of the three phases as

$$u_w = -\frac{kk_{rw}}{\mu_w}\left(\frac{\partial p_w}{\partial z} - \rho_w g\right) \tag{3.26}$$

$$u_o = -\frac{kk_{ro}}{\mu_o}\left(\frac{\partial p_o}{\partial z} - \rho_o g\right) \tag{3.27}$$

$$u_g = -\frac{kk_{rg}}{\mu_g}\left(\frac{\partial p_g}{\partial z} - \rho_g g\right) \tag{3.28}$$

We can write the capillary pressure equations as

$$p_g - p_o = p_{cgo} \tag{3.29}$$

$$p_o - p_w = p_{cow} \tag{3.30}$$

Again assuming zero head drop for the gas phase ($p_g = \rho_g g z$),

$$p_o = \rho_g g z - p_{cgo}, \tag{3.31}$$

$$p_w = \rho_g g z - p_{cgo} - p_{cow}, \tag{3.32}$$

and

$$u_o = \frac{kk_{ro}}{\mu_o}\left(\frac{\partial p_{cgo}}{\partial z} + \Delta\rho_{go} g\right) \tag{3.33}$$

$$u_w = \frac{kk_{rw}}{\mu_w}\left(\frac{\partial p_{cow}}{\partial z} + \frac{\partial p_{cgo}}{\partial z} + \Delta\rho_{gw} g\right) \tag{3.34}$$

where

$$\Delta\rho_{go} = \rho_o - \rho_g \tag{3.35}$$

and

$$\Delta\rho_{gw} = \rho_w - \rho_g \tag{3.36}$$

Now conservation of water implies

$$\phi \frac{\partial s_w}{\partial t} + \frac{\partial u_w}{\partial x} = 0 \tag{3.37}$$

Hence

$$u_w|_z = \int_0^z \phi \frac{\partial s_w}{\partial t} dz \tag{3.38}$$

Conservation of oil implies

$$\phi \frac{\partial s_o}{\partial t} + \frac{\partial u_o}{\partial x} = 0 \tag{3.39}$$

Hence

$$u_o|_z = \int_0^z \phi \frac{\partial s_o}{\partial t} dz \tag{3.40}$$

Thus the equations for the water and oil relative permeabilities are

$$k_{ro} = -\frac{\mu_o \phi}{k} \frac{\int_0^z \frac{\partial s_o}{\partial t} dz}{\left(\frac{\partial p_{cgo}}{\partial z} + \Delta \rho_{go} g \right)} \tag{3.41}$$

$$k_{rw} = -\frac{\mu_w \phi}{k} \frac{\int_0^z \frac{\partial s_w}{\partial t} dz}{\left(\frac{\partial p_{cow}}{\partial z} + \frac{\partial p_{cgo}}{\partial z} + \Delta \rho_{gw} g \right)} \tag{3.42}$$

To calculate the relative permeabilities, we need in-situ saturation measurements as a function of distance from the top of the core and time. This can be done using dual-energy CT scanning and the equations to obtain the saturations are derived in Appendix B.

3.5 Conclusions

We have developed a methodology for analyzing three-phase flow experiments. We have described a technique for measuring three-phase relative permeabilities from in-situ CT scan measurements of oil and water saturations. In later work we plan a series of gravity drainage experiments to measure three-phase relative permeabilities with a particular emphasis on low oil and water saturations.

3.6 Nomenclature

A = Jacobian matrix of flux vector f
ds = right eigenvector of matrix A
f = flux vector with components f_w and f_g
f_g, f_w= gas and water fractional flow
k = absolute permeability
k_{rp} = relative permeability to phase p
ν = x-ray attenuation of material
s_p = saturation (p = o, g, w)
s = saturation vector with components s_w and s_g
t = dimensionless time (injected pore volumes)
V_{sh} = shock velocity
v = eigenvalues of matrix A
x = dimensionless distance

Greek Letters
δ = discriminant
ϕ = porosity

Subscripts
1 = first energy level
2 = second energy level
g = gas
o = oil
p = phase
t = derivative with respect to t
w = water
x = derivative with respect to x

Superscripts
L = left state
R = right state

3.7 Appendix A

More details on the construction of analytical solutions to three phase flow are given in References [78] and [79]. The dimensionless conservation Equation 3.2. is:

$$s_t + As_x = 0 \tag{3.43}$$

where A is given by Equation 3.6. The eigenvalues of A are:

$$v = \frac{1}{2}(f_{ww} + f_{gg}) \pm \sqrt{\delta} \tag{3.44}$$

where

$$\delta = (f_{ww} - f_{gg})^2 + 4f_{gw}f_{wg} \tag{3.45}$$

and

$$f_{pq} = \frac{\partial f_p}{\partial s_q} \tag{3.46}$$

The eigenvectors are aligned along the direction

$$ds = \begin{pmatrix} 1 \\ \frac{ds_g}{ds_w} \end{pmatrix} = \begin{pmatrix} 1 \\ \left(f_{gg} - f_{ww} \pm \sqrt{\delta}\right)/2f_{wg} \end{pmatrix} \tag{3.47}$$

and thus the ratio of a change in s_g to s_w along an eigenvector is:

$$ds_g = \left(\left(f_{gg} - f_{ww} \pm \sqrt{\delta}\right)/2f_{wg}\right) ds_w \tag{3.48}$$

A rarefaction curve is found by starting at some given $s = (s_w,\ s_g)$ and using Equation 3.48. to find the change in s_g for a small change in s_w. Then Equation 3.48. is recomputed and the new eigenvalues are found. In this way a curve in $(s_w,\ s_g)$ space is traced. In Figure 3.3, the faster rarefaction is found, i.e., the positive root in Equation 3.48. is taken.

To construct the analytical solutions we start at the initial condition and attempt to find a shock into the three phase region, where

$$v(s_p^L) = V_{sh} = \frac{f_p^L - f_p^R}{s_p^L - s_p^R} \tag{3.49}$$

for $p = w,\ g$. $s_p^R = s_{pi}$, i.e. the initial condition and we try to find s_p^L that obeys these conditions. Equation 3.49 represents two independent equations for two unknowns (s_w^L, s_g^L). Once s_w^L and s_g^L are known we follow a rarefaction curve back to the injection conditions. Note that Equation 3.49. describes a Buckley-Leverett type shock, where the shock speed is equal to the wavespeed of the left state.

For Figures 3.5 and 3.6. we could not find a shock from the initial conditions to the three phase region. For three phase flow with a unique umbilic point, the three phase shock jumps from the two phase region to the dividing rarefaction that passes through the umbilic point [80, 81]. We have three unknowns, s_w^L, s_g^L and s_w^R, the water saturation in the two phase region. Equation 3.49 gives two indepedent equations. Insisting that s_w^L and s_g^L lie on the rarefaction that passes through the umbilic point gives the third equation. To aid in the solution of these equations we can use the numerical solution as an initial guess for s_w^R. There is then a two phase shock to the initial conditions. This shock speed must be larger than for the three phase shock.

3.8 Appendix B

The equations for three phase saturation calculations using dual energy CT scanning are derived in the following section. For each energy level, the CT number of a core containing three fluids is given by the equations

$$CT_1 = (1-\phi)\nu_{r1} + \phi s_g \nu_{g1} + \phi s_o \nu_{o1} + \phi s_w \nu_{w1} \tag{3.50}$$

$$CT_2 = (1-\phi)\nu_{r2} + \phi s_g \nu_{g2} + \phi s_o \nu_{o2} + \phi s_w \nu_{w2} \tag{3.51}$$

Also

$$s_g = 1 - s_o - s_w \tag{3.52}$$

This gives us three equations with three unknowns.
Setting

$$CT_{gr1} = (1 - \phi)\nu_{r1} + \phi\nu_{g1} \tag{3.53}$$

and

$$CT_{gr2} = (1 - \phi)\nu_{r2} + \phi\nu_{g2} \tag{3.54}$$

gives

$$s_o = \frac{[CT_1 - CT_{gr1}](\phi\nu_{w2} - \phi\nu_{g2}) - [CT_2 - CT_{gr2}](\phi\nu_{w1} - \phi\nu_{g1})}{(\phi\nu_{o1} - \phi\nu_{g1})(\phi\nu_{w2} - \phi\nu_{g2}) - (\phi\nu_{o2} - \phi\nu_{g2})(\phi\nu_{w1} - \phi\nu_{g1})} \tag{3.55}$$

$$s_w = \frac{[CT_2 - CT_{gr2}](\phi\nu_{o1} - \phi\nu_{g1}) - [CT_1 - CT_{gr1}](\phi\nu_{o2} - \phi\nu_{g2})}{(\phi\nu_{o1} - \phi\nu_{g1})(\phi\nu_{w2} - \phi\nu_{g2}) - (\phi\nu_{o2} - \phi\nu_{g2})(\phi\nu_{w1} - \phi\nu_{g1})} \tag{3.56}$$

4. Analytical Calculation of Minimum Miscibility Pressure

Yun Wang and Franklin M. Orr, Jr.

Analysis of the problem of one-dimensional, dispersion-free displacement of a multicomponent oil by a gas such as CO_2, or methane has shown that the behavior of the flow is controlled by a sequence of key tie lines. Those that extend through the original oil and injected gas compositions and $n_c - 3$ tie lines known as crossover tie lines. The minimum miscibility pressure (MMP) is the lowest pressure at which any of the key tie lines is a critical tie line. We show how to identify the $n_c - 3$ crossover tie lines for oils that contain an arbitrary number of components as a sequence of tie lines whose extensions intersect. For displacement by a gas that contains only one component, that problem is equivalent to the problem of performing a flash calculation for single phase mixture with the composition of the intersection point. We transform the standard flash equation to a form that gives convergent solutions even for compositions well outside the phase diagram. We use the modified flash calculation to determine which of the key tie lines approaches the critical locus as the pressure is increased. Calculation of tie line lengths for a sequence of increasing pressures to determine the MMP as the lowest pressure at which the length of one of the key tie-lines becomes zero. Extension of the method to systems with two components in the injection gas is demonstrated for a four-component system, and further extension to multicomponent injection gases is discussed.

4.1 Introduction

Gas injection processes are among the most effective methods of enhanced oil recovery. A key parameter in the designing of a gas injection project is the minimum miscibility pressure (MMP), the pressure at which the local displacement efficiency approaches 100% . If the flow is one-dimensional (1D) and there is no dispersive mixing, then the displacement efficiency is exactly 100% at the MMP. In real displacements, however, those conditions are not strictly satisfied. At pressures near MMP, the phases that form in the transition zone between injected fluid and original oil in place have very low interfacial tension, and the displacement is close to piston-like even when small amounts of dispersion or nonuniform flow due to viscous fingering or gravity segregation are present. That is the situation that arises in slim tube displacements, for example, displacement experiments that are routinely used to determine the MMP. In those experiments a long (say 10 m or longer), small diameter (say 0.5 cm) tube packed with sand or glass beads is filled with oil that is then displaced by injection gas at a fixed temperature and outlet pressure. The fraction of the original oil in place recovered after injection of some fixed amount of gas (usually 1.1 or 1.2 pore volumes) is measured. The fraction of oil recovered is then plotted as a function of pressure. Typically, recovery increases rapidly with increasing pressure and then levels off. The MMP is usually taken to be the intersection of lines drawn through recovery points in the steeply climbing and level regions as long as the recovery in the level region is above some arbitrary cutoff (often 90%).

Most attempts to predict MMPs have been empirical. Investigators have tried to fit experimental MMPs to a variety of expressions for specific gas systems (see, for example, Holm and Josendal [82]; Glaso [83]; Orr and Silva [84]). While those approaches reproduce reasonably well the experimental observations on which they were based, they should be used with caution for injection gases or oils with compositions substantially different from those used to build the correlation (Orr and Silva [84]).

Computational attempts to calculate the MMP include three approaches: One-dimensional compositional simulations, mixing cell calculations based on a single cell, and multiple mixing cell calculations. Compositional simulations can be used to determine the MMP provided that sufficiently fine grids are used in the computations, the prediction of the MMP will be as accurate as the representation of the phase behavior by the equation of state used. The disadvantage of the simulation approach is the lengthy computation time for fine-grid simulations performed at many pressures.

Other investigators have used mixing cell methods (Pedersen *et al.* [87]; Jensen and Michelsen [88]; Neau *et al.* [89]) to estimate MMPs. In those methods, injected gas is first mixed with oil and flashed. The resulting vapor is mixed with fresh oil (forward contacts) and the liquid is mixed with fresh injection gas (reverse contacts), and the new mixtures are flashed. The process is repeated until it converges. The forward contacts converge to the tie line that extends through the oil composition (if there is one), and the reverse contacts converge to the tie line through the injection gas composition. The pressure is then increased until one of the tie lines is a critical tie line, which is taken to be the MMP. These methods work well as long as it is oil tie line (vaporiaing gas drive) or the injection gas tie line (condensing gas drive) that controls miscibility. In many systems, however, the MMP occurs at a pressure at which neither the oil tie line nor the gas tie line is a critical tie line, though such behavior can only occur if four or more components are present (Orr *et al.* [90]). The condensing/vaporizing drive described by Zick [86] and Stalkup [85] is an example of this behavior (Johns *et al.* [91]). For those systems, mixing cell methods do not give accurate predictions.

Multicell versions of the mixing cell idea have also been used. Metcalfe *et al.* [92] described a technique in which gas is added to the first cell and the contacts are flashed. The resulting gas phase is then moved to the next cell while more gas is added to the initial cell, and both cells are flashed. Again gas is moved to downstream cells. Thus, the procedure is similar to one-dimensional simulation, though fluids are not moved according to relative permeability functions. Hearn and Whitson [93] cite unpublished work by Zick that shows that multicell methods can be used for condensing-vaporizing drives.

In this report, we attempt to avoid the inaccuracies that can arise from finite grids or numbers of mixing cells, as well as the computational effort of many flash calculations in many cells, by calculating the MMP directly from analytical solutions for multicomponent, two-phase flow. We define the MMP based on the assumption of 1D, dispersion-free flow. Under those assumptions, the MMP can be calculated rigorously from analytical solutions for one-dimensional flow obtained by the method of characteristics (MOC). We begin with a brief review of the MOC theory to show that the problem of finding the MMP can be reduced in many cases to the problem of finding a sequence of tie lines whose extensions intersect at compositions that may lie well outside the region of physically attainable compositions. Next we formulate and solve a negative flash algorithm that converges for the compositions of the intersection points and use it to determine the sequence of tie lines. We then adjust the displacement pressure until one of the key tie lines becomes a critical tie line, one that is tangent to the critical locus (Johns and Orr [94]). We describe a technique that can be used to find the MMP for a two-component injection gas, and we discuss the extension of the technique to systems with more components.

4.2 Mathematical Model

For one-dimensional, dispersion-free two-phase flow in which components do not change volume as they transfer between two phases, the mass conservation equations are

$$\frac{\partial C_i}{\partial t} + \frac{\partial F_i}{\partial z} = 0, \qquad i = 1, ..., n_c, \tag{4.1}$$

where t and z are dimensionless time and distance, respectively. Components do change volume as they transfer between phases, but that volume change does not affect the MMP (Dindoruk [95]). C_i is the overall volumetric fraction of component i given by:

$$C_i = c_{il}[1 + (K_i - 1)S], \quad i = 1, ..., n_c, \tag{4.2}$$

F_i is the the overall fractional flux of component i given by:

$$F_i = c_{il}[1 + (K_i - 1)f], \quad i = 1, ..., n_c, \tag{4.3}$$

Here c_{il} is the volume fraction of component i in the liquid phase; S is gas saturation; f is the fractional flow of the gas phase; and K_i is the equilibrium ratio of component i.

For the calculations reported here, the fractional flow function was assumed to be

$$f = \frac{S^2}{S^2 + (1 - S)^2}. \tag{4.4}$$

It should be noted that while the fractional flow function is required to construct analytical solutions to Eq. 4.1, numerical calculations suggest that it has no effect on the key tie line geometry that determines the MMP. Two additional constraints associated with Eq. 4.1 are:

$$\sum_{i=1}^{n_c} C_i = 1, \tag{4.5}$$

and

$$\sum_{i=1}^{n_c} F_i = 1, \tag{4.6}$$

which means that only $n_c - 1$ of the conservation equations are independent.

Eqs. 4.1-4.6 can be solved by calculating the velocity at which a given overall composition propagates. An eigenvalue problem results, in which an eigenvalue is the wave speed at which the composition moves. The associated eigenvector gives a discrete direction in composition space along which composition variations satisfy the differential equations. Integration along eigenvector directions gives many 'paths' through the n_c dimensional composition space. For example, Fig. 4.1 shows typical composition paths for a four-component system in which equilibrium K-values are independent of composition (Note that when equilibrium K-values are independent of compositions the surfaces of liquid and vapor compositions are both planes. In Fig. 4.1, the surface of liquid compositions is the triangle ABC, and the surface of vapor compositions is DEF). Tie lines are paths, and there are two nontie-line paths through each composition point. The solution to the problem is the unique route that connects the initial oil composition to the injection gas composition (Monroe *et al.* [96]). The modern form of the theory was developed for analysis of three-component surfactant flooding (Larson and Hirasaki [97]; Larson [98]; Helffreich [99]; Hirasaki [100]), though mathematically equivalent approaches were reported earlier by Welge *et al.* [101] and Wachman [102] for gas/oil and alcohol displacement systems. Application of the theory to gas/oil systems continued with the analysis of three-component systems by Dumore *et al.* [103]. Monroe *et al.* [96] obtained the first solutions for systems with four components, and subsequent work by Johns [104] and Dindoruk [95] explored the behavior of systems with four or more components (Dindoruk [105]; Orr *et al.* [90]; Johns *et al.* [91]; Johansen *et al.* [106]). Those papers showed that the solution behavior is controlled by $n_c - 1$ key equilibrium tie lines. They are the tie lines that extend through injection gas and initial oil compositions as well as $n_c - 3$ additional tie-lines known as 'crossover' tie lines (Monroe *et al.* [96]). If the pressure or enrichment is increased enough that one of the key tie lines becomes a critical tie line (a tie line of zero length that is tangent to the critical locus),

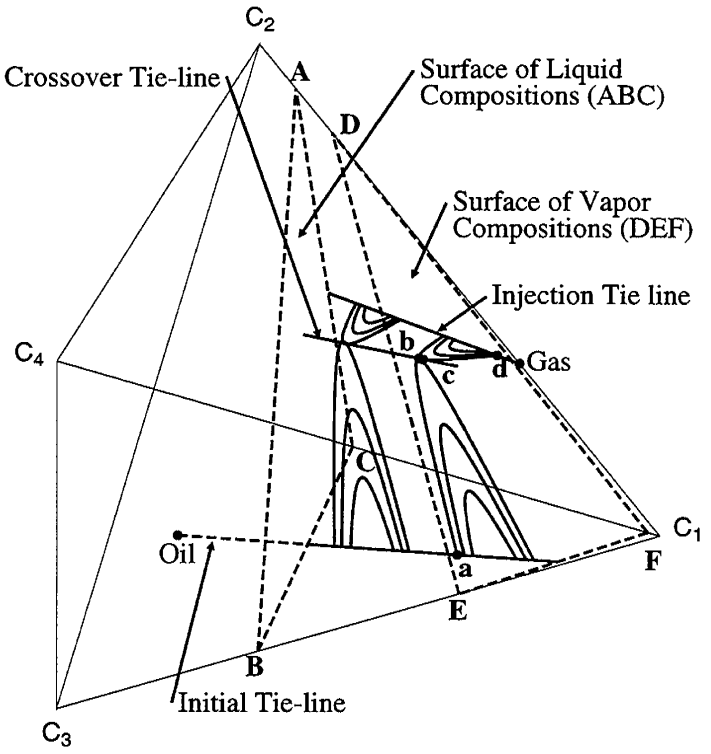

Figure 4.1: Composition paths in a four-component system with constant K-values (Points **a**, **b**, **c**, **d** refer to composition points in Fig. 4.2.

then the displacement is multicontact miscible (Orr *et al.* [90]; Johns *et al.* [91]). Thus the first step toward finding the MMP is to identify the key tie lines.

In portions of the solution where compositions vary continuously, the variation must occur along paths. It often happens, however, that eigenvalues vary along a path in such a way that fast-moving compositions would appear upstream of slow-moving ones, a physical impossibility. In such situations, the continuous variation (known as a rarefaction by analogy with gas dynamics) is replaced by a shock, which must satisfy a material balance (also known as a Rankine-Hugoniot condition) of the form

$$\Lambda = \frac{F_i^U - F_i^D}{C_i^U - C_i^D}, \qquad i = 1, ..., n_c, \tag{4.7}$$

where Λ is the shock velocity, superscripts U and D represent the upstream and downstream sides of the shock. A shock must also occur whenever the number of phases present changes; the solution route must enter and exit the two-phase region via a shock along a tie line extension (Helfferich [99]).

Fig. 4.2 shows an example, again for the constant K-values, in which a shock between two tie lines would be required. It shows the magnitudes of composition velocities, λ_{nt}, along the path traced from a to b in the 'vertical' surface of paths and then from c to d in the 'horizontal' surface of paths in Fig.1 (between b and c there is a short variation along the crossover tie line). Value of λ_{nt} decreases as the path is traced toward the direction from a to b, so a rarefaction is permitted there. From c to d, however, the value of λ_{nt} increases, which would violate the velocity constraints if this path were being traced in the upstream direction. Hence, this composition variation would be 'self-sharpening', and a shock would connect the tie lines that contain points c and d. An important

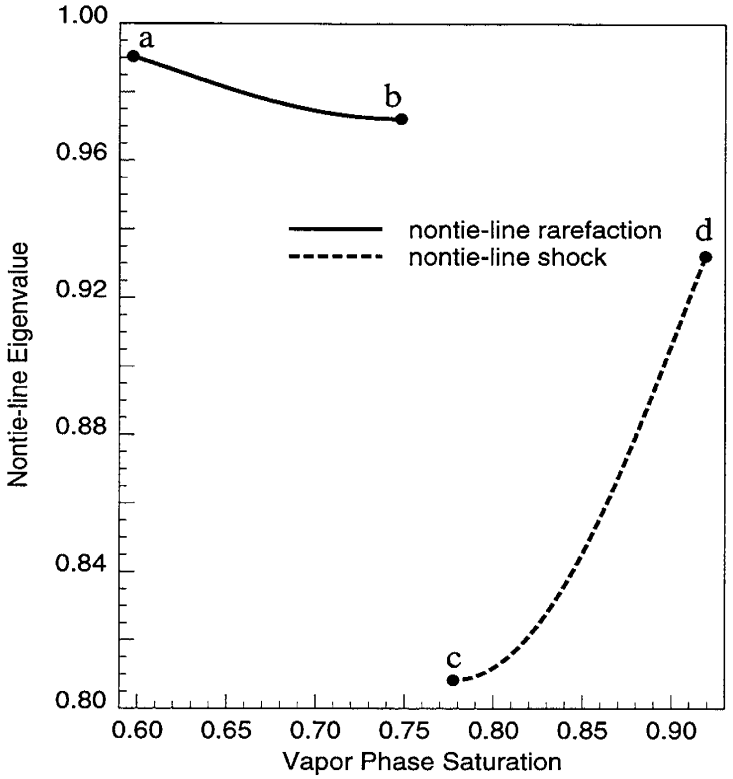

Figure 4.2: Variation of the nontie-line eigenvalue alonf the nontie-line path.

result of the analytical theory is that the extensions of two tie lines connected by a shock must intersect (Johns [104]; Orr *et al.* [90]; Johns *et al.* [91]).

For systems in which all the tie lines are connected by shocks, which we refer to as fully self-sharpening, all the crossover tie lines can be determined from the requirement that the tie line extensions intersect. Fig. 4.3 shows such a system. In Fig. 4.3, the initial oil composition is o, a mixture of methane (CH_4), butane (C_4) and decane (C_{10}). The curves labeled 'phase envelopes' in Fig. 4.3, are the binodal curves of liquid and vapor compositions in the four ternary faces that bound the quaternary diagram. The injection gas is a mixture of CO_2 and CH_4 (composition g). The initial tie line lies in the $CH_4/C_4/C_{10}$ ternary face, and the injection gas tie line is on the $CH_4/CO_2/C_{10}$ face. The extensions of the crossover tie line intersect both the initial oil and injection gas tie lines. In this system, if the pressure were increased, the crossover tie line would become tangent to the critical locus at a pressure lower than that of either the initial oil or injection gas tie lines.

For ternary systems, self-sharpening behavior can be identified easily from an analysis of systems with constant K-values (see Appendix A of Johns [104] or Johns *et al.* [91] for details). The analysis shows that self-sharpening behavior is controlled by whether the value of the intermediate K-value is greater than or less than one. While that analysis is only approximate for systems with composition-dependent K-values, the prediction of self-sharpening behavior is quite reliable. For systems with more than three components, self-sharpening behavior can always be detected by direct integration along nontie-line paths. An approximate method for identifying self-sharpening behavior in multicomponent displacements was outlined by Johns and Orr [94], who reported a procedure for calculation of the MMP for displacement of a multicomponent oil by a single-component gas. In that scheme, components present at any point in a displacement are lumped into a pseudoternary system so that the expression given by Johns and Orr [94] could be used to determine self-sharpening behavior.

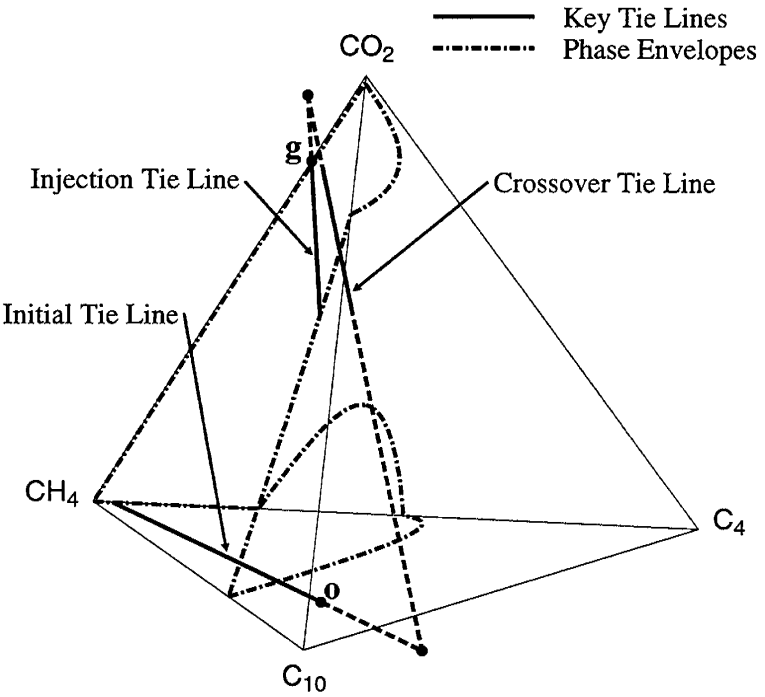

Figure 4.3: Key tie lines for a displacement of a three-component oil (composition **o**) by a two-component gas (composition **g**) at 160° F (71.1° C), 1600 psia (11.0 MPa). The crossover tie line intersects extensions of the initial oil and injection gas tie lines. See Table 4.3 for oil and gas compositions.

In the remainder of this report we develop a technique for calculation of MMP that is rigorous for systems that are fully self-sharpening. Experience with solutions for CO_2 displacements, for example, indicates that the fully self-sharpening systems are common for CO_2 injection. We also have computational evidence that this approach gives accurate MMPs for displacements that include one or more segments of rarefaction along nontie-line paths, but we do not have a rigorous proof of accuracy for those systems.

We find the key tie-lines by solving a sequence of flash calculations for the compositions at intersection points of tie lines. Those points always lie in the single-phase region, and they often fall outside the phase diagram where some component fractions are negative (see Fig. 4.3 for an example). For single-phase compositions that are not too far from the two-phase region, the negative flash of Whitson and Michelsen [107] can be used to determine the tie-line that extends through that composition. However, many of the intersection points that arise in the analytical solutions are well outside the domain of convergence of the negative flash algorithm of Whitson and Michelsen. In the next section, we transform the flash calculation and develop a negative flash algorithm that does converge for such compositions.

4.3 Modified Negative Flash

The equation of any tie line is given by a material balance of the form

$$C_i = c_{il}(1 - S) + c_{iv}S, i = 1, ..., n_c, \tag{4.8}$$

which can be rearranged to yield Eq. 4.2 by substitution of the definition of the equilibrium K-values,

$$K_i = \frac{c_{iv}}{c_{il}}, i = 1, ..., n_c, \tag{4.9}$$

where C_i is the overall composition for component i, c_{il} is the volume fraction of component i in the liquid phase and c_{iv} is the volume fraction in the vapor phase. S is the vapor phase saturation. K_i is the equilibrium ratio for component i (K-value). The equilibrium compositions must also sum to unity,

$$\sum_{i=1}^{n_c} c_{il} = \sum_{i=1}^{n_c} c_{iv} = 1. \tag{4.10}$$

The usual approach to a flash calculation follows that of Rachford and Rice [108]. For a given set of K-values, the following equation is solved iteratively for S,

$$F(S) = \sum_{i=1}^{n_c} \frac{C_i(K_i - 1)}{1 + (K_i - 1)S} = 0. \tag{4.11}$$

The phase compositions are then calculated as

$$\begin{cases} c_{il} = \dfrac{C_i}{1 + (K_i - 1)S} \\ c_{iv} = \dfrac{K_i C_i}{1 + (K_i - 1)S} \end{cases} \tag{4.12}$$

Fugacities can be calculated from an equation of state (EOS). Here we use the Peng-Robinson EOS [109] to calculate component partial fugacities. K-values are then updated using

fugacities until convergence is reached. Phase compositions in mole fractions are converted to volume fractions using the pure component molar densities.

Rachford and Rice assumed that the overall composition is inside the two-phase region. Whitson and Michelsen [107] pointed out that single-phase compositions can be flashed with the same algorithm if the vapor phase saturation is not restricted to lie between zero and one. They showed that their negative flash always converges for compositions within a range bounded by $1/(1-K_{max})$ and $1/(1-K_{min})$, where K_{max} and K_{min} are the highest and lowest K-values of the system.

We observe that, for an arbitrary overall composition, the vapor phase saturation S can vary in an unrestricted way, while the phase compositions c_{il} and c_{iv} are always subject to the restriction that they be greater than zero and less than one. Hence we choose phase compositions instead of vapor phase saturation as the primary variables. Elimination of S yields the following system of equations:

$$\begin{cases} \sum_{i=1}^{n_c} c_{il} - 1 = 0 \\ C_i c_{1l}(K_1 - 1) - c_{1l}c_{il}(K_1 - K_i) - c_{il}C_1(K_i - 1) = 0, \quad i = 2, .., N_c \end{cases} \tag{4.13}$$

Eq. 4.13 can be solved for the liquid phase compositions by a Newton-Raphson iteration of the form

$$\mathbf{J}\Delta\mathbf{c_l} = -\mathbf{F}, \tag{4.14}$$

where Δc_l is the vector of changes in individual component fractions. The entries in F are

$$F_1 = \sum_{i=1}^{n_c} c_{il} - 1 \tag{4.15}$$

$$F_i = C_i c_{1l}(K_1 - 1) - c_{1l}c_{il}(K_1 - K_i) - c_{il}C_1(K_i - 1) \quad i = 2, .., n_c. \tag{4.16}$$

The Jacobian matrix $\mathbf{J}$, whose elements are derivatives of $\mathbf{F}$ with respect to c_{il}, is

$$\mathbf{J} = \begin{bmatrix} 1 & 1 & 1 & ... & 1 \\ J_{21} & J_{22} & 0 & ... & 0 \\ J_{31} & 0 & J_{33} & ... & 0 \\ . & . & . & . & . \\ J_{n_c 1} & 0 & 0 & ... & J_{n_c n_c} \end{bmatrix} \tag{4.17}$$

where

$$\begin{cases} J_{i1} = C_i(K_1 - 1) - c_{il}(K_1 - K_i) \\ J_{ii} = -c_{1l}(K_1 - K_i) - C_1(K_i - 1) \qquad i = 2, .., n_c \end{cases} \tag{4.18}$$

The simple structure of the Jacobian matrix yields a straightforward algebraic solution of the form

$$\begin{cases} \Delta c_{1l} = \dfrac{\sum_{i=2}^{n_c} \dfrac{F_i}{J_{ii}} - F_1}{1 - \sum_{i=2}^{n_c} \dfrac{J_{i1}}{J_{ii}}} \\ \\ \Delta c_{il} = -\dfrac{F_i + J_{i1}\Delta c_{1l}}{J_{ii}} \quad i = 2, .., n_c \end{cases} \tag{4.19}$$

The updated phase compositions are

$$c_{il}^{new} = c_{il}^{old} + \Delta c_{il} \quad i = 1, .., n_c. \tag{4.20}$$

The iterative process ends when the left hand side of Eq. 4.13 is zero to within some tolerance. Then the phase compositions are used to calculate new partial fugacities and the K-values are updated. Here we use the standard successive substitution

$$K_i^{new} = K_i^{old}(\frac{f_i^L}{f_i^V}) \quad i = 1, .., n_c, \tag{4.21}$$

where f_i^L and f_i^V are the liquid and vapor partial fugacities for component i, respectively, and the K-values in Eq. 4.20 are defined in terms of mole fractions. The flash calculation is complete when component partial fugacities are equal (to within some tolerance). We note that there is an opportunity to improve the speed of the calculations performed be acceleration along the lines described by Michelsen [110]. For the examples reported in this report, however, the computation times for calculating MMPs were quite short (on the order of 3-10 minutes on a workstation), so the speed of the successive substitution was not a limiting factor.

Fig. 4.4 shows three overall compositions used to test the performance of the modified negative flash, and Fig. 4.5 compares convergence behavior of the modified flash with that of the negative flash of Whitson and Michelsen. Composition **A** is in the domain of convergence of the Whitson-Michelsen negative flash (The vapor phase saturation for point **A** is -0.19799, well within the domain of convergence -1.79176 < S < 1.01865). Both methods converge quickly. Compositions **B** and **C** are outside the domain of convergence for the Whitson-Michelsen negative flash, but Fig. 4.5 shows that the modified negative flash converges quickly for those compositions as well. Points **B** and **C** are actually outside the phase diagram; the mole fraction of CO_2 is negative. They are typical of intersection points (see Fig. 4.3). For point **B**, the vapor phase saturation is -2.48537, which is clearly outside the convergence domain -2.14178 < S < 1.03103. Composition C lies on the extension of a tie line that is quite close to the critical point. The vapor phase saturation of point **C** is -3902.968, which is also outside the domain of convergence defined by the largest and smallest K-values: -3443.336 < S < 323.810 (K_{max} = 1.000290, K_{min} = 0.996912). In this case as well, the modified negative flash converges rapidly. It is important that the flash algorithm perform well in the near-critical region if it is to be used to calculate the MMP.

4.4 Analytical Calculation of MMP

4.4.1 Pure CO_2 Injection

To illustrate how the modified negative flash can be used to determine the MMP, we consider first an example in which pure CO_2 displaces a six-component oil. This system is fully self-sharpening: all the nontie-line portions of the solution are shocks. Hence, all the adjacent key tie lines intersect. We now show that the intersection points are such that exactly one component

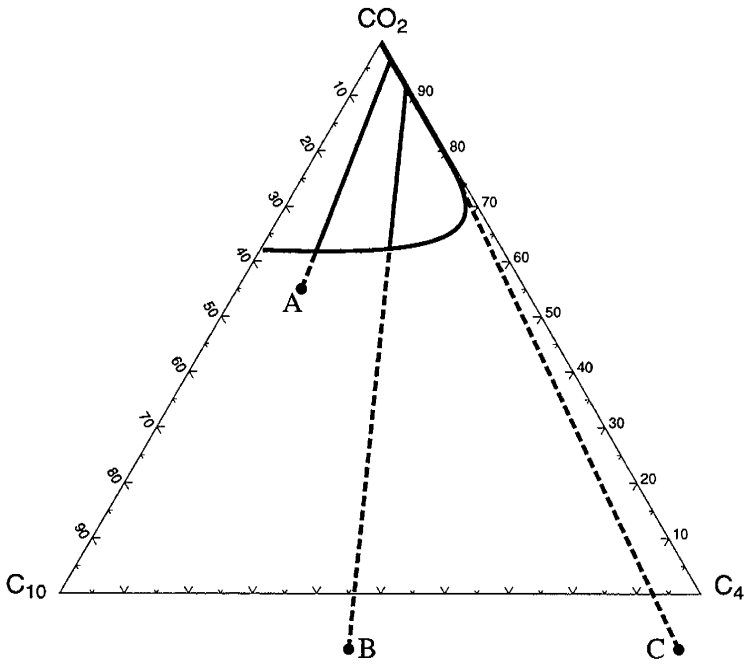

Figure 4.4: Compositioon for test of the modified negative flash algorithm (T = 160° F (71.1° C), P = 1600 psia (11.0 MPa)).

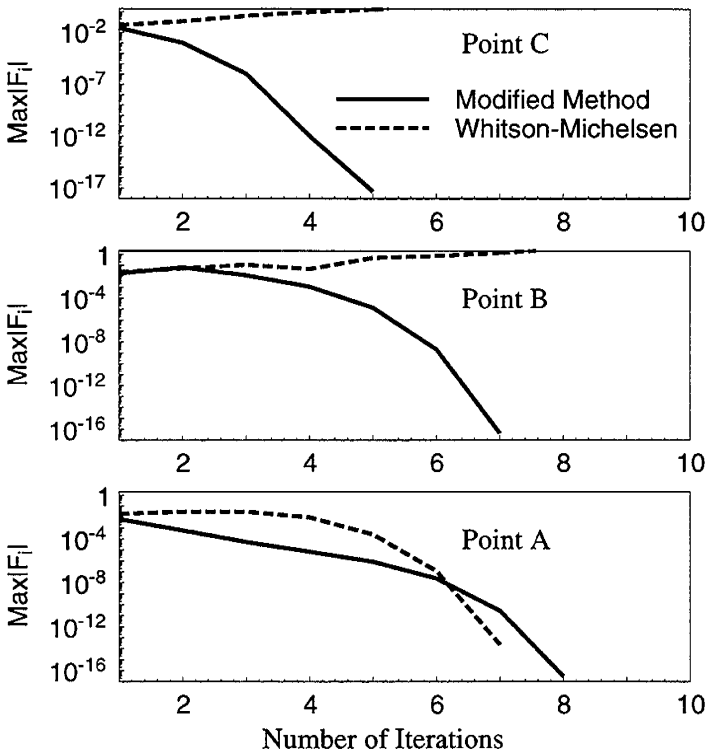

Figure 4.5: Convergence of the modified negative flash.

Table 4.1: Oil and gas compositions for pure CO_2 injection, T=160°F.

Component	Compositions(Mole Fraction)					
	CH_4	CO_2	C_4	C_{10}	C_{14}	C_{20}
Oil	0.20	0.05	0.05	0.40	0.10	0.20
Gas	0.00	1.00	0.00	0.00	0.00	0.00

changes to zero composition across each shock that connects two tie lines. Foe the calculations reported, component properties were those reported by Johns [104].

Table 4.1 shows the oil and gas compositions and system temperature. The initial and injection tie lines are both known. The initial tie line includes all six components that are present in the oil. The injection tie line contains two components, CO_2 and C_{20}. There are three crossover tie-lines altogether for a six-component system.

We show now that one component disappears across each shock between tie lines in the sequence from the initial tie line to the injection tie line. Assume first that there are two intersecting tie lines that have non-zero fractions of an identical number of components. Now the number of components present can only change if the tie line changes. Because there are only three crossover tie lines, there must be another pair of adjacent intersecting tie lines that have two or more components missing. Suppose that components j and k are missing on tie-line n, then

$$C_j = c_{jl}^n[1 + (K_j^n - 1)S_n] = 0, \tag{4.22}$$

$$C_k = c_{kl}^n[1 + (K_k^n - 1)S_n] = 0, \tag{4.23}$$

which requires that

$$S_n = \frac{1}{1 - K_j^n} = \frac{1}{1 - K_k^n} \tag{4.24}$$

Eq. 4.24 is satisfied only if $K_j^n = K_k^n$, an equality that never holds true except at the critical point as long as K-values stay ordered. That condition is satisfied for this system and for systems of practical interest; if two components have almost equal K-values they should be lumped for compositional purposes. Thus, the assumption that two tie lines in the sequence have the same number of components leads to a contradiction. Hence we have shown that, for this system, there are four shocks that connect pairs of tie lines, and one component present in the initial oil disappears across each shock. The argument given applies to initial compositions with an arbitrary number of components. Therefore the statement applies for displacement of an oil containing any number of components by a pure component gas.

We use the disappearance of one component at each shock to locate easily the sequence of tie line intersection points. Components disappear in the order of their K-values: CH_4 first in the shock from the initial tie line to crossover tie line 1; C_4 second in the shock from crossover tie line 1 to crossover tie line 2, and so on. Table 4.2 shows the sequence of tie lines for the example six-component oil displaced by CO_2. For the disappearing component on the crossover tie line n,

$$C_j = c_{jl}^n[1 + (K_j^n - 1)S^n] = 0. \tag{4.25}$$

Table 4.2: Key tie-line structure for pure CO_2 injection.

Tie-lines	Compositions					
	CH_4	CO_2	C_4	C_{10}	C_{14}	C_{20}
Initial	√		√	√	√	√
Crossover 1		√	√	√	√	√
Crossover 2		√		√	√	√
Crossover 3		√			√	√
Injection		√				√

Therefore the vapor phase saturation on crossover tie line n where the component j is zero is

$$S^n = \frac{1}{1 - K_j^n}. \tag{4.26}$$

Substitution of Eq. 4.24 into Eq. 4.23 for other components gives the i compositions of the intersection point,

$$C_i = c_{il}^n \Big[\frac{K_i^n - K_j^n}{1 - K_j^n}\Big], \qquad i \neq j. \tag{4.27}$$

Application of the modified negative flash then gives the next tie line associated with the intersection point.

The lengths l_n of the key tie-lines indicate how close they are to the critical region,

$$l_n = \sqrt{\sum_{i=1}^{n_c} (c_{iv}^n - c_{il}^n)^2} \tag{4.28}$$

To find the MMP, we repeat the calculation of tie line lengths for increasing pressures. The MMP is the pressure at which one of the key tie lines reaches zero length, an indication that it is a critical tie line. Thus, for a pure component injection gas, the algorithm for calculation of the MMP is:

1. Perform a modified negative flash to find the initial oil and injection gas tie lines.
2. Find the intersection point between the initial tie line and crossover tie line 1 from Eq. 4.27 applied to each of the components in the oil,

$$C_i^1 = c_{il}^o \Big[\frac{K_i^o - K_j^o}{1 - K_j^o}\Big], \tag{4.29}$$

where superscript o denotes the initial tie line, and

$$i = CH_4, CO_2, C_4, C_{10}, C_{14}, C_{20}, \quad j = CH_4. \tag{4.30}$$

3. Perform a modified negative flash to find crossover tie line 1.
4. Find the intersection point between crossover tie lines 1 and 2

$$C_i^2 = c_{il}^1 \Big[\frac{K_i^1 - K_j^1}{1 - K_j^1}\Big], \tag{4.31}$$

where the superscript 1 denotes crossover tie line 1, and

$$i = \mathrm{CH_4}, \mathrm{CO_2}, \mathrm{C_4}, \mathrm{C_{10}}, \mathrm{C_{14}}, \mathrm{C_{20}}, \quad j = \mathrm{C_4}. \tag{4.32}$$

5. Perform a modified negative flash to find crossover tie line 2.

6. Find the intersection point between crossover tie lines 2 and 3

$$C_i^3 = c_{il}^2 \Big[\frac{K_i^2 - K_j^2}{1 - K_j^2} \Big], \tag{4.33}$$

where the superscript 2 denotes crossover tie line 2, and

$$i = \mathrm{CH_4}, \mathrm{CO_2}, \mathrm{C_4}, \mathrm{C_{10}}, \mathrm{C_{14}}, \mathrm{C_{20}}, \quad j = \mathrm{C_{10}}. \tag{4.34}$$

7. Perform a modified negative flash to find the crossover tie line 3.

8. Increase system pressure and repeat the above steps until one of the key tie line lengths is zero.

Fig. 4.6 shows the change of key tie line lengths with pressure. As Fig. 4.6 indicates, the first crossover tie line reaches the critical region at lower pressure than any other tie line. Therefore it is the first crossover tie line that controls miscibility. Fig. 4.6 indicates that the MMP is 2380 psia (16.4 MPa). To confirm the MMP calculated analytically, we also carried out one-dimensional compositional simulations for the same system. We used a fully explicit finite difference simulator with single-point upstream weighting. The Peng-Robinson equation of state was used to calculate phase equilibria. The computations were performed with 800 grid blocks, and the Courant number ($C = \lambda \Delta t / \Delta x$, λ is the eigenvalue) was set to 0.2. Fig. 4.7 shows results of those simulations reported as fractional recovery (defined as one minus the fraction of moles of hydrocarbons remaining within the porous medium) of hydrocarbon components at 1.1 pore volumes injected (the use of recovery at 1.1 pore volumes injected is arbitrary but customary in interpretations of slim tube displacements). We interpret the compositional simulation results as if they were experimental results: The estimated MMP is taken to be the intersection of lines drawn through recovery points in the steeply climbing and level regions. An estimated MMP of 2340 psia (16.1 MPa) is obtained by extrapolating the linear portions of the recovery curve to an intersection point. A more precise estimate of the MMP could have been obtained by applying the technique described by Zick [86](extrapolation to an infinite number of grid blocks), though at the cost of some additional computation time. While the numerical results are clearly influenced by numerical dispersion (see Stalkup [85], Zick [86] or Walsh and Orr [111]), they are already accurate enough to confirm the analytical results.

Next we consider displacement of a ten-component oil by pure CO_2. This oil was studied experimentally by Metcalfe and Yarborough [112], and Johns and Orr [94] reported an analytical solution for this oil. However, they encountered convergence difficulties in the near critical region when they attempted to calculate the MMP, and hence they obtained only an estimate. However, use of the modified negative flash described here allowed direct calculation of the MMP. Fig. 4.8 shows the key tie line lengths as a function of system pressure, obtained by the algorithm described. Again the first crossover tie line controls miscibility. For displacement of oils containing dissolved CH_4, CO_2 will normally have the second highest K-value, and hence the first crossover tie line will control miscibility (Johns and Orr [94]). The calculated MMP is 1466 psia (10.1 MPa). Again, the numerical results (see Fig. 4.7) confirm the analytical MMP with an estimate of 1460 psia (10.1 MPa).

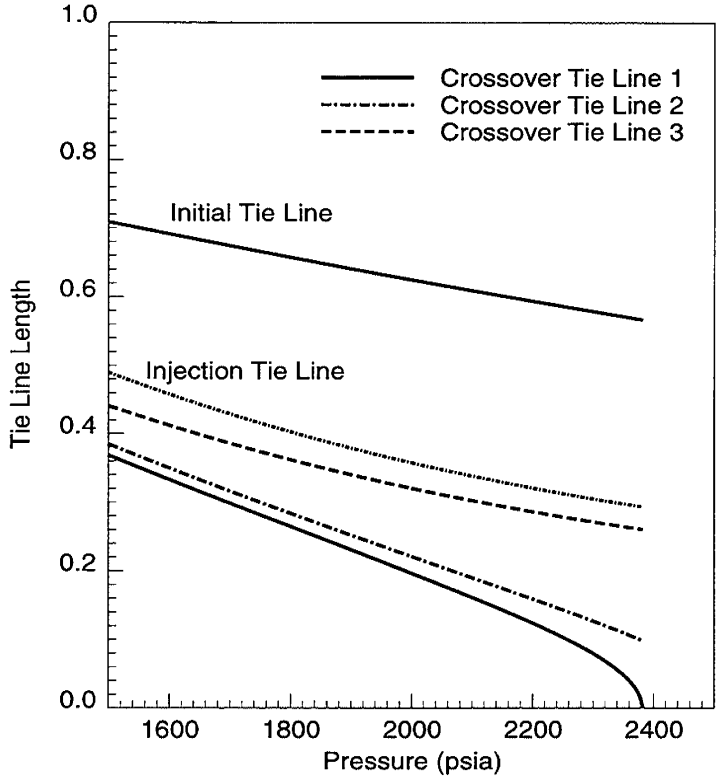

Figure 4.6: Dependence of key tie line lengths on pressure for displacement of a six-component oil by CO_2 at 160° F (71.1° C). The MMP is 2380 psia (16.4 MPa). See Table 4.1 for oil and gas compositions.

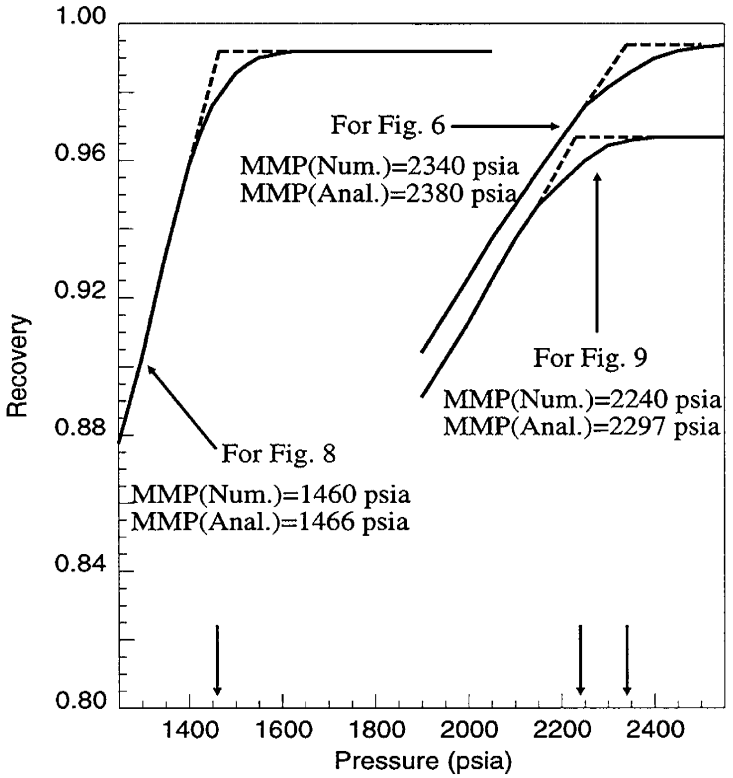

Figure 4.7: Results of one-dimensional compositional simulations with 800 grid blocks and a Courant number of 0.2, for the systems of Fig. 4.6, Fig. 4.8 and Fig. 4.9.

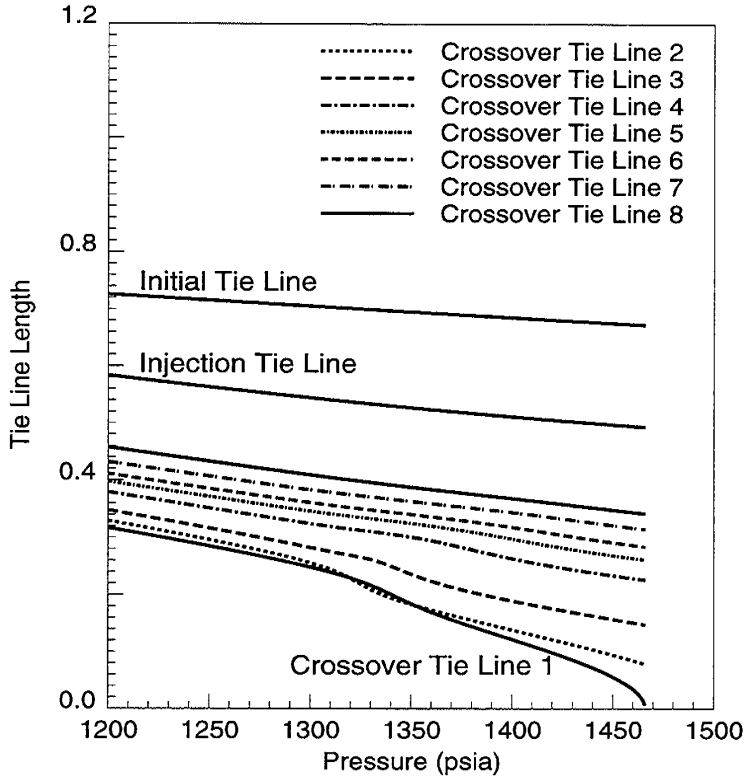

Figure 4.8: Key tie line lengths for CO_2 displacement of a ten-component oil at 120° F (48.9° C). The MMP is 1466 psia (10.1 MPa).

The algorithm given can be applied to a fully self-sharpening system with any number of components as long as the injection gas contains only a single component. This approach is more difficult to apply, however, if the injection gas contains more than one component. In the next section, we consider an alternative approach for such injection gas systems.

4.4.2 Two-Component Gas Injection

If the injection gas contains more than one component, then it is not necessarily true that a component disappears at each shock that connects two tie lines. Furthermore, the tie line intersection points associated with shock solutions cannot be determined *a priori* by using the fact that one component disappears at the intersection points. The example shown in Fig. 4.3 is such a system. Table 4.3 lists the oil and gas compositions as well as the system temperature. In this example, the injection gas contains CO_2 and CH_4, and the crossover tie line intersects both the initial and injection tie lines. However, the intersection points cannot be determined unless the crossover tie line is known. In principle, the technique for single-component gas injection could be used to determine the key tie lines if guesses of intersection points were made. However, experience indicates that the trial and error approach is difficult to apply in a way that converges routinely, especially when the system contains more than four components.

In such cases, therefore, it is more convenient to solve the full set of intersection equations simultaneously. In this four-component example, the equations for the two intersection points of the key tie lines are

$$c^o_{\mathrm{CH_4},\mathrm{I}}[1 + (K^o_{\mathrm{CH_4}} - 1)S^o] = c^c_{\mathrm{CH_4},\mathrm{I}}\Big[\frac{K^c_{\mathrm{CH_4}} - K^c_{\mathrm{CO_2}}}{1 - K^c_{\mathrm{CO_2}}}\Big], \tag{4.35}$$

Table 4.3: Oil and gas compositions for a four-component system, T=160°F.

Component	Compositions(Mole Fraction)			
	CH_4	CO_2	C_4	C_{10}
Oil	0.20	0.00	0.15	0.65
Gas	0.20	0.80	0.00	0.00

$$c^o_{C_4,l}[1 + (K^o_{C_4} - 1)S^o] = c^c_{C_4,l}\Big[\frac{K^c_{C_4} - K^c_{CO_2}}{1 - K^c_{CO_2}}\Big], \tag{4.36}$$

$$c^g_{CH_4,l}[1 + (K^g_{CH_4} - 1)S^g] = c^c_{CH_4,l}\Big[\frac{K^c_{CH_4} - K^c_{C_4}}{1 - K^c_{C_4}}\Big], \tag{4.37}$$

$$c^g_{CO_2,l}[1 + (K^g_{CO_2} - 1)S^g] = c^c_{CO_2,l}\Big[\frac{K^c_{CO_2} - K^c_{C_4}}{1 - K^c_{C_4}}\Big], \tag{4.38}$$

where $c^o_{i,l}$ are the liquid phase compositions of the initial tie line; $c^g_{i,l}$ are the liquid phase compositions of the injection gas tie line and $c^c_{i,l}$ are the liquid phase compositions of the crossover tie line; K^o_i are the K-values for the initial tie line; K^g_i are the K-values for the injection tie line and K^c_i are the K-values for the crossover tie line (i = CH_4, CO_2, C_4, C_{10}). S^o is the vapor phase saturation on the initial oil tie line of the intersection point between the initial tie line and the crossover tie line, and S^g is the vapor phase saturation on the injection gas tie line of the intersection point between the crossover tie line and the injection tie line.

The initial oil and injection gas tie lines can be found easily from the initial and injection compositions using the negative flash of Whitson and Michelsen [107] or the modified negative flash described here. The K-values of the crossover tie line are not known initially, but the equation of Wilson [113] or some other suitable guess can be used. For the example given here the equation of Wilson was used. Iteration over the K-values converged rapidly for the four-component example, and as the pressures were increased toward the MMP, the solution still converged fairly rapidly. Fig. 4.9 shows the tie line length as a function of the system pressure. It indicates that for this system the MMP is 2297 psia (15.8 MPa), and the crossover tie line controls miscibility. The numerical simulation results shown in Fig. 4.7 confirm the analytical calculation with an estimated MMP of 2240 psia (15.4 MPa).

Fig. 4.10 shows that the effect of adding CH_4 to CO_2 is to increase the MMP substantially. When pure CO_2 is injected, the crossover tie line lies in the $CO_2/C_4/C_{10}$ face, and the MMP is easy to identify (Orr *et al.* [90]). As the CH_4 fraction is increased the MMP climbs because the crossover tie line moves into the interior of the quaternary diagram, where the tie line is further from the critical locus at some pressure below the MMP. Hence, the pressure required to make the crossover tie line a critical tie line increases. When the CH_4 fraction reaches 100% in the injection gas, the algorithm simply finds the critical tie line for the $CH_4/C_4/C_{10}$ ternary system.

4.4.3 Multicomponent Gas Injection

The technique used to handle the two-component gas injection can be extended to systems in which the oil and gas contains more components. In such systems, solutions of the set of tie line intersections should yield the appropriate tie lines provided that the systems are fully self-sharpening. Tie line lengths can then be calculated at a sequence of pressures to find the MMP.

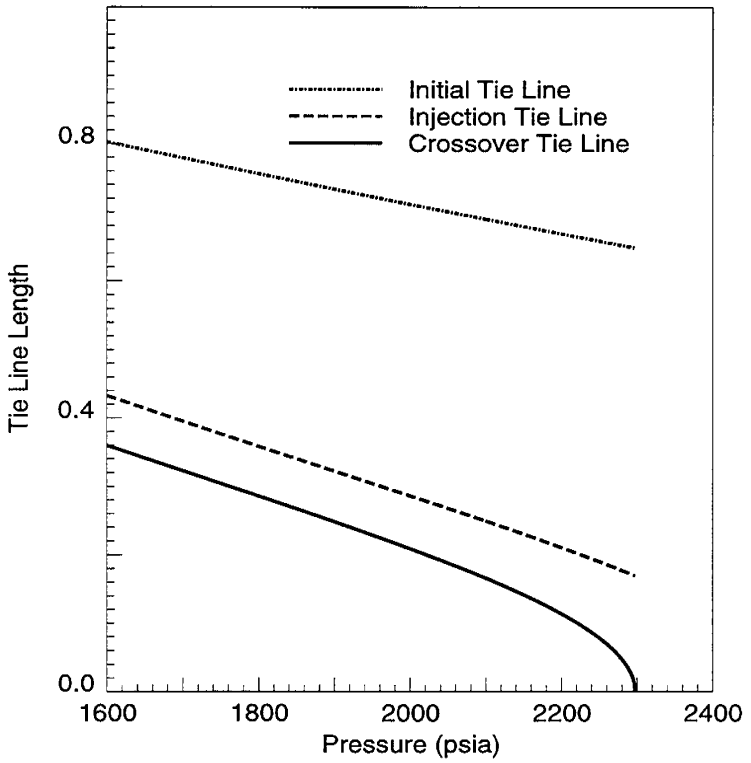

Figure 4.9: Key tie line lengths for a two-component gas displacement of a three-component oil at 160° F (71.1° C), (see Fig. 4.3). The MMP is 2297 psia (15.9 MPa).

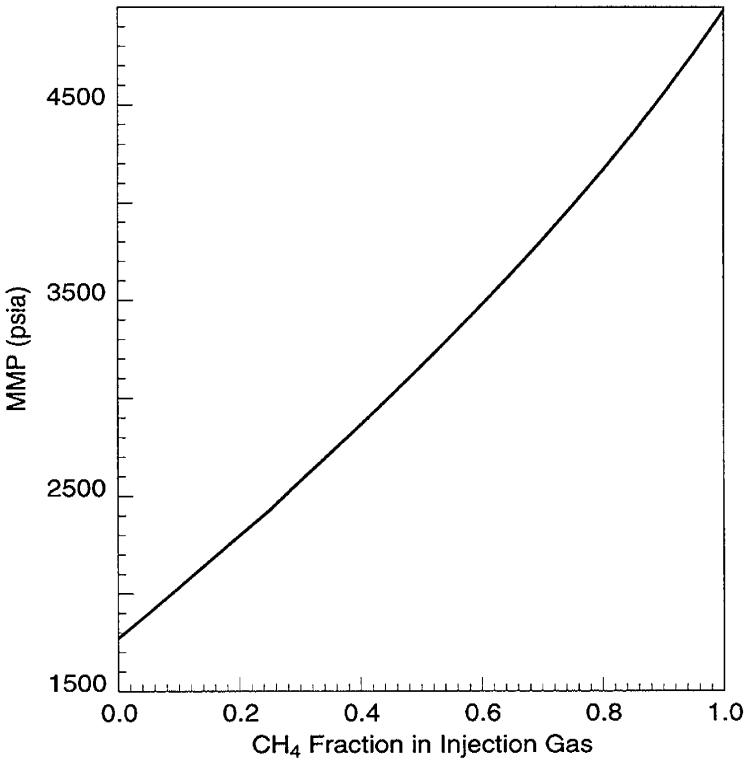

Figure 4.10: Effect of CH_4 contamination of CO_2 on MMP for the displacement of a $CH_4/C_4/C_{10}$ mixture at 160° F (71.1° C). See Table 4.3 for the oil composition and Fig. 4.3 for the phase diagram.

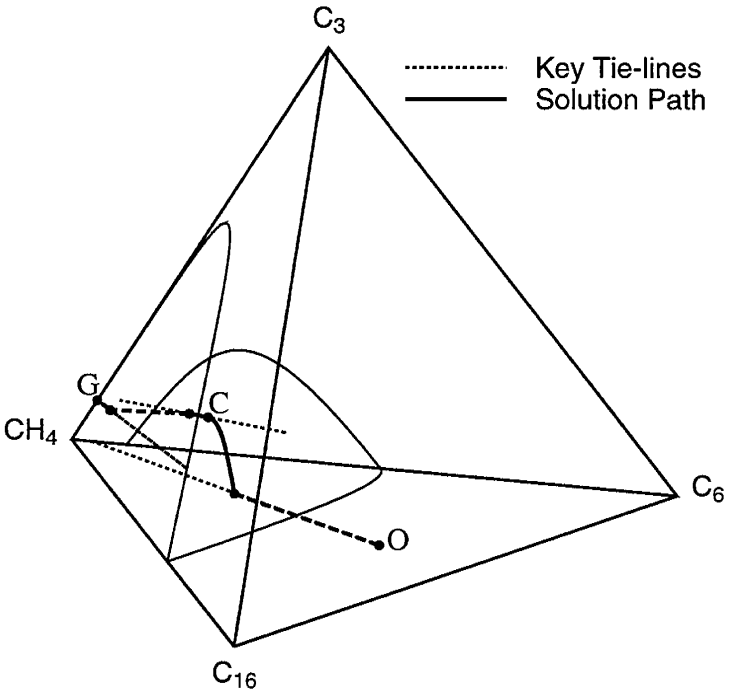

Figure 4.11: Displacement of 20% CH_4, 40% C_6 and 40% C_{16} by 90% CH_4 and 10% C_3 at P = 2000 psia and T = 200° F. There is a rarefaction between crossover tie line C and initial tie line O.

Convergence behavior has not yet been investigated, however, for systems with more than two components in the injection gas and four components in the oil.

At least one additional issue must be addressed if analytical methods are to be used reliably to calculate MMPs for the full range of gas-oil system. While fully self-sharpening systems are quite common, it is possible to find exceptions. If the injection gas contains significant quantities of components with K-values less than one, then it is possible that some tie lines will be connected by rarefactions, and it is also possible to have rarefactions in other situations (see Johns *et al.* [91], for an example). The following example shows that even though tie lines are connected by rarefactions, the notion that all tie lines intersect each other is still a good approximation. If that is generally true then the MMP calculation method proposed in this report will still give accurate predictions of MMPs.

Fig. 4.11 shows a quaternary system in which a CH_4/C_3 mixture displaces a $CH_4/C_6/C_{16}$ mixture. Direct application of the K-value rule suggested by Johns ([104]) indicates that there is a rarefaction along the nontie-line path connecting the crossover tie line and the initial tie line. To show that the notion of intersecting tie lines is still reasonable in this case, we first find the crossover tie line by solving the tie line intersection equations. Next we construct the analytical solution by integrating along the nontie-line path from the crossover tie line to the initial tie line. The numerical integration is quite simple. It consists of taking a small step along the nontie-line eigenvector direction, after which the eigenvector is evaluated again, and the process is repeated. When the composition steps taken are small, the numerical error associated with this simple integration is also small. In the calculations described here, the integration step size was 10^{-6}. Finally, we compare our analytical solution with a solution obtained by fine-grid numerical simulation. To minimize the effect of numerical dispersion, we use a single-point upstream weighting scheme with 5000 grid blocks. Fig. 4.12 shows that the agreement between the analytical and numerical solutions is excellent.

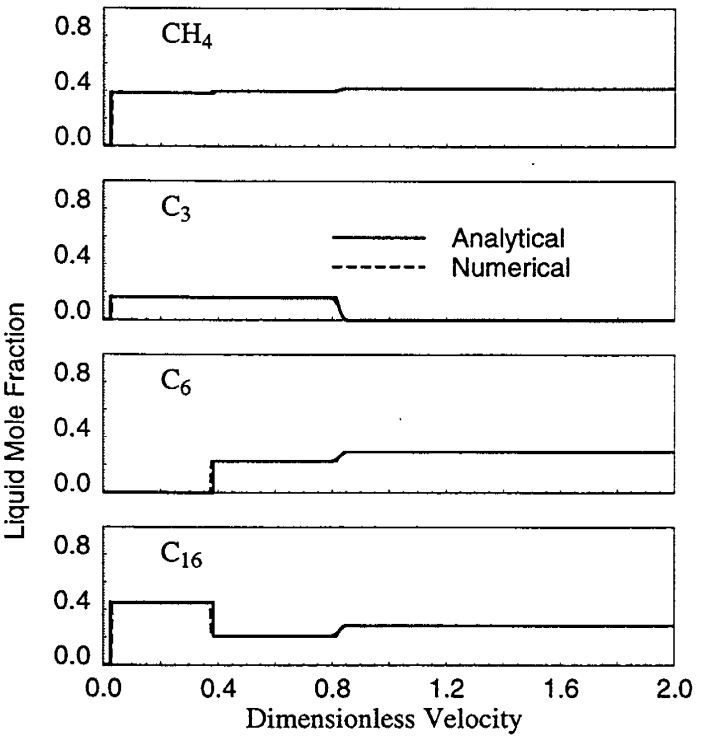

Figure 4.12: Numerical and analytical solutions for a system with a rarefaction along a nontie-line path.

Tables 4.4 and 4.5 compare two key tie lines obtained by three different approaches: analytical solution (Johns [104]), tie line intersection solution and numerical simulation. Table 4.4 compares crossover tie line. The analytical solution was found by integrating along a nontie-line path from the initial tie line to the crossover tie line. The numerical simulation version was obtained by conventional, fine-grid (5000 grid blocks), finite difference simulation. The tie line intersection version agrees quite closely (the maximum difference between tie lines is 4×10^{-5} in the C_6 liquid mole fraction). Table 4.5 compares initial oil tie lines obtained in a i different way. The analytical solution was obtained from a negative flash of the oil composition. The numerical version came from the compositional simulation. The tie line intersection result was obtained by integrating along the nontie-line path from the crossover tie line (calculated with the intersection equations) to the $C_3 = 0$ face. Here again, the maximum difference in phase compositions is about 3×10^{-5} (C_6 mole fraction in the liquid). That difference is small enough to be consistent with the accuracy of the numerical integration along the nontie-line path (step size 10^{-6}). Thus, we conclude that it is reasonable to use the tie line intersection method to estimate the MMP even in the absence of a proof that tie lines intersect when nontie-line rarefactions are present. For the particular system shown in Fig. 4.11, we use the tie line intersection method to calculate the MMP. Fig. 4.13 shows the MMP is 4264 psia (29.4 MPa). Numerical simulation results similar to those shown in Fig. 4.7 gave an estimate of 4320 psia (29.8 MPa) for the MMP. In this example, therefore, the estimate of the MMP from tie line intersection approach is accurate.

Computation times for MMP calculations described here are compared in Table 4.6. Estimation of the MMP by compositional simulation requires that simulations be performed at multiple pressures (we used 10 pressures for the examples in Fig. 4.7). For the relatively simple systems considered here, the tie line intersection approach is about two orders of magnitude faster than

Table 4.4: Tie-line structure for two-component injection.

Tie-lines	Compositions					
	CH_4	CO_2	C_4	C_{10}	C_{14}	C_{20}
Initial	√		√	√	√	√
Crossover 1	√	√	√	√	√	√
Crossover 2	√	√		√	√	√
Crossover 3	√	√			√	√
Injection	√	√				√

Table 4.5: Comparison of the initial tie lines obtained from three different approaches for the system shown in Fig. 4.11.

Initial Tie Line	Liquid Phase Mole Fraction			
	CH_4	C_3	C_6	C_{16}
Analytical	0.420225	0.000000	0.294695	0.285080
Numerical	0.420260	0.000000	0.294660	0.285080
Tie Line Intersection	0.420224	0.000000	0.294674	0.285102
	Vapor Phase Mole Fraction			
Analytical	0.965949	0.000000	0.033674	0.000377
Numerical	0.965943	0.000000	0.033679	0.000378
Tie Line Intersection	0.965952	0.000000	0.033671	0.000377

Table 4.6: Comparison of CPU times between the numerical and analytical approaches.

Figure	System			
	Fig. 9	Fig. 13	Fig. 6	Fig. 8
Number of Components	4	4	6	11
Number of Pressures	10	10	10	10
Method	CPU Time			
Numerical Simulation	11.2 hrs	10.4 hrs	19.1 hrs	32.1 hrs
Analytical Approach	1.3 mins	2.8 mins	2.0 mins	3.5 mins

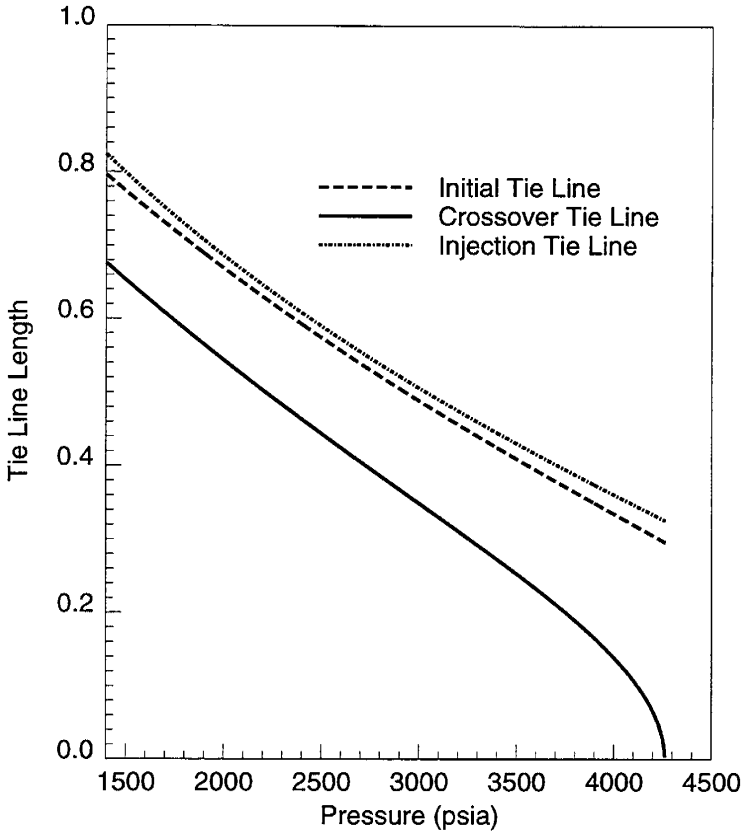

Figure 4.13: Displacement of 20% CH_4, 40% C_6 and 40% C_{16} by 90% CH_4 and 10% C_3 at T = 200° F. MMP = 4264 psia (29.4 MPa).

conventional simulation. For systems with more components present, the compositional simulation times will grow rapidly with the number of components. Hence, we argue that the tie line intersection technique offers a significant advantage over conventional simulation.

4.5 Conclusions

The analysis and examples reported here demonstrate that:

1. A modified negative flash calculation can be performed that yields convergent solutions for composition points far outside the two-phase region, for compositions outside the phase diagram, and for compositions on extensions of near-critical tie-lines.

2. For fully self-sharpening systems in which a gas containing one component displaces a multicomponent oil, the modified negative flash can be used to find the sequence of key tie lines from the fact that one component disappears across each shock. The MMP is the lowest pressure at which one of the key tie lines is a critical tie line.

3. For fully self-sharpening systems in which a gas containing two components displaces a four-component oil, the crossover tie line can be found by solving the full set of tie line intersection equations simultaneously. The MMP can then be found as the lowest pressure at which one of the key tie lines is a critical tie line.

4. For systems that are not fully self-sharpening, it is still reasonable to assume that all key tie lines intersect each other. The same approach can then be used to calculate the MMP.

5. The proposed MMP calculation method can be extended to apply to a general system with an arbitrary number of components.

5. Development of a Streamline Based Reservoir Simulator

Rod Batycky, Marco Thiele and Martin Blunt

We present a new streamline-based simulator applicable to field scale flow. The method is three-dimensional (3D) and accounts for changing well conditions that result from infill drilling and well conversions, heterogeneity, mobility effects, and gravity effects. The key feature of the simulator is that fluid transport occurs on a streamline grid, rather than between the discrete gridblocks on which the pressure field is solved. The streamline grid dynamically changes as the mobility field and boundary conditions dictate. A general numerical solver moves the fluids forward in space and time along each streamline. Multiphase gravity effects are accounted for by an operator-splitting technique that also requires a numerical solver. Because fluid transport is decoupled from the underlying grid, the method is computationally efficient and very large time steps can be taken without loss in solution accuracy.

We present results of the streamline-based simulator applied to tracer, waterflooding, and first-contact miscible (FCM) displacements in two and three dimensions. Where possible, comparisons with conventional methods indicate that the streamline model minimizes numerical diffusion and is up to two orders of magnitude faster. We also demonstrate the efficiency of the method on a field scale, million-gridblock 36-well waterflood that includes a pattern modification plan to improve oil recovery. Lastly, we present results of the method applied to the House Mountain waterflood in Canada.

5.1 Introduction

The use of streamlines and streamtubes to model convective displacements in heterogeneous media has been presented many times since the early works of Muskat[114, 115, 116], Fay & Prats[117], and Higgins & Leighton[118, 119, 120]. Important contributions to the field are also due to Parsons[121], Martin & Wegner[122], Bommer & Schechter[123], Lake *et al.*[124], Emanuel *et al.*[125], and Hewett & Behrens[126, 127].

Streamline methods have recently resurfaced as a viable alternative to traditional finite-difference methods for large, heterogeneous, multiwell, multiphase simulations[128, 129, 130, 131, 132, 133, 134, 135, 136, 137, 138, 139, 140]. The efficiency of the method has made it an ideal tool for ranking equiprobable reservoir images [141], rapid assessment of production strategies such as infill drilling and gas injection [142], computing upscaled component flux properties for compositional simulation [143], and integration with production data for reservoir characterization [144]. The method has also allowed for the solution of fine-scale models ($\mathcal{O}(10^6)$ gridblocks) on standard computer resources, thus reducing the need for significant upscaling.

In this report we present advances on our previous work where we mapped analytical solutions along streamlines [132, 135]. Although the streamline paths were updated periodically to account for changing mobility fields, the method could not account for changing well conditions or gravity – two key phenomena that must be modeled in general field scale simulations.

We account for these mechanisms by mapping one-dimensional (1D) numerical solutions along streamlines, as first proposed by Bommer & Schechter[123]. In doing so, nonuniform initial conditions that appear along recalcuated streamline paths, resulting from changing well and mobility conditions, can be moved forward in space and time correctly. Streamline paths are updated

and the transport process repeated. The grid on which the pressure field is solved is effectively decoupled from the streamline grid used to transport fluids. There is no longer a global grid Courant-Friedrichs-Lewy (CFL) condition to restrict time step size. Furthermore, grid orientation and numerical diffusion effects are minimized. Finally, operator-splitting is used to account for gravity in multiphase flow [145, 146]. After moving fluids convectively along streamlines, fluids are then moved vertically along 1D gravity lines. Bratvedt *et al.*[137] presented a similar operator-splitting technique in the context of their front tracking method.

Our application of streamlines to field scale reservoir simulation is a combination of four existing ideas: (1) 3D streamlines [147], (2) updating the streamline paths to account for changing mobility field and well conditions [122, 128, 132], (3) numerical solutions along streamlines [123], and (4) including gravity effects in multiphase flow using operator-splitting [136, 137, 145, 146]. Using streamlines and gravity lines decouples the 3D transport problem into multiple 1D problems and leads to a very fast and accurate method applicable to a wide range of field conditions.

5.2 The Streamline Method

In this section we outline the streamline method. For a detailed discussion on how to trace the streamlines we refer the reader to the Appendix.

5.2.1 Governing IMPES Equations

The streamline method is an IMPES method. Ignoring capillary and dispersion effects, the governing equation for pressure p, for incompressible, multiphase flow is given by

$$\nabla \cdot \vec{\vec{k}} \cdot (\lambda_t \nabla p + \lambda_g \nabla D) = 0, \tag{5.1}$$

where D represents a depth below datum. The total mobility λ_t and the total gravity mobility λ_g are defined as

$$\lambda_t = \sum_{j=1}^{n_p} \frac{k_{rj}}{\mu_j}, \qquad \lambda_g = \sum_{j=1}^{n_p} \frac{k_{rj}\rho_j g}{\mu_j}. \tag{5.2}$$

k_{rj} is the relative permeability of phase j, μ_j is the phase viscosity, ρ_j is the phase density, g is the gravity acceleration constant, and n_p is the number of phases present. We also require a material balance equation for each phase j [148],

$$\phi \frac{\partial S_j}{\partial t} + \vec{u}_t \cdot \nabla f_j + \nabla \cdot \vec{G}_j = 0. \tag{5.3}$$

The total velocity $\vec{u}_t$ is derived from the 3D solution to the pressure field (Eq. 5.1) and application of Darcy's Law. The phase fractional flow is given by

$$f_j = \frac{k_{rj}/\mu_j}{\sum_{i=1}^{n_p} k_{ri}/\mu_i}, \tag{5.4}$$

and the phase velocity due to gravity effects is given by

$$\vec{G}_j = \vec{\vec{k}} \cdot g f_j \nabla D \sum_{i=1}^{n_p} k_{ri}(\rho_i - \rho_j)/\mu_i. \tag{5.5}$$

Eqs. 5.1 and 5.3 form the IMPES set of equations in the formulation of the streamline simulator. We will confine our discussion to the solution of these equations for two-phase flow.

5.2.2 Coordinate Transform

In a conventional IMPES finite-difference simulator Eq. 5.3 is solved in its full 3D form using the previously calculated pressure field. In the streamline method, we transform the 3D equation into multiple 1D equations that are solved along streamlines.

Streamlines are launched from gridblock faces containing injectors. As the streamlines are traced from injectors to producers we determine the time-of-flight along the streamline, which is defined as [129, 147]

$$\tau = \int_0^s \frac{\phi}{|\vec{u}_t(\zeta)|} d\zeta, \tag{5.6}$$

and gives the time required to reach a point s on the streamline based on the total velocity $\vec{u}_t(\zeta)$ along the streamline. The permeability, porosity, and total mobility effects of the 3D Cartesian domain are incorporated along a streamline via the τ coordinate.

To determine the coordinate transform, we rewrite Eq. 5.6 as

$$\frac{\partial \tau}{\partial \zeta} = \frac{\phi}{|\vec{u}_t|}, \tag{5.7}$$

which can further be rewritten as

$$|\vec{u}_t| \frac{\partial}{\partial \zeta} \equiv \vec{u}_t \cdot \nabla = \phi \frac{\partial}{\partial \tau}. \tag{5.8}$$

Substituting Eq. 5.8 into Eq. 5.3 gives

$$\frac{\partial S_j}{\partial t} + \frac{\partial f_j}{\partial \tau} + \frac{1}{\phi} \nabla \cdot \vec{G}_j = 0. \tag{5.9}$$

Eq. 5.9 is the governing pseudo-1D material balance equation for phase j along a streamline coordinate. The equation is pseudo-1D since the gravity term is typically not aligned along the direction of a streamline. To solve Eq. 5.9 we split the equation into two parts based on operator-splitting as outlined by Glimm *et al.*[146], Colella *et al.*[145], and Bratvedt *et al.*[137]. First, a convective step along streamlines is taken governed by

$$\frac{\partial S_j^c}{\partial t} + \frac{\partial f_j}{\partial \tau} = 0, \tag{5.10}$$

to construct an intermediate saturation distribution S_j^c. Then, a gravity step is taken along gravity lines using

$$\frac{\partial S_j}{\partial t} + \frac{1}{\phi} \frac{\partial G_j}{\partial z} = 0, \tag{5.11}$$

with S_j^c as the initial condition to construct S_j, and $G_j = |\vec{G}_j|$. For simplicity, we have assumed that the z-coordinate direction is aligned with the gravity lines.

1D Numerical Solvers

One-dimensional numerical solvers are used to solve Eqs. 5.10 and 5.11. Each solver is completely decoupled from the rest of the simulator. Here we have chosen to solve Eq. 5.9 but in fact any equation with the desired physics written in 1D can be used. For example, this method has been extended to compositional displacements [140].

For cases presented here, Eq. 5.10 is solved numerically using a single-point upstream (SPU) weighting scheme explicit in time. By discretizing in τ space, this leads to a natural refinement in 1D where flow velocities are high and reduced resolution where flow velocities are low. To retain

accuracy within the numerical solver the irregular spaced τ-grid is converted to a regular spaced τ-grid. Time stepping for the SPU scheme is controlled within the solver using the optimal local CFL constraint particular to a given streamline such that the fastest front is always moved one τ node per local time interval (Δt_{1D}). The ability to honor the local CFL constraint minimizes numerical diffusion.

For the gravity solver, Eq. 5.11 is discretized in space limited to the same vertical resolution of the underlying grid on which the pressure field is defined. Eq. 5.11 is solved using an explicit upstream weighting method outlined by Sammon [149]. An additional advantage of decoupling the gravity step in this way is that Eq. 5.11 is only solved in flow regions where gravity effects are important. For example, in locations where fluids are completely segregated, Eq. 5.11 will not be solved since $\partial G/\partial z$=0.

Time Stepping

In field scale displacements the streamline paths change with time due to the changing mobility field and/or changing boundary conditions. Thus the velocity field is updated periodically in accordance with these changes, by solving for the pressure.

To move the 3D solution forward in time globally by Δt from t^n to t^{n+1}=t^n+Δt we use the following algorithm:

1. At the start of a new time step, t^{n+1}, solve for pressure using Eq. 5.1. We solve Eq. 5.1 using a standard seven-point finite difference scheme, with no-flow boundary conditions over the surface of the domain and specified pressure or rate at the wells. The resulting linear set of equations is solved using a multigrid method [150].

2. Apply Darcy's Law to determine the total velocity at gridblock faces of the 3D Cartesian domain.

3. Trace streamlines from injectors to producers as outlined in the Appendix. For each streamline we do the following: (a) While tracing a streamline, the current saturation information from each gridblock that the streamline passes through is recorded. In this manner, a profile of saturation versus τ is generated for the new streamline. (b) Move the saturations forward Δt by solving Eq. 5.10 numerically in 1D. This will involve several timesteps within the numerical solver since $\Delta t \gg \Delta t_{1D}$. (c) Map the new saturation profile back to the original streamline path and onto the underlying grid.

4. Average all the streamline properties within each gridblock of the 3D domain to determine the saturation distribution at t^{n+1}.

5. If $G_j \neq 0$ include a gravity step that traces gravity lines from the top of the domain to the bottom of the domain along $\vec{g}$. For each gravity line we do the following: (a) The saturation distribution calculated in the convective step as a function of z is traced along a gravity line. (b) The saturations are moved forward by Δt using Eq. 5.11. (c) Map the new saturation profile back to the original gravity line and onto the underlying grid.

6. If $G_j \neq 0$ average all gravity line properties within each gridblock of the 3D domain to determine the final saturation distribution at t^{n+1}.

7. Return to Step 1.

In the above time stepping scheme, for tracer displacements with fixed boundary conditions the streamline paths do not change with time. The pressure field is only calculated once. Δt represents a global convective time step between remappings. For nonlinear displacements (changing streamline paths), each global time step includes a pressure solve and a remapping step.

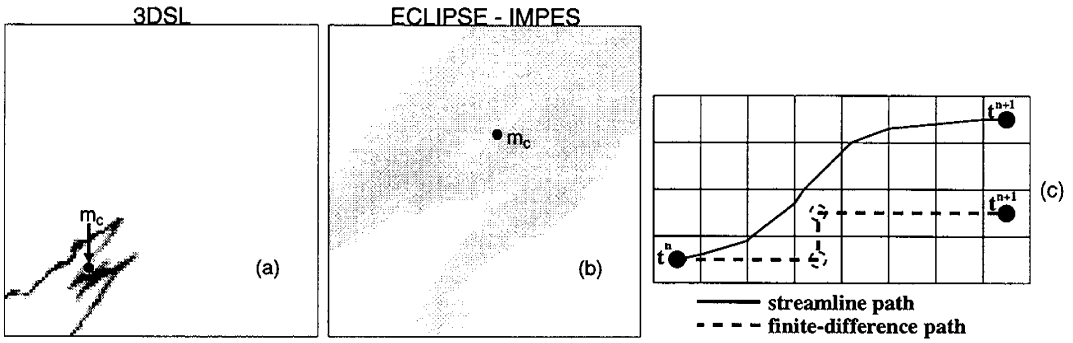

Figure 5.1: Distribution of a tracer slug using (a) the streamline method and (b) ECLIPSE-IMPES. m_c is the center of mass of the tracer slug. (c) Conceptual picture illustrating the final position of a fluid element at the end of time interval Δt by transporting along a streamline vs. the underlying Cartesian grid.

5.3 Tracer Displacements

In our first example, a small slug of tracer is injected into a 100×100 heterogeneous quarter-five spot model. The slug distribution at t_D=0.07 is shown in Figure 5.1 for the streamline simulator (3DSL) and ECLIPSE-IMPES[151] with a SPU scheme. This comparison demonstrates how conventional grid-based methods can suffer from large amounts of numerical diffusion and move fluid in the wrong direction. In contrast, the streamline method automatically captures the correct flow direction and moves fluid with minimal numerical diffusion. Note the difference in the location of the center of mass m_c of the slug predicted by the two methods.

Figure 5.1c illustrates conceptually the difference between the two methods. The efficiency of the streamline method is a result of being able to take large global time steps along streamline paths. The CFL constraints of the underlying grid have been decoupled from transport and there is no limit to the size of Δt. For a conventional method, because transport is restricted to Cartesian directions, small global time steps must be taken but will not guarantee the same path as a streamline path. For this example, the streamline method required 2 time steps to move the slug profile in Figure 5.1 whereas ECLIPSE required over 900 time steps.

For both the streamline simulator and conventional methods, saturation information is only known at the scale of a single gridblock. Each time we map the streamline saturation information to the underlying grid we mix all of the streamline saturations within each gridblock. For the numerical solutions, these mixed properties are then picked up at the next time step and moved forward. In this manner streamlines communicate with each other within each gridblock after a global time step. The number of remappings will influence the level of mixing present in the solution. We will study this mixing next and compare results with those from mapping an analytical solution along streamlines [132, 135], which for tracer displacements give exact results in the case of no physical dispersion or diffusion.

For the numerical solutions, G_j=0 in Eq. 5.11 and S_j=f_j=C, where C is the tracer concentration, in Eq. 5.10. Figure 5.2 shows a comparison of tracer flow results in a heterogeneous 250×100 medium for the exact solution (mapping the analytical 1D tracer profile) and the numerical mapping technique using both a SPU scheme and a high-order TVD scheme [45] to solve Eq. 5.10. The use of TVD schemes for transport equations along streamlines is discussed in detail elsewhere [139, 140]. Taking the entire time step Δt within the 1D solver and mapping only once to the underlying grid (Figure 5.2b,d) gives results almost identical to the reference solution. There is no difference between using a SPU or a TVD scheme. This is because we move fluid at the

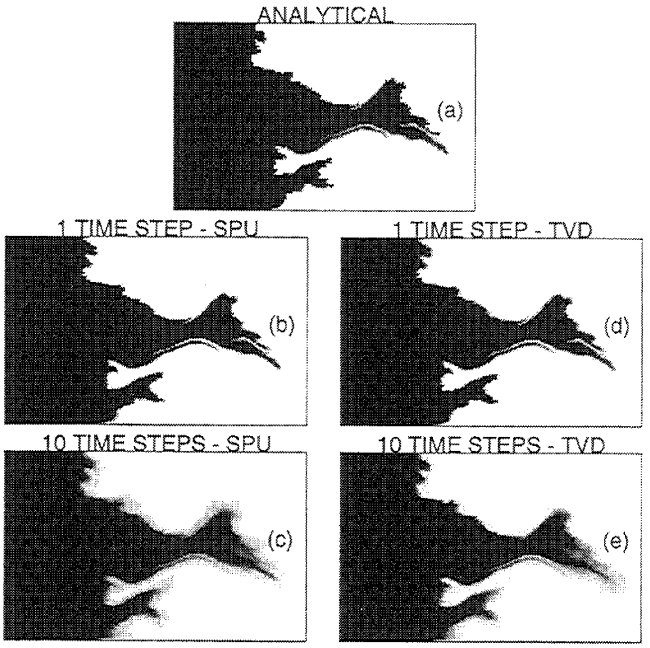

Figure 5.2: Comparison of tracer profiles in a 250×100 heterogeneous domain using the streamline simulator: (a) mapping an analytical tracer solution along streamlines, (b) mapping a SPU (numerical) solution with 1 remapping step, (c) mapping a SPU solution with 10 remapping steps, (d) mapping a TVD (numerical) solution with 1 remapping step, (e) mapping a TVD solution with 10 remapping steps.

optimum CFL number along a streamline, such that the fastest front moves one τ interval per local time step Δt_{1D}. Under this condition a SPU scheme will not suffer from numerical diffusion and is equivalent to a high-order scheme. We see similar behavior for waterflood displacements. Thus, for the remaining cases in this report we use the SPU scheme. However, for more complex 1D systems, where the front speed is not known analytically – such as compositional displacements – a TVD scheme can offer improved accuracy [140].

If the convective time step is reduced by a factor of 10, then 10 time steps are taken to reach t_D=0.3. There are 10 remappings to the underlying grid resulting in the saturation profiles shown in Figure 5.2c,e. Again there is no difference between the SPU or TVD scheme. However, there is more diffusion than in Figure 5.2b,d, and it is due to increased mixing of streamline properties at the gridblock scale.

As we show later, for nonlinear displacements where the flow field changes with time, the streamline method requires only 10's of time steps per pore volume injected (PVI) to produce converged results. The degree of mixing is approximately that shown in Figure 5.2c,e and is smaller than numerical diffusion in conventional methods. This is important since numerical diffusion can feed back into errors in the flow field calculation, resulting in compounding errors in recovery predictions.

5.4 First-Contact Miscible Displacements

For first-contact miscible displacements we use Eq. 5.10 with S_j=f_j=C, where C is the concentration of the miscible injectant. Effective phase viscosities and densities are calculated using the Todd & Longstaff method [152]. For all cases shown here the Todd & Longstaff mixing

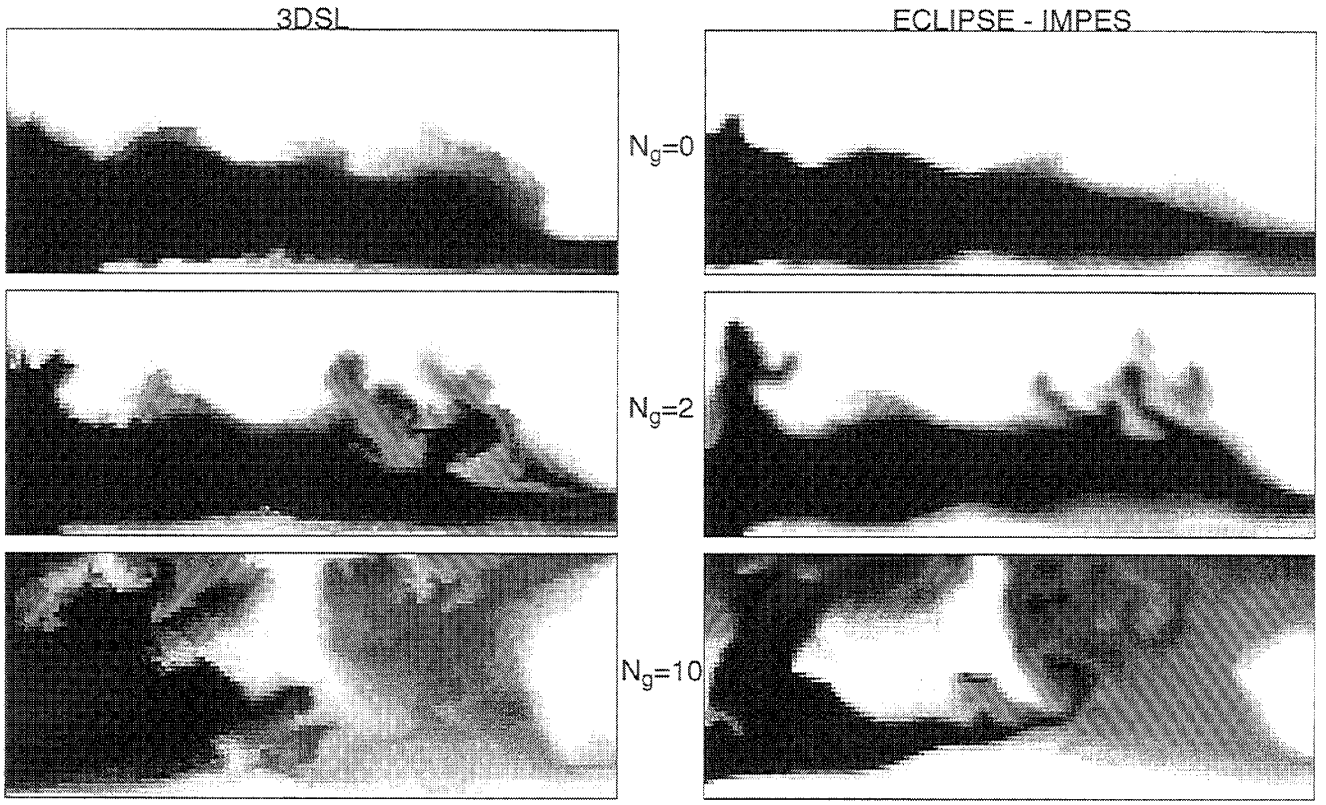

Figure 5.3: Comparison of FCM solvent profiles between 3DSL and ECLIPSE at t_D=0.6 in a 125×50 heterogeneous model at three gravity numbers. Injection is into the lower 10 left gridblocks and production is from the lower 10 right gridblocks.

parameter is assumed to be ω=1. This implies that fluid properties between the miscible phases are completely mixed at the gridblock scale. As a result the effective phase densities within any gridblock are equal (G_j=0) and only Eq. 5.10 governs transport.

We define a gravity number as [153]

$$N_g = \frac{\overline{k}_V \Delta\rho g L^2}{\overline{k}_H (\overline{\Delta p}_H) h}, \tag{5.12}$$

where $\overline{k}_V$ and $\overline{k}_H$ are average vertical and horizontal permeabilities respectively, $\Delta\rho$ is the pure fluid density difference, $\overline{\Delta p}_H$ is the pressure drop in the horizontal direction, L is the distance between wells, and h is the model height.

Shown in Figure 5.3 are the solvent profiles for a 125×50 heterogeneous system at t_D=0.6 for the streamline method at three different gravity numbers. Injection is in the lower ten gridblocks on the left and production is from the lower ten gridblocks on the right. The pure fluid viscosity ratio was kept constant at 10, and phase densities were altered to change the gravity number. Clearly, the streamline simulator (3DSL) can model gravity dominated FCM displacements as seen by the increased amount of solvent rising in the model as gravity forces are increased. For comparison, ECLIPSE-IMPES two-point upstream weighting results with the same parameters are also shown in Figure 5.3. The solvent distributions are similar between the two methods, although there appears to be more detail in the 3DSL pictures. A summary of oil recovery is shown in Figure 5.4 for each gravity number. In general, ECLIPSE under predicts recovery compared to the streamline method. There appears to be more numerical diffusion within ECLIPSE which causes increased

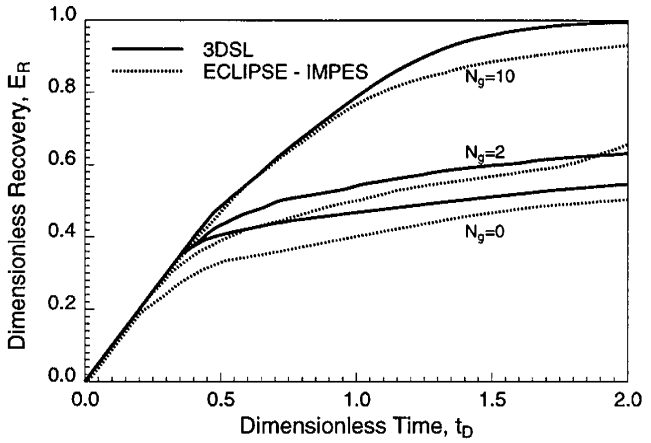

Figure 5.4: FCM displacement recovery comparisons between 3DSL and ECLIPSE, for three different gravity numbers.

mixing of the solvent and oil. This in turn reduces the effective density between the two fluids and the ability of the solvent to rise and displace oil, giving lower predicted recoveries than 3DSL. Heterogeneous FCM displacements are very difficult to model with conventional methods since the solution is highly susceptible to numerical diffusion [154, 153].

Running on a standard UNIX workstation (DEC AlphaServer 2100 4/275 256MB RAM), ECLIPSE results for this small problem with N_g=10 required 32,767 time steps and 6.26 days of CPU time to reach t_D=2, whereas the streamline method only required 306 time steps and 10.3 minutes of CPU time. This translates into a speed-up factor of 875. For N_g=2, the speed-up factor was 504, and for N_g=0 the speed-up factor was 280. Although not shown here, ECLIPSE fully implicit results were also calculated. CPU usage was reduced but the results exhibited considerably more numerical diffusion and very poor agreement with the streamline solutions. Finally, the ECLIPSE SPU scheme was not considered due to poor agreement with the two-point method and a high-order flux corrected transport method [135, 154].

5.5 Two-Phase Displacements

Here we consider immiscible, two-phase displacements. We now include a gravity step (Eq. 5.11) to allow fluids to equilibrate vertically after a convective step (Eq. 5.10).

As a first example we show a two-dimensional (2D) waterflood displacement in a 19,000 gridblock (250×75) heterogeneous model. The fluid viscosity ratio is μ_o/μ_w=15, the density difference is 500 kg/m^3, and the flowrate was adjusted to vary the gravity number. Shown in Figure 5.5 are the water saturation profiles using 3DSL, for three different gravity numbers. The streamline method does account for gravity effects in two-phase flow as can be seen by the increased amount of water sinking in the model as the gravity number increases. For comparison we also include the standard SPU, ECLIPSE-IMPES results in Figure 5.5. The saturation profiles for the streamline method show more detail and less numerical diffusion than the ECLIPSE results. Although not shown, oil recovery predictions by the two methods are very similar for all gravity numbers. This was expected since waterfloods are stable displacements affected only minimally by numerical diffusion. For this model the speedup factor for N_g=0 was 11, for N_g=0.4 the speedup factor was 4, and for N_g=10 the speedup factor was 3. The reduction in speedup factor as N_g increases is due to the need to update the streamline paths more often in order to honor the additional nonlinearity due to gravity effects.

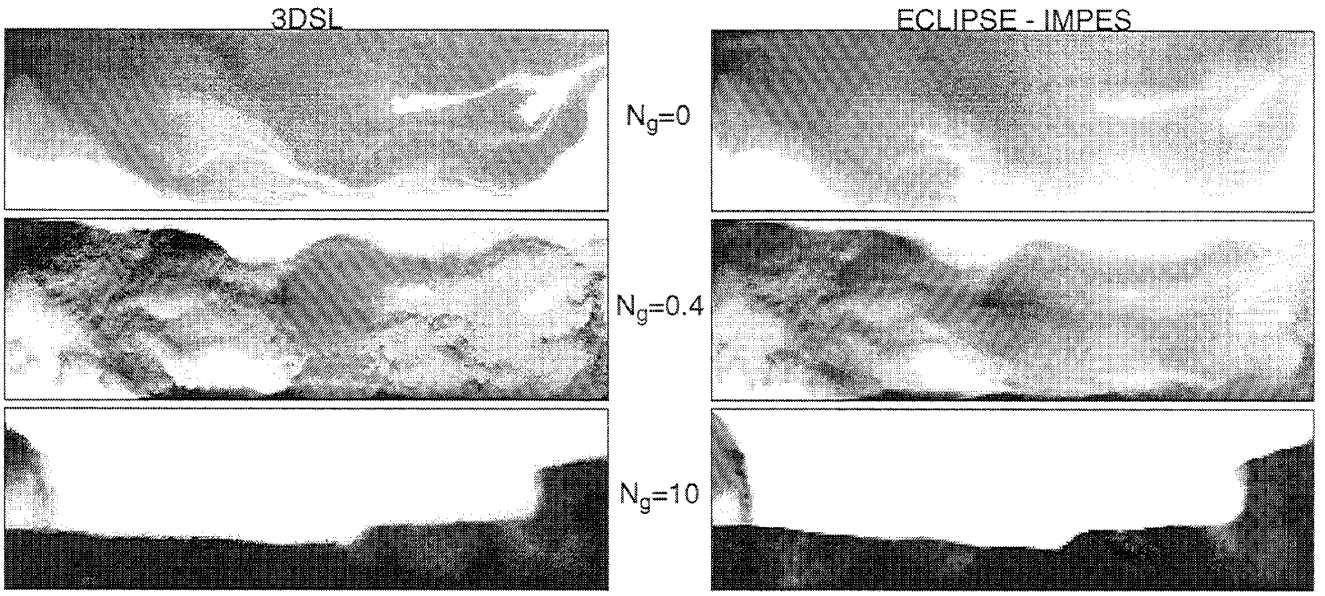

Figure 5.5: Comparison of water saturation profiles between 3DSL and ECLIPSE at t_D=0.4 in a 250×75 heterogeneous model at three gravity numbers. Injection is into the upper 10 left gridblocks and production is from the upper 10 right gridblocks.

As a second example we solve a 100,000 gridblock (100×100×10) 5-spot waterflood with and without gravity. An injection well is located in the lower two central gridblocks, and a production well is located in the upper two gridblocks in each corner of the model. The water distributions with and without gravity using 3DSL are shown in Figure 5.6. We compare the streamline results against the ECLIPSE-IMPES SPU method. Figure 5.7 shows that the oil recovery predicted by the two methods is similar, although there are some small differences for the N_g=1 case. We attribute these differences to grid orientation effects in ECLIPSE and the ability of 3DSL to better model the water cone to each producer. For the case N_g=0, the streamline model required 50 minutes run time while the equivalent ECLIPSE model required 101 hours run time, a speedup factor of 121. For the case N_g=1.0, the streamline model required 5.4 hours run time while ECLIPSE required 297 hours (12.4 days) run time, a speedup factor of 55.

5.6 Million Gridblock Waterflood

A major limitation of previous streamline models was the inability to account for changing well conditions. Mapping numerical solutions along the streamlines removes this deficiency and allows for shut-in of wells, conversion of producers to injectors, and infill drilling.

We illustrate this flexibility with a field scale problem, a 1.16 million gridblock (220×220×24) waterflood model containing 9 producers and 9 injectors in 5-spot patterns. The permeability field, generated using sequential Gaussian simulation [155], is highly heterogeneous with a permeability trend aligned diagonal to the 5-spots. The correlation length is λ_c=0.25 in the on-trend direction, λ_c=0.03 in the off-trend direction, and λ_c=0.17 in the vertical direction. The producers are completed in the upper 12 gridblocks and the injectors are completed in the lower 12 gridblocks. At t_D=0.4 all the producers are recompleted in the lower portion of the model and converted to injectors, while 16 additional infill producers are added to give a line-drive waterflood.

The million gridblock model was run using 3DSL on a standard workstation and required

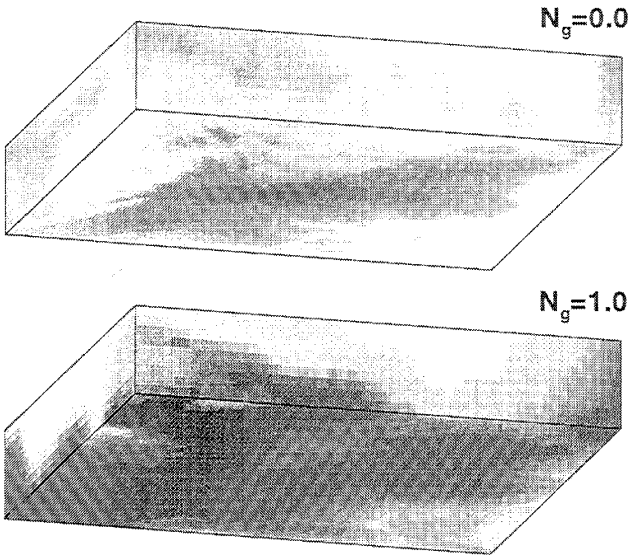

Figure 5.6: Water saturations predicted using 3DSL with and without gravity (100,000 gridblocks). Injection is in the central bottom two gridblocks, production is from the top two gridblocks of each corner.

50 hours for the base case recovery curve, and 40 hours for the incremental results. The base case and incremental recovery due to the pattern modifications are shown in Figure 5.8. We could not run this model with ECLIPSE using our current computer resources. To compare with ECLIPSE, the model was upscaled by a factor of 16 to 72,000 gridblocks (110×110×6) using geometric averaging of absolute permeability. Relative permeabilities were not altered for the coarse scale model. The oil recovery results for ECLIPSE-IMPES SPU are also shown in Figure 5.8. For this model the ECLIPSE base case recovery curve required 55 hours run time, while the incremental results required 13 hours run time. It is worth noting that an ECLIPSE fully implicit solution for the base case model required 120 hours run time due to time step convergence problems for this size model. Included for reference are 3DSL upscaled results, which required 28 minutes run time for the base case and 22 minutes run time for the incremental case.

As seen in Figure 5.8, incremental oil recovery due to infill drilling is underestimated in the upscaled model. This is because upscaling leads to a larger over prediction of oil recovery for the base case 5-spot model, than for the line-drive model. We attribute this to the difference in the inter-well permeability correlation lengths, which are 50% smaller in the line-drive pattern than the 5-spot pattern. This comparison highlights two points: (1) the ECLIPSE base case model was 16 times smaller than the 3DSL model, yet both required approximately the same run time, and (2) ignoring fine-scale heterogeneity can lead to an over optimistic prediction of field performance.

5.7 Convergence

A key issue in the streamline method is how large a global time step Δt can be allowed between pressure solves before the streamline paths require updating. For a conventional IMPES scheme the maximum time step size is linked to the grid CFL constraint dictated by the largest flow velocity anywhere in the domain (typically near a well). Small time steps result, causing fronts in most of the domain to move at far less than the optimal one gridblock per time step giving rise

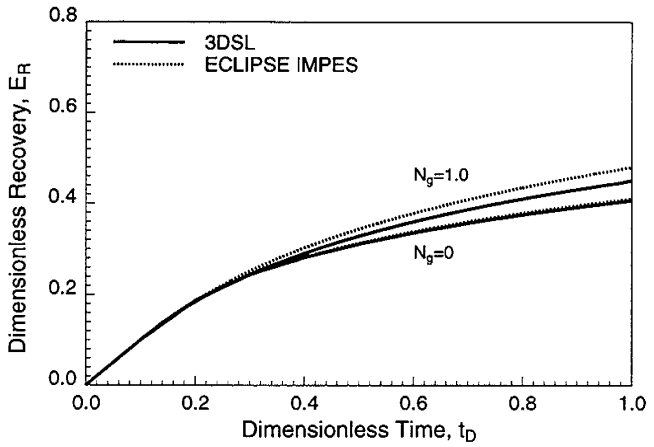

Figure 5.7: Waterflood displacement recovery comparison between 3DSL and ECLIPSE for a 3D model (100,000 gridblocks) with two different gravity numbers.

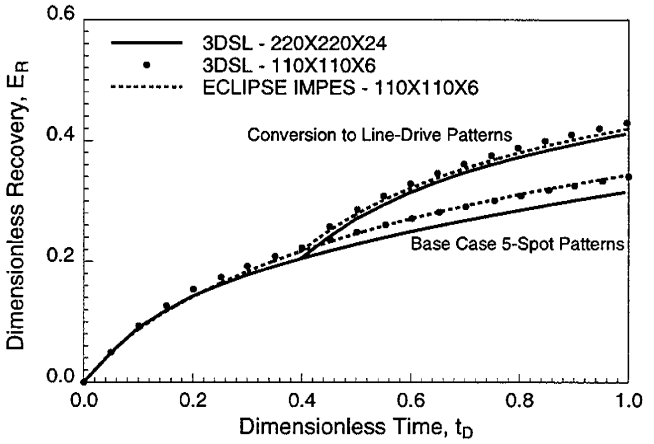

Figure 5.8: Waterflood oil recovery comparisons between 3DSL million gridblock model and up-scaled ECLIPSE-IMPES and 3DSL models.

to significant levels of numerical diffusion. Moreover, the pressure field is unnecessarily recomputed at each time step based on saturation changes at a sub-gridblock scale. A fully implicit method overcomes the drawback of small time steps, but the trade-off is increased numerical diffusion and nonlinear convergence problems.

For the streamline method, the fastest front can be moved at substantially more that a single gridblock per global time step since fluid transport is decoupled from the underlying grid. Moving the fastest front at a single gridblock per time step actually represents the desired lower limit on time step size. The maximum time step size is governed by a global constraint – the nonlinearity of the displacement. The magnitude of the nonlinearity is a function of heterogeneity, fluid properties, displacement type, and boundary conditions. The weaker the nonlinearity, the larger the time step allowable. Convective dominated displacements in heterogeneous domains with multiple wells gives rise to streamline paths that change little between time steps. This class of problems is ideal for the streamline method, but is particularly difficult for conventional grid-based methods.

We illustrate convergence of the method on the 2D cross-sectional FCM and waterflood models at each gravity number. All results presented in this report are converged solutions. In this

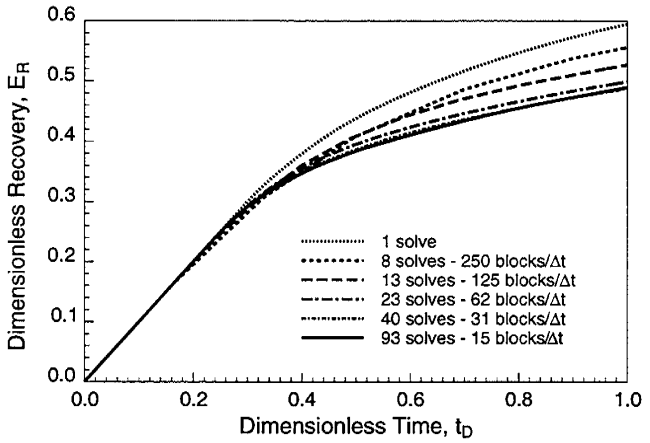

Figure 5.9: Convergence of oil recovery curve as maximum front speed is reduced from 250 to 15 gridblocks per time step, for 250×75 waterflood displacement, N_g=0.4.

report, we define convergence of a displacement based on changes to the recovery curve as time step size is reduced. For these test cases we implemented an automatic time stepping algorithm that moves the fastest front along the fastest streamline a predetermined number of gridblocks per time step. This time stepping method has the added advantage of automatically increasing time step sizes after breakthrough. For example, Figure 5.9 illustrates changes to oil recovery for the 250×75 waterflood at N_g=0.4, as maximum front movement is reduced from 250 to 15 gridblocks per time step. For this case there is no change between 31 and 15 gridblocks per time step so the solution is considered converged at 31 gridblocks per time step, or equivalently, 40 pressure solves. To summarize our results for the waterflood, as N_g changed from 0 to 0.4 to 10, optimal front movement changed from 25 to 31 to 2 gridblocks per time step. The corresponding ECLIPSE-IMPES results gave approximately 0.35, 0.62 and 0.28 gridblocks per time step. Note for this case, adding a small amount of gravity (N_g=0.4) increased the overall effect of heterogeneity on the displacement giving a higher maxmimum front speed than without gravity. For the FCM cases, which are inherently more nonlinear, as N_g increased from 0 to 2 to 10, optimal front movement dropped from 5 to 2 to 1 gridblocks per time step. By contrast, approximate front speed movements for ECLIPSE-IMPES were 0.14, 0.03, and 0.01 gridblocks per time step.

These results highlight the following: (1) the more nonlinear a problem, due to displacement physics (waterflood vs FCM) and gravity, the smaller the time step required to achieve convergence, (2) the streamline method converges as the maximum front speed is reduced, (3) for heterogeneous displacements, optimal front speeds are typically larger than the minimum of a single gridblock per time step, and (4) using conventional grid based methods result in front speeds far less than optimum.

The maximum global time step size is also related to boundary conditions. When history matching, for example, well information may be changing at specific time intervals. These time intervals would represent limits in the maximum global time step size. How the streamline method performs under this scenario is illustrated in the next section.

5.8 Field Example - House Mountain Waterflood

We summarize the application of the streamline simulator using the House Mountain waterflood in central Alberta as an example. The Shell in-house simulator MORES was used to model a 56 well portion of the waterflood [156]. The data set consisted of 21,000 active gridblocks, 7

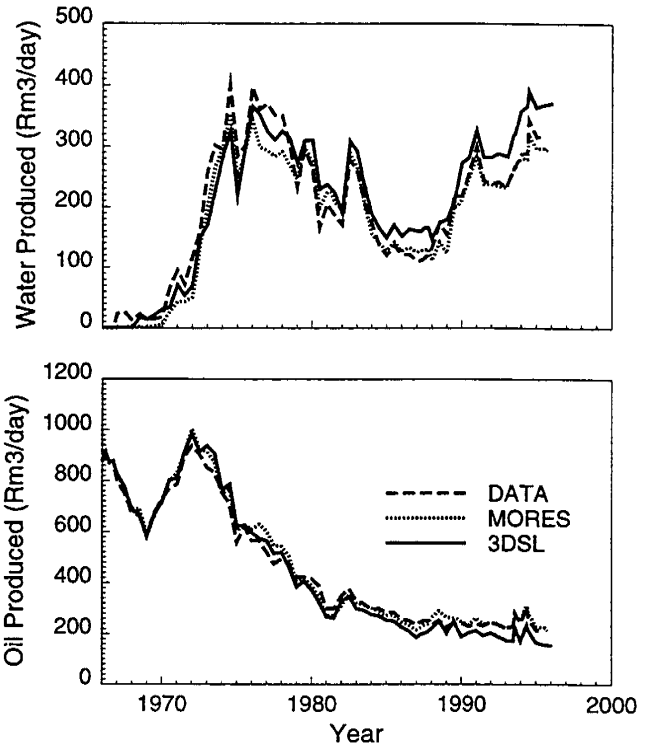

Figure 5.10: Comparison of historical production rate data with history matches for the streamline simulator (3DSL) and a conventional implicit simulator (MORES).

grid layers, three main rock types, and included vertical barriers in the southern half of the model. Production data consisted of 30 years of history at 6 month intervals with standard shut-ins and start-ups, 14 well abandonments, and 2 infill and 2 horizontal redrills added. The MORES simulation specified total liquid production only. The quality of the history match was defined on predicted water production performance on a well-by-well basis.

To input the data set into 3DSL the major assumption required was that the system be strictly incompressible. The assumption was not a major limitation in this case since the voidage replacement ratio was approximately 1. No tuning of the streamline history match was performed. Figure 5.10 summarizes the field oil and water production rates for MORES and 3DSL compared with the field data. Post-breakthrough prediction is excellent, although there is some deviation in the 3DSL results after 1985. We believe that this is a result of over prediction of water rates at two southern producers and is due to assuming only a single rock type within 3DSL.

For this 21,000 gridblock model, there was only a minimal speed advantage using 3DSL compared with the fully implicit MORES model. This is a result of historical well data limiting the time step size to 6 month intervals. However, we were also able to run a downscaled 201,000 gridblock model with 3DSL in 10.5 CPU hours. The ability to run a fine scale model translates into either incorporating more heterogeneity in the existing model, or including the entire field. A field-wide simulation eliminates the need to account for leak-off in pattern type simulations and gives true field-wide performance predictions.

5.9 Discussion and Limitations

The streamline method is ideally suited for large, heterogeneous, multiwell problems that are convectively dominated. This is a class of problems that is particularly challenging for conventional

numerical techniques. For these cases, the streamline simulator can represent the difference between solving a problem and not solving it at all. However, the method is not applicable to all situations and the results presented here do ignore the following effects:

1. We have assumed that the fluids are incompressible. For compressible flow, streamlines are still defined, but they do not always originate or end at wells. The method can accommodate compressibility by solving a mass balance equation along the streamlines. However, for highly compressible single-phase flow, such as primary production, frequent recomputation of the pressure field is necessary and the method is unlikely to offer a significant speed advantage over conventional techniques.

2. The current method does not allow for transport between streamlines due to capillary effects or transverse dispersion. These effects could be accommodated using operator-splitting [157]. Fluids would be moved diffusively along the underlying grid after the convective and gravity steps. For situations where these effects are dominant, again the streamline method may offer little speed advantage over existing methods.

Because of the decoupled nature of the streamline method, it is easily extended to more general displacements by simply solving a different mass conservation equation along each streamline. For example, we have extended the method to compositional displacements [140], where multi-component phase behavior effects are accounted for in the 1D solver. We observe that the advantages of reduced numerical diffusion and increased speed for FCM and waterflood displacements are amplified for compositional displacements.

5.10 Conclusions

1. The underlying idea of the streamline method is to decouple a 3D problem into multiple 1D problems. Fluid transport is separated from the underlying grid and instead occurs along a dynamically changing streamline grid. The main advantage is that the grid CFL conditions are eliminated from fluid transport giving global time step sizes that are independent of the underlying grid constraints. Additionally the method reduces numerical diffusion. A streamline-based grid is ideal for convective dominated displacements in heterogeneous media.

2. The ability to take large time steps and a reduced number of pressure solves gives speedup factors between 1 and 2 orders of magnitude over conventional finite-difference methods. For waterflood and FCM displacements considered here, only 10's of pressure solves over 2 PVI were required, whereas conventional IMPES methods required 1000's or pressure solves and convective steps due to the grid CFL constraints. As shown, this increased efficiency translates into easily being able to solve million gridblock models.

3. The streamline method exhibits convergence as the time step size is reduced. The maximum time step size is dependent on the nonlinearity of the problem – the greater the nonlinearity, the smaller the time step size. In terms of front speeds, for all but cases with significant gravity effects, fronts can move at substantially greater than the minimum of 1 gridblock per time step. In comparison, conventional IMPES methods gave average front speeds substantially less than 1 gridblock per time step.

4. The streamline method was tested on a 56 well field waterflood with 30 years of production history. History matching results compared very well with a conventional simulation, although no tuning of the streamline model was performed.

5.11 Nomenclature

C = concentration
D = depth from datum, L
E_R = dimensionless recovery efficiency
f_j = fractional flow of phase j
$\vec{G}_j$ = j phase velocity due to gravity, L/t
g = gravitational acceleration constant, L/t^2
$g_{v,x}$ = velocity gradient across gridblock in x-direction, 1/t
h = height of model, L
$\vec{\vec{k}}$ = absolute permeability tensor, L^2
k_{rj} = relative permeability of phase j
$\overline{k}_H$ = average horizontal permeability, L^2
$\overline{k}_V$ = average vertical permeability, L^2
L = distance between producer and injector, L
m_c = center of mass
N_g = gravity number
n_p = number of phases
p = Pressure, M/t^{2}L
S_j = saturation of phase j
S_j^c = saturation of phase j after convective step
s = spatial distance coordinate along a streamline, L
t = time, t
t_D = dimensionless time
u_t = total Darcy velocity, L/t
v = interstitial velocity, L/t
x_e = x-position of streamline exit location, L
x_i = x-position of streamline inlet location, L
x, y, z = spatial coordinates
$\overline{\Delta p}_H$ = average pressure drop in horizontal direction, M/t^{2}L
Δt = global time step size, t
Δt_{1D} = time step size within 1D solver, t
$\Delta t_{e,x}$ = time-of-flight required to reach an x-exit face, t
$\Delta\rho$ = fluid density difference, M/L^3
ζ = local streamline coordinate, L
λ_c = permeability correlation length
λ_g = total gravity mobility, 1/Lt
λ_t = total mobility, Lt/M
μ_j = viscosity of phase j, M/Lt
ρ_j = density of phase j, M/L^3
τ = time of flight, t
ϕ = porosity
ω = Todd & Longstaff mixing parameter

5.12 Appendix: Tracing Streamlines

Streamlines are launched uniformly across the face of a gridblock containing an injector, with the number of streamlines launched proportional to the flux across the face. Thus each streamline between all producers and injectors carries the same flux. Not every gridblock in the domain will contain a streamline based on launching a finite number of streamlines. For these missed gridblocks we define a streamline by simply tracing back from each missed gridblock until an injector is reached.

Tracing streamlines from injectors to producers is based on the analytical description of a streamline path within a gridblock as outlined by Pollock [147] and Datta-Gupta & King [129]. The underlying assumption is that the velocity field in each coordinate direction varies linearly and is independent of the velocities in the other directions. This method is attractive because it is analytical and consistent with the governing material balance equation.

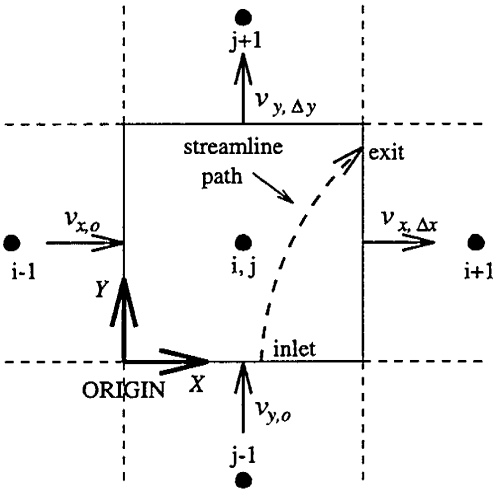

Figure 5.11: Schematic of a streamline path through a 2D gridblock of dimensions Δx by Δy.

Consider the two-dimensional gridblock in Figure 5.11, for which we know the interstitial velocity field and have defined a local coordinate system and origin. The velocity in the x-direction, v_x, is defined as

$$v_x = v_{x,o} + g_{v,x}(x - x_o), \tag{5.13}$$

where $g_{v,x}$ is the velocity gradient across the gridblock and is given by

$$g_{v,x} = (v_{x,\Delta x} - v_{x,o})/\Delta x. \tag{5.14}$$

Knowing that $v_x = dx/dt$, one can integrate Eq. 5.13 to yield the time required to reach an x-exit face $\Delta t_{e,x}$ as

$$\Delta t_{e,x} = \frac{1}{g_{v,x}} \ln \left\{ \frac{v_{x,o} + g_{v,x}(x_e - x_o)}{v_{x,o} + g_{v,x}(x_i - x_o)} \right\}, \tag{5.15}$$

where x_i is the inlet position and x_e is the exit position, in the x-coordinate direction. Similarly, the times required to reach the exit faces in the y or z directions are given by

$$\Delta t_{e,y} = \frac{1}{g_{v,y}} \ln \left\{ \frac{v_{y,o} + g_{v,y}(y_e - y_o)}{v_{y,o} + g_{v,y}(y_i - y_o)} \right\}, \tag{5.16}$$

and

$$\Delta t_{e,z} = \frac{1}{g_{v,z}} \ln \left\{ \frac{v_{z,o} + g_{v,z}(z_e - z_o)}{v_{z,o} + g_{v,z}(z_i - z_o)} \right\}. \tag{5.17}$$

The correct face which the streamline will exit is that which requires the smallest value of Δt_e calculated from Eqs. 5.15, 5.16, and 5.17. Knowing the minimum time the exact exit location of the streamline is determined by rewriting Eqs. 5.15, 5.16, and 5.17 as

$$x_e = \frac{1}{g_{v,x}} (v_{x,i} \exp\{g_{v,x}\Delta t_e\} - v_{x,o}) + x_o, \tag{5.18}$$

$$y_e = \frac{1}{g_{v,y}} (v_{y,i} \exp\{g_{v,y}\Delta t_e\} - v_{y,o}) + y_o, \tag{5.19}$$

$$z_e = \frac{1}{g_{v,z}} (v_{z,i} \exp\{g_{v,z}\Delta t_e\} - v_{z,o}) + z_o, \tag{5.20}$$

where v_i represents the inlet-velocity and v_o is the velocity at the origin coordinates.

For the case when velocity is uniform across a gridblock in a given direction (g_v=0), Eq. 5.15, for example, simply becomes $\Delta t_{e,x}$=(x_e-x_i)/$v_{x,o}$ and Eq. 5.18 becomes x_e=x_o+$\Delta t_{e,x} v_{x,o}$. Finally, for the situation where a flow divide exists in say the x direction within a gridblock, one must assure that the sign v_x at the inlet location is the same as the sign of v_x at a potential x exit face. This check also avoids the possibility of calculating negative logarithms in Eqs. 5.15, 5.16, and 5.17.

References

[1] Bryant, S. and M.J. Blunt. Prediction of relative permeability in simple porous media. *Physical Review A*, 46:2004–2011, August 1992.

[2] Bakke, S. and P.E. Oren. 3-d pore-scale modelling of sandstones and flow simulations in the pore networks. *SPE Journal*, June 1997.

[3] Nilsen, L.S., P.E. Oren, S. Bakke, and A. Henriquez. Prediction of relative permeability and capillary pressure from a pore model, paper SPE 35531 proceedings of the 1996 European 3-D Reservoir Modelling Conference, Stavanger, Norway, April.

[4] Oren, P.E., S. Bakke, L. Scandellari Nilson, and A. Henriquez. Prediction of relative permeability and capillary pressure from pore-scale modelling, proceedings of the 1996 5th European Conference on the Mathematics of Oil Recovery, Leoben, Austria, September.

[5] Blunt, M.J. Effects of heterogeneity and wetting on relative permeability using pore level modeling. *SPE Journal*, 2:70–87, March 1997.

[6] Jerauld, G.R. and S.J. Salter. The effect of pore-structure on hysteresis in relative permeabilty and capillary pressure: Pore-level modeling. *Transport in Porous Media*, 5:103–151, 1990.

[7] McDougall, S.R. and K.S. Sorbie. The impact of wettability on waterflooding: Pore-scale simulation. *SPE Reservoir Engineering*, 10:208–213, August 1995.

[8] Dixit, A.B., S.R. McDougall, and K.S. Sorbie. A pore-level investigation of relative permeability hysteresis in water-wet systems, paper SPE 37233 proceedings of the 1997 SPE International Symposium on Oilfield Chemistry, Houston, TX.

[9] Mohanty, K.K., and S.J. Salter. Multiphase flow in porous media part 3: Oil mobilization, transverse dispersion and wettability, paper SPE 12127 proceedings of the 1983 SPE Annual Technical Conference and Exhibition, San Francisco, CA.

[10] Oak, M. J., L.E. Baker, and D.C. Thomas. Three-phase relative permeability of berea sandstone. *Journal of Petroleum Technology*, 42:1057–1061, August 1990.

[11] Jerauld, G.R. Prudhoe Bay gas/oil relative permeability. *SPE Reservoir Engineering*, 12:66–73, Feb 1997.

[12] Chatzis, I., A. Kantzas, and F.A.L. Dullien. On the investigation of gravity-assisted inert gas injection using micromodels, long berea sandstone cores, and computer-assisted tomography, paper SPE 18284 proceedings of the 1988 63rd Annual Technical Conference and Exhibition of the SPE, Houston, TX, October.

[13] Soll, W. E., M.A. Celia, and J.L. Wilson. Micromodel studies of three-fluid porous media systems: Pore-scale processes relating to capillary pressure-saturation relationships. *Water Resources Research*, 29(9):2963–2974, 1993.

[14] Oren, P.E., J. Billiote, and W.V. Pinczewski. Mobilization of waterflood residual oil by gas injection for water-wet conditions. *SPE Formation Evaluation*, 7:70–78, March 1992.

[15] Oren, P.E. and W.V. Pinczewski. The effect of wettability and spreading coefficients on the recovery of waterflood residual oil by miscible gasflooding, paper SPE 24881 proceedings of the 1992 67th Annual Technical Conference and Exhibition of the SPE, Washington D.C., October.

[16] Oren, P.E. and W.V. Pinczewski. Fluid distribution and pore-scale displacement mechanisms in drainage dominated three-phase flow. *Transport in Porous Media*, 20:105–133, 1995.

[17] Keller, A. A., M.J. Blunt, and P.V. Roberts. Micromodel observation of the role of oil layers in three-phase flow. *Transport in Porous Media*, 26:277–297, 1997.

[18] Soll, W. E. and M.A. Celia. A modified percolation approach to simulating three-fluid capillary pressure-saturation relationships. *Advances in Water Resources*, 16(2):107–126, 1993.

[19] Oren, P.E., J. Billiote, and W.V. Pinczewski. Pore-scale network modelling of waterflood residual oil recovery by immiscible gas flooding, paper SPE 27814 proceedings of the 1994 Improved Oil Recovery Symposium, Tulsa, OK, April.

[20] Pereira, G.G., W.V. Pinczewski, D.Y.C. Chan, L. Paterson, and P.E. Oren. Pore-scale network model for drainage dominated three-phase flow in porous media. *Transport in Porous Media*, 24:167–201, 1996.

[21] Heiba, A. A., H.T. Davis, and L.E. Scriven. Statistical network theory of three-phase relative permeabilities, paper SPE 12690 proceedings of the 1984 4th DOE/SPE Symposium on Enhanced Oil Recovery, Tulsa, OK, April.

[22] Mani, V. and K.K. Mohanty. Effect of spreading coefficient on three-phase flow in porous media. *J. Colloid & Interface Sci.*, 187:45–56, March 1997.

[23] Fenwick, D.H., and M.J. Blunt. Calculating three-phase relative permeabilities using network modeling, proceedings of the 1996 5th European Conference on the Mathematics of Oil Recovery, Leoben, Austria, September.

[24] Fenwick, D.H., and M.J. Blunt. Three-dimensional modeling of three phase imbibition and drainage. *Advances in Water Resources*, 21:121–143, 1998.

[25] Fenwick, Darryl H. *Pore Scale Modeling of Three-Phase Flow.* PhD thesis, Stanford University, Stanford, CA, February 1997.

[26] Dumoré, J.M. and R.S. Schols. Drainage capillary pressure functions and the influence of connate water. *SPE Journal*, 14:437–444, October 1974.

[27] Kantzas, A., I. Chatzis, and F.A.L. Dullien. Enhanced oil recovery by inert gas injection, paper SPE 17379 proceedings of the 1988 Sixth SPE/DOE Symposium on Enhanced Oil Recovery, Tulsa, OK, April.

[28] Vizika, O. Effect of the spreading coefficient on the efficiency of oil recovery with gravity drainage, proceedings of the 1993 Symposium on Enhanced Oil Recovery, presented before the Division of Petrolium Chemistry, Inc., Denver, CO.

[29] Kalaydjian, F.J.M., J.C. Moulu, O. Vizika, and P.K. Munkerud. Three-phase flow in water-wet porous media: Determination of gas/oil relative permeabilities under various spreading conditions, paper SPE 26671 proceedings of the 1993 68th Annual Technical Conference and Exhibition of the SPE, Houston, TX, October.

[30] Skurdal, H., O. Hustad, and T. Holt. Oil recovery by gravity drainage during gas injection, proceedings of the 1995 8th European Symposium on Improved Oil Recovery, Vienna, Austria, May.

[31] Zhou, D., and M.J. Blunt. Effect of spreading coefficient on the distribution of light non-aqueous phase liquid in the subsurface. *Journal of Contaminant Hydrology*, 25:1–19, 1997.

[32] Adamson, A.W. *Physical Chemistry of Surfaces.* John Wiley & Sons, New York, fifth edition, 1990.

[33] Hough, D.B. and L.R. White. The calculation of hamaker constants from lifshitz theory with applications to wetting phenomena. *Adv. Colloid & Interface Sci.*, 14:3–41, 1980.

[34] Del Cerro, C. and G.J. Jameson. The behavior of pentane, hexane, and heptane on water. *J. Colloid & Interface Sci.*, 78:362–375, December 1980.

[35] Oren, P.E. and W.V. Pinczewski. The effect of film-flow on the mobilization of waterflood residual oil by gas flooding, proceedings of the 1991 6th European IOR Symposium, Stavanger, Norway, May.

[36] Dong, M., F.A.L. Dullien, and I. Chatzis. Imbibition of oil in film form over water present in edges of capillaries with an angular cross-section. *J. Colloid & Interface Sci.*, 172:278–288, December 1995.

[37] Landau, L.D., and E.M. Lifshitz. *Fluid Mechanics.* Pergamon Press, Oxford, 1959.

[38] Blunt, M.J., D. Zhou, and D.H. Fenwick. Three phase flow and gravity drainage in porous media. *Transport in Porous Media*, 20:77–103, 1995.

[39] Kalaydjian, F.J.M. Performance and analysis of three-phase capillary pressure curves for drainage and imbibition in porous media, paper SPE 24878 proceedings of the 1992 67th Annual Technical Conference and Exhibition of the SPE, Washington D.C., October.

[40] Ransohoff, T.C. and C.J. Radke. Laminar flow of a wetting liquid along the corners of a predominantly gas-occupied noncircular pore. *J. Colloid & Interface Sci.*, 121:392–401, February 1988.

[41] Zhou, D., M.J. Blunt, and F.M. Orr, Jr. Hydrocarbon drainage along corners of noncircular capillaries. *Journal of Colloid & Interface Science*, 187:11–21, 1997.

[42] Naylor, P., N.C. Sargent, A.J. Crosbie, A.P. Tilsed, and S.G. Goodyear. Gravity drainage during gas injection, proceedings of the 1995 8th European Symposium on Improved Oil Recovery, Vienna, Austria, May.

[43] Goodyear, S.G., and P.I.R. Jones. Relative permeabilities for gravity stabilized gas injection, proceedings of the 1993 7th European IOR Symposium, Moscow, Russia.

[44] Grader, A. S., and D.J. O'Meara, Jr. Dynamic displacement measurements of three-phase relative permeabilities using three immiscible liquids, paper SPE 18293 proceedings of the 1988 63rd Annual Technical Conference and Exhibition of the SPE, Houston, TX, October.

[45] Blunt, M. and B. Rubin. Implicit flux limiting schemes for petroleum reservoir simulation. *Journal of Computational Physics*, 102:194–210, September 1992.

[46] Hirasaki, G.J. Structural interactions in the wetting and spreading of van der waals fluids. *Journal of Adhesion Science and Technology*, 7(3):285–322, 1993.

[47] Oak, M. J. Three-phase relative permeability of water-wet berea, paper SPE 20183 proceedings of the 1990 Seventh SPE/DOE Symposium on Enhanced Oil Recovery, Tulsa, OK, April.

[48] Leverett, M.C. and W.B. Lewis. Steady flow of gas-oil-water mixtures through unconsolidated sands. *Transactions of AIME*, 142:107–116, 1941.

[49] Nordtvedt, J.E., E. Ebeltoft, J.E. Iversen, A. Sylte, H. Urkedal, K.O. Vatne, and A.T. Watson. Determination of three-phase relative permeabilities from displacement experiments, paper SPE 36683 proceedings of the 1996 Annual Technical Conference and Exhibition, Denver, Co, October.

[50] Baker, L. E. Three-phase relative permeability correlations, paper SPE 17369 proceedings of the 1988 Sixth SPE/DOE Symposium on Enhanced Oil Recovery, Tulsa, OK, April.

[51] Skauge, A., O. Eleri, A. Graue, and P.A. Monstad. Influence of connate water on oil recovery by gravity drainage, paper SPE 27817 proceedings of the 1994 Improved Oil Recovery Symposium, Tulsa, OK, April.

[52] Fenwick, D. H., and Blunt, M. J., "Calculating Three-Phase Relative Permeabilities Using Network Modeling", Paper presented at the 5th European Conference on the Mathematics of Oil Recovery, Leoben, Austria, 3-6 Sept. 1996.

[53] Virnovsky, G. A.: "Determination of Relative Permeabilities in a Three-Phase Flow in a Porous Medium," *Izv. Akad. Nauk SSSR, Mekh. Zhidk. Gaza* (1984) **5**, 187-189.

[54] Welge, H. J.: "Displacement of Oil from Porous Media by Water and Gas," *Trans., AIME* (1950) **198**, 314-316.

[55] Johnson, E. F., Bossler, D. P., and Naumann, V. O.: "Calculation of Relative Permeability from Displacement Experiments," *Trans., AIME* (1959) **216**, 370.

[56] Siddiqui, S., Hicks, P. J., Grader, A. S.: "Verification of Buckley Leverett Three Phase Theory Using Computerized Tomography," *J. Pet. Sci. Eng.* (1996) **15**(1), pp. 1-21.

[57] Sarem, A. M.: "Three-Phase Relative Permeability Measurements by Unsteady-State Method," Soc. Pet. Eng. J., (Sept. 1966) **6**, 199-205.

[58] Oak, M. J., Baker, L. E., and Thomas, D. C.: "Three Phase Relative Permeability of Berea Sandstone," Journal of Petroleum Technology, **42** (1990) 1057-1061.

[59] Minssieux L., Duquerroix J-P.: "WAG Flow Mechanisms in Presence of Residual Oil," SPE 28623 proceeding of the SPE 69th Annual Technical Conference and Exhibition, New Orleans, LA, U.S.A., 25-28 Sept. 1994.

[60] Kalaydjian, F. J.-M., Moulu, J-C., Vizika, O., and Munkerun, P. K.: "Three Phase Flow in Water-Wet Porous Media: Determination of Gas/Oil Relative Permeabilities Under Various Spreading Conditions" SPE 26671 proceedings of the 68th Annual Technical Conference and Exhibition of the SPE, Houston, TX, October, 1993.

[61] Vizika, O., and Lombard, J-M.: "Wettability and Spreading: Two Key Parameters in Oil Recovery With Three-Phase Gravity Drainage," *Soc. Pet. Eng. Res. Eng.* **11**, p 54-60, February 1996.

[62] Naylor, P., Sargent, N. C., Crosbie, A. J., Tilsed A. P., Goodyear S. G.: "Gravity Drainage during Gas Injection," proceeding of the 8th European IOR-Symposium in Vienna, Austria, May 15-17, 1995.

[63] Chalier, G., Giry, V., Madaoui, K., Sakthikumar S., and Maquignon Ph.: "Three Phase Oil Relative Permeability Determination as a Key Point in the Evaluation of a Tertiary Gas Gravity Drainage Project," SPE 30761 proceedings of the 70th SPE Annual Technical Conference and Exhibition, Dallas, TX, U.S.A., October 22-25, 1995.

[64] Skau, A., Eleri, O. O., Graue, A., and Monstad, P.: "Influence of Connate Water on Oil Recovery by Gravity Drainage," SPE 27817 proceedings of the SPE/DOE Ninth Symposium on Improved Oil Recovery, Tulsa, OK, U.S.A., April 17-20, 1994.

[65] Espie, A. A., Brown, C. E., Narayanan, K. R., Wilcox, T. C.: "A Laboratory Investigation of Gravity Drainage/Waterflood Interaction in Prudhoe Bay," SPE 28614 proceedings of the SPE 69th Annual Technical Conference and Exhibition, New Orleans, LA, U.S.A., Sept. 25-28, 1994.

[66] Fayers, F. J.: "Extension of Stone's Method 1 and conditions for real characteristics in three phase flow," *Soc. Pet. Eng. Res. Eng.* , **4** (1989) 437-445.

[67] Parker, J. C., Lenhard, R. J., and Kuppusamy, T.: "A Parametric Model for Constitutive Properties Governing Multiphase Flow in Porous Media," *Water Resources Research*, **23** (1987) 618-624.

[68] Stone, H. L.: "Probability Model for Estimation Three-Phase Relative Permeability," *Journal of Petroleum Technology*, **20** (1970) 214-218.

[69] Stone, H. L.: "Estimation of Three-Phase Relative Permeability and Residual Data," *Journal of Canadian Petroleum Technology*, **12** (1973) 53-61.

[70] van Genuchten, M. T.: "A Closed-form Equation for Predicting the Hydraulic Conductivity of Unsaturated Soils," *Soil Science Society of American Journal*, **44** (1980) 892-898.

[71] Baker, L. E.: "Three Phase Relative Permeability Correlations," paper SPE 17369 proceedings of the 1988 Sixth SPE/DOE Symposium on Enhanced Oil Recovery, Tulsa, OK, April.

[72] Delshad, M., and Pope, G. A.: "Comparison of the Three Phase Oil Relative Permeability Models," *Transport in Porous Media*, **4** (1989) 59-83.

[73] Fayers, F. J. and Matthews, J. D.: "Evaluation of Normalized Stone's Methods for Estimating Three-Phase Relative Permeabilities," *Soc. Pet. Eng. J* **24** (April 1984) 224-232.

[74] Hicks, P. J., and Grader, A. S.: "Simulation of Three Phase Displacement Experiments," *Transport in Porous Media*, (1996), In Press.

[75] Corey, A. T., Rajthens, C. H., Henderson, J. H., and Wyllie, M. R. J.: "Three Phase Relative Permeability Models," *AIME* (1956) **207**, 349-351.

[76] Trangenstein, J. A.: "Three-Phase Flow with Gravity," *Contemporary Mathematics* (1989) **100**, 147-159.

[77] Holden, L.: "On the strict hyperbolicity of the Buckley-Leverett Equations for Three-Phase Flow in a Porous Medium," *SIAM J. Applied Math.* (June 1990) **50**, No. 3, 667-682.

[78] Guzman, R. E. and Fayers, F. J.: "Mathematical Properties of Three-Phase Flow Equations" SPE 35154, and "Solution to the Three-Phase Buckley-Leverett Problem" SPE 35156, *Soc. Pet. Eng. J.* 1996 (in Press).

[79] Guzman, R. E.: *Mathematics of Three Phase Flow*, PhD dissertation, Stanford University, Stanford, CA (July 1995).

[80] Falls, A. H., and Schulte, W. M.: "Theory of Three Component, Three Phase Displacement in Porous Media," *Soc. Pet. Eng. Res. Eng.* **7** (August 1992) 377-384.

[81] Falls, A. H., and Schulte, W. M.: "Features of Three Component, Three Phase Displacement in Porous Media," *Soc. Pet. Eng. Res. Eng.* **7** (November 1992) 426-432.

[82] Holm, L.W., and Josendal, V.A.: "Effect of Oil Composition on Miscible-Type Displacement by Carbon Dioxide," *Soc. Pet. Eng. J.* **22** (1982), 87-98.

[83] Glaso, O.: *Soc. Pet. Eng. J.* **25** (1985) 927-934.

[84] Orr, F.M., Jr., and Silva, M.K.: " Effect of Oil Composition on Minimum Miscibility Pressure - Part 2: Correlation," *Soc. Pet. Eng. Res. Eng.* **27** (1987), 479-491.

[85] Stalkup, F.I.: "Displacement Behavior of the Condensing/Vaporizing Gas Drive Process," SPE Annual Technical Conference and Exhibition, SPE 16715, 1987.

[86] Zick, A.A.: "A Combined Condensing/Vaporizing Mechanism in the Displacement of Oil by Enriched Gas," SPE 15493 Presented at the SPE Annual Technical Conference and Exhibition, New Orleans, LA, 1986.

[87] Pederson, K.S., Fjellerup, J., Thomassen, P., Fredenslund, A.: "Studies of Gas Injection into OIl Reservoirs by a Cell to Cell Simulation Model," SPE 15599, presented at the 1986 SPE Annual Technical COnference and Exhibition, New Orleans, LA.

[88] Jensen, F. and Michelsen M.L.: "Calculation of First Contact and Multiple Contact Minimum Miscibility Pressures," *In Situ* **14** (1990), 1-17.

[89] Neau, E., Avaulee, L., and Jaubert, J.N.: " A New Algorithmn for Enhanced Oil Recovery Calculations," *Fluid Phase Equilibria* **117** (1996), 265-272.

[90] Orr, F.M., Jr., Johns, R.T., and Dindoruk, B.: "Development of Miscibility in Four-Component CO_2 Floods," *Soc. Pet. Eng. Res. Eng.* **40** (1993), 135-142.

[91] Johns, R.T., Dindoruk, B., and Orr, F.M., Jr.: "Analytical theory of combined condensing/vaporizing gas drives," *SPE Adv. Tech.* **2** (1993) 7-16.

[92] Metcalfe, R.S., Fussell, D.D., and Shelton, J.L.: " A Multi-Cell Equilibrium Seperation Model for the Study of Multibple Contact Miscibility in Rich Gas Drives," *Soc. Pet. Eng. J.* **13** (1973) 147-155.

[93] Hearn, C.L., and Whitson, C.H.: "Evaluating Miscible and Immiscible Gas Injection in the Sarah Field, Oman," SPE 29115 Presented at the 13th SPE Symposium on Reservoir Simulation (1995), San Antonio, TX.

[94] Johns, R.T., and Orr, F.M., Jr.: "Miscible gas displacement of Multi-Component Oils," *Soc. Pet. Eng. J.* **1** (1996) 39-50.

[95] Dindoruk, B.: "Analytical Theory of Multiphase, Multicomponent Displacement in Porous Media," PhD dissertation, Stanford Univ., 1992.

[96] Monroe, W.W., Silva, M.K., Larsen, L.L., and Orr, F.M., Jr.: "Composition Paths in Four-Component Systems: Effect of Dissolved Methane on 1D CO_2 Flood Performance," *Soc. Pet. Eng. Res. Eng.* **35** (1990), 42-58.

[97] Larson, R.G., and Hirasaki, G.J.: "Analysis of the Physical Mechanisms in Surfactant Flooding," *Soc. Pet. Eng. J.* **18** (1978), 42-58.

[98] Larson, R.G.: "The Influence of Phase Behavior on Surfactant Flooding," *Soc. Pet. Eng. J.* **19** (1979), 411-422.

[99] Helffreich, F.G.: "Theory of Multicomponent, Multiphase Displacement in Porous Media," *Soc. Pet. Eng. J.* **21** (1981), 51-62.

[100] Hirasaki, G.J.: "Applications of the Theory of Multicomponent, Multiphase Displacement to Three-Component, Two-Phase Surfactant Flooding," *Soc. Pet. Eng. J.* **21** (1981), 191-204.

[101] Welge, H.J.: "A Simplified Method for Computing Oil Recovery by Gas or Water Drive," *Trans., AIME* **195** (1952), 91-98.

[102] Wachmann, C.: "The Mathematical Theory for the Displacement of Oil and Water by Alcohol," *Soc. Pet. Eng. J.* **231** (1964), 250-266.

[103] J.M. Dumore, J. Hagoort, A.S. Risseeuw, Dumoré, J.M. Hagoort, J. and Risseeuw, A.S.: "An Analytical Model for One-Dimensional, Three-Component Condensing and Vaporizing Gas Drives," *Soc. Pet. Eng. J.* **24** (1984), 169-179.

[104] Johns R.T.: "Analytical Theory of Multicomponent Gas Drives with Two-Phase Mass Transfer," PhD dissertation, Stanford Univ., 1992.

[105] Dindoruk, B., R.T. Johns, F.M. Orr, Jr.: "Analytical Solution for Four Component Gas Displacements with Volume Change on Mixing," Third European Conference on the Mathematics of Oil Recovery, Deft, Holland, June, 1992.

[106] Johansen, T., B. Dindoruk, F.M. Orr, Jr.: "Global Triangular Structure in Four-Component Conservation Laws," Fourth European Conference on the Mathematics of Oil Recovery, Roros, Norway, June, 1994.

[107] Whitson, C., M.L. Michelsen: "The Negative Flash: Part II, Fluid Properties and Phase Equilibria for Chemical Process Design," *Fluid Phase Equilibria* **53** (1989) 51-71.

[108] Rachford, H.H., J.D. Rice, Petrol. Technol., Section 1, p19, Section 2, p3, 1952.

[109] Peng, D.Y., D.B. Robinson: "A New Two-Constant Equation of State," *Ind. Eng. Chem. Fund.* **15** (1976) 59-64.

[110] Michelsen, M.J.: "The Isothermal Flash Problem. Part 1. Stability," *Fluid Phase Equilibria* **9** (1982), 21-40.

[111] Walsh, B.W. and Orr, F.M. Jr.: "Prediction of Miscible Flood Performance: The Effect Of Dispersion on Composition Paths in Ternary Systems," *In Situ* **14** (1990), 19-47.

[112] Metcalfe, R.S. and Yarborough, L.: "The Effect of Phase Equilibria on the CO_2 Displacement," *Soc. Pet. Eng. J.* **19** (1979), 242-252.

[113] Wilson G.: "A Modified Redlich-Kwong Equation of State. Application to General Physical Data Calculations," Paper 15c, American Inst. of Chem. Eng. National Meeting, Cleveland, 1968.

[114] Muskat, M.: *Flow of Homogeneous Fluids*, International Human Resources Development Corporation, 137 Newbury Street, Boston MA 02116 (1937, 1982).

[115] Muskat, M.: "The Theory of Potentiometric Models," *Trans. AIME* (1948) **179**, 216–221.

[116] Muskat, M. and Wyckoff, R.: "A Theoretical Analysis of Waterflooding Networks," *Trans. AIME* (1934) **107**, 62–77.

[117] Fay, C.H. and Prats. M.: "The Application of Numerical Methods to Cycling and Flooding Problems," in proceedings of the 1951 3rd World Petroleum Congress, The Hague.

[118] Higgins R.V. and Leighton, A.J.: "A Computer Method to Calculate Two–Phase Flow in Any Irregularly Bounded Porous Medium," *Journal of Petroleum Technology* (June 1962) **14**, 679–683.

[119] Higgins R.V. and Leighton, A.J.: "Computer Prediction of Water Drive of Oil and Gas Mixtures Through Irregularly Bounded Pororus Media — Three-Phase Flow," *Journal of Petroleum Technology* (September 1962) **14**, 1048–1054.

[120] Higgins, R.V., Boley, D.W., and A.J. Leighton: "Aids to Forecasting The Performance of Water Floods," *Journal of Petroleum Technology* (September 1964) **16**, 1076–1082.

[121] Parsons, R.W.: "Directional Permeability Effects in Developed and Unconfined Five-Spots," *Journal of Petroleum Technology* (April 1972) **24**, 487–494.

[122] Martin, J.C. and Wegner, R.E.: "Numerical Solution of Multiphase, Two-Dimensional Incompressible Flow Using Streamtube Relationships," *Society of Petroleum Engineers Journal* (October 1979) **19**, 313–323.

[123] Bommer, M.P. and Schechter, R.S.: "Mathematical Modeling of In-Situ Uranium Leaching," *Society of Petroleum Engineers Journal* (December 1979) **19**, 393–400.

[124] Lake, L.W., Johnston, J.R., and Stegemeier, G.L.: "Simulation and Performance Prediction of a Large-Scale Surfactant/Polymer Project," *Society of Petroleum Engineers Journal* (December 1981) **21**, 731–739.

[125] Emanuel, A.S., Alameda, G.K., Behrens, R.A., and Hewett, T.A.: "Reservoir Performance Prediction Methods Based on Fractal Geostatistics," *SPE Reservoir Engineering* (August 1989) **4**, 311–318.

[126] Hewett, T.A. and Behrens, R.A.: "Conditional Simulation of Reservoir Heterogeneity With Fractals," *SPE Formation Evaluation* (September 1990) **8**, 217–225.

[127] Hewett, T.A. and Behrens, R.A.: "Scaling Laws in Reservoir Simulation and Their Use in a Hybrid Finite Difference/Streamtube Approach to Simulation the Effects of Permeability Heterogeneity," *Reservoir Characterization, II*, L. Lake and J. Carroll, H.B. (eds.), Academic Press, Inc., London (1991) 402–441.

[128] Renard, G.: "A 2D Reservoir Streamtube EOR Model with Periodical Automatic Regeneration of Streamlines," *In Situ* (1990) **14**, No. 2, 175–200.

[129] Datta–Gupta, A. and King, M.J.: "A Semianalytic Approach to Tracer Flow Modeling in Heterogeneous Permeable Media," *Advances in Water Resources* (1995) **18**, 9–24.

[130] Thiele, M.R., Blunt, M.J., and Orr, F.M., Jr.: "Modeling Flow in Heterogeneous Media Using Streamtubes — I. Miscible and Immiscible Displacements," *In Situ* (August 1995) **19**, No. 3, 299–339.

[131] Thiele, M.R., Blunt, M.J., and Orr, F.M., Jr.: "Modeling Flow in Heterogeneous Media Using Streamtubes — II. Compositional Displacements," *In Situ* (November 1995) **19**, No. 4, 367–391.

[132] Thiele, M.R., Batycky, R.P., Blunt, M.J., and Orr, F.M., Jr.: "Simulating Flow in Heterogeneous Media Using Streamtubes and Streamlines," *SPE Reservoir Engineering* (February 1996) **10**, No. 1, 5–12.

[133] Blunt, M.J., Liu, K., Thiele, M.R.: "A Generalized Streamline Method to Predict Reservoir Flow," *Petroleum Geoscience* (1996) **2**, 259–269.

[134] Behrens, R.A., Jones, R.C., and Emanuel, A.S.: "Implementation of a Streamline Method for Flow Simulation of Large Fields," In Proceedings of 47th Annual Technical Meeting of the Petroleum Society, Calgary, Canada (June 10-12, 1996) CIM 96-55.

[135] Batycky, R.P., Thiele, M.R., and Blunt, M.J.: "A Streamline Simulator to Model Field Scale Three-Dimensional Flow," in proceedings of the 1996 5th European Conference on the Mathematics of Oil Recovery, Leoben, Austria, September.

[136] Batycky, R.P., Blunt, M.J., and Thiele, M.R.: "A 3D Multi-Phase Streamline Simulator with Gravity and Changing Well Conditions," in proceedings of the 17th International Energy Agency Collaborative Project on Enhanced Oil Recovery, Sydney, Australia (September 1996).

[137] Bratvedt, F., Gimse, T., Tegnander, C.: "Streamline Computations for Porous Media Flow Including Gravity," *Transport in Porous Media* (October 1996) **25**, No. 1, 63–78.

[138] Hewett, T.A. and Yamada, T.: "Theory of the Semi-Analytical Calculation of Oil Recovery and Effective Relative Permeabilities using Streamtubes," *Advances in Water Resources* (1997) **20**, No. 5–6, 279–292.

[139] Peddibhotla, S. Datta-Gupta, A., and Guoping Xue: "Multiphase Streamline Modeling in Three Dimensions: Further Generalizations and a Field Application," paper SPE 38003 in proceedings of the 1997 SPE Reservoir Simulation Symposium, Dallas, TX, June, 8-11.

[140] Thiele, M.R., Batycky, R.P., and Blunt, M.J.: "A Streamline-Based 3D Field-Scale Compositional Reservoir Simulator," paper SPE 38889 in proceedings of the 1997 Annual Technical Conference and Exhibition, San Antonio, TX, October, 5-8.

[141] Thiele, M.R., Rao, S.E., and Blunt, M.J.: "Quantifying Uncertainty in Reservoir Performance Using Streamtubes," *Mathematical Geology* (1996) **28**, No. 7, 843–856.

[142] Ehlig-Economides, C.A. and Spath, J.: "Waterflood Infill Well Pattern Strategies for Horizontal and Multibranch Wells," paper SPE 35209 in proceedings of the 1996 Permian Basin Oil Recovery Conference, Midland, TX, March, 27-29.